

EFFECT OF DEALUMINATION AND DESILICATION OF BETA ZEOLITE ON PERFORMANCE
OF NICKEL CATALYSTS IN HYDROISOMERIZATION FOR BIO-JET FUEL PRODUCTION



A Thesis Submitted in Partial Fulfillment of the Requirements
for the Degree of Master of Science in Petrochemistry and Polymer Science
Field of Study of Petrochemistry and Polymer Science
FACULTY OF SCIENCE
Chulalongkorn University
Academic Year 2020
Copyright of Chulalongkorn University

ผลของดีอะลูมิเนียมและดีซิลิกอนของซีโอไลต์ปีต้าต่อสมรรถนะของตัวเร่งปฏิกิริยานิกเกิลในไฮโดรไอโซเมอไรเซชันสำหรับการผลิตเชื้อเพลิงชีวภาพอากาศยาน



วิทยานิพนธ์นี้เป็นส่วนหนึ่งของการศึกษาตามหลักสูตรปริญญาวิทยาศาสตรมหาบัณฑิต
สาขาวิชาปิโตรเคมีและวิทยาศาสตร์พอลิเมอร์ สาขาวิชาปิโตรเคมีและวิทยาศาสตร์พอลิเมอร์
คณะวิทยาศาสตร์ จุฬาลงกรณ์มหาวิทยาลัย
ปีการศึกษา 2563
ลิขสิทธิ์ของจุฬาลงกรณ์มหาวิทยาลัย

6172056823 : MAJOR PETROCHEMISTRY AND POLYMER SCIENCE

KEYWORD: bio-jet fuel, hydroisomerization, palm olein, desilication,
dealumination

Warodom Hunsiri : EFFECT OF DEALUMINATION AND DESILICATION OF
BETA ZEOLITE ON PERFORMANCE OF NICKEL CATALYSTS IN
HYDROISOMERIZATION FOR BIO-JET FUEL PRODUCTION. Advisor: Prof.
NAPIDA HINCHIRANAN, Ph.D.

-The Global aviation fuel consumption tends to increase. In recent years, the European Union has announced that fossil fuels jet fuel must be mixed with 10% biofuels in 2020. bio-jet fuel production has many processes such as biomass pyrolysis. or hydro-processing of vegetable oil Therefore, there is a challenge to increase the volume and specificity of bio-jet fuel. At the same time, biofuels are required properties ASTM D7566 specification. The aviation fuel has the appropriate freezing point and stability requirements to be used. This research aims to convert palm olein into bio-jet fuel by using Ni-based catalyst supported on beta zeolite with and without dealumination and desilication, which was prepared by using incipient wetness impregnation. The dealuminated beta zeolite was prepared by using HF/NH₄F solution and desilicated zeolite was prepared by using NaOH solution at ambient temperature. Hydroisomerization of palm olein was investigated effect of parameter: acid and base concentration (0.25-0.75 M), initial H₂ pressure (30-50 bar), and reaction temperature (320-360 °C). The use of Ni/desilicated beta zeolite could reduce coke formation. The biofuel obtained from hydroisomerization had the high iso/normal alkane ratio at 2.54 by using Ni/beta-0.25-deA at 340 °C 40 under initial H₂ pressure to reduce freezing point at -60.1 °C.

Field of Study: Petrochemistry and
Polymer Science

Student's Signature

Academic Year: 2020

Advisor's Signature

ACKNOWLEDGEMENTS

The author wishes to express greatest gratitude to my advisor, Professor Dr. Napida Hinchiranan, for her advice, assistance and generous encouragement throughout the course of this research. In addition, the author wishes to express deep appreciation to Professor Dr. Chawalit Ngamcharussrivichai, Associate Professor Dr. Duangamol Tungasmita and Associate Professor Ekasith Somsook for serving as the chairman, and members of my thesis committee, respectively, and provide their valuable suggestions and comments.

Appreciation is also extended to the Science Achievement Scholarship of Thailand (SAST), Program of Petrochemistry and Polymer Science and the Department of chemical Technology, Faculty of Science, Chulalongkorn University for granting financial support to fulfill this study and provision of experimental facilities.

The author is thankful for support the waste tire powder. Finally, the author is very appreciated to his family and his best friends for their assistance and encouragement throughout his entire education.



Warodom Hunsiri

TABLE OF CONTENTS

	Page
.....	iii
ABSTRACT (THAI).....	iii
.....	iv
ABSTRACT (ENGLISH).....	iv
ACKNOWLEDGEMENTS.....	v
TABLE OF CONTENTS.....	vi
LIST OF TABLES.....	x
LIST OF FIGURES.....	xi
CHAPTER 1.....	1
1.1 The Statement of Problem.....	1
1.2 Objectives.....	3
1.3 The Scope of This Research Work.....	4
CHAPTER 2.....	6
2.1 Sustainable aviation fuel.....	6
2.2 Jet fuels.....	8
2.2.1 Compositions of jet fuels.....	8
2.2.2 Jet fuel properties.....	9
2.2.3 Bio-jet fuels.....	10
2.2.4 Sustainable aviation fuel productions and feedstocks.....	10
2.3 Hydro-processing.....	13
2.4 Hydroisomerization.....	14

2.5 Mesoporous zeolite	15
2.5.1 Dealumination	16
2.5.2 Desilication	17
2.6 literature review	19
CHAPTER 3.....	23
3.1 Materials.....	23
3.2 Instruments.....	24
3.3 Experiment.....	25
3.3.1 Preparation of treated supports	25
3.3.1.1 Dealumination.....	25
3.3.1.2 Desilication.....	25
3.3.2 Catalyst preparation.....	25
3.3.3 Hydroisomerization of palm olein.....	26
3.3.4 Catalyst characterization	26
3.3.4.1 Scanning electron microscopy equipped with energy dispersive spectroscopy (SEM-EDS).....	26
3.3.4.2 Textural properties of zeolites and Ni-based catalysts.....	27
3.3.4.3 Transmission electron microscopy (TEM).....	27
3.3.4.4 X-rays diffraction patterns of modified zeolite supports and Ni-based catalysts	28
3.3.4.5 Solid state nuclear magnetic resonance (NMR) spectroscopy.....	29
3.3.4.6 NH ₃ Temperature programmed desorption (NH ₃ -TPD).....	30
3.3.4.7 Fourier transform infrared spectra of pyridine adsorption (py-FTIR)	31
3.3.4.8 Hydrogen temperature programmed reduction (H ₂ -TPR)	32

3.3.4.9 Actual NiO content supported on beta zeolites	32
3.3.4.10 Ni metal dispersion on zeolite before and after dealumination and desilication	33
3.3.5. Characterization of products	33
3.3.5.1 Coke deposition on catalyst surface	33
3.3.5.2 Chemical composition in liquid products	34
3.3.5.3 Heating value of liquid products.....	35
3.3.5.4 Freezing point of liquid products.....	35
CHAPTER 4.....	37
4.1 The effect of dealumination on hydroisomerization of palm olein.....	37
4.1.1 Characterization of beta zeolite supports before and after dealumination	37
4.1.2 Characterization of Ni-based catalysts supported onto beta zeolite with and without dealumination.....	44
4.1.3 Hydroisomerization of palm olein over Ni/dealuminated beta zeolite catalysts.....	49
4.1.3.1 Effect of initial H ₂ pressure on hydroisomerization of palm olein over Ni/dealuminated zeolites.....	50
4.1.3.2 Effect of dealumination and reaction temperature on product distribution and chemical compositions of liquid product.....	58
4.2 The effect of desilication on hydroisomerization of palm olein	65
4.2.1 Catalyst chracterization	65
4.2.2 Hydroisomerization of palm olein over Ni based catalysts supported on desilicated beta zeolite.....	76
4.3 Freezing points of biofuel from hydroisomerization.....	80
CHAPTER 5.....	82

CONCLUSION	82
5.1 Conclusion	82
5.1.1 The effect of dealumination on hydroisomerization of palm olein	82
5.1.1.1 Catalyst characterization	82
5.1.1.2 Catalytic performance	82
5.1.2 The effect of desilication on hysisomerization of palme olein	83
5.1.2.1 Catalyst characterization	83
5.1.2.2 Catalytic performance	83
5.1.3 Biofuel properties in freezing point	84
5.2 Recommendations	84
APPENDIX A	85
APPENDIX B	86
APPENDIX C	87
REFERENCES	88
VITA	98

LIST OF TABLES

	Page
Table 2.1 Heating value, boiling point and freezing point of compound: aromatic, cyclo-aromatic, n-alkane, iso-alkane [30]	8
Table 2.2 Jet fuel specifications [4]	9
Table 2.3 Conversion processes of SAF approved by ASTM international [28].....	11
Table 4.1 Textural properties of beta zeolite before and after dealumination.....	38
Table 4.2 Relative peak areas for each signal in ^{27}Al MAS NMR spectra of beta zeolite before and after dealumination	41
Table 4.3 Acidic properties of beta zeolite before and after dealumination.....	43
Table 4.4 Textural properties of Ni supported beta zeolites before and after dealumination	45
Table 4.5 Actual Ni content, NiO crystalline size, Ni dispersion, H_2 consumption and reducibility Ni-based catalysts.	49
Table 4.6 Textural properties of beta zeolite before and after desilication	68
Table 4.7 %Relative peak area for each signal in ^{29}Si MAS NMR spectra of beta zeolite before and after desilication	70
Table 4.8 Acidic properties of beta zeolite before and after desilication.....	72
Table 4.9 Actual Ni content, NiO crystalline size, Ni dispersion, H_2 consumption and reducibility of Ni-based catalysts supported on beta zeolites with and without desilication	75

LIST OF FIGURES

	Page
Fig. 2.1 Expected aircraft CO ₂ emissions from international aviation, reflecting contributions from the ICAO Basket of Measures towards international aviation's global aspirational goals (Source: ICAO, 2016).	7
Fig. 2.2 Hydro-processing pathway of triglyceride [20].....	13
Fig. 2.3 Schematic representation of MFI desilication by NaOH treatment [23]......	18
Fig. 2.4 Comparison of the conversions of n-hexane and the yields of branched C ₆ isomers and C ₁ –C ₅ by-products in the hydroisomerization reaction over*BEA and MOR catalysts with Pt introduced by a conventional incipient wetness impregnation (Pt/H-*BEA/4.2 and Pt/H-MOR/12) and the mechanical mixtures of the protonic form of zeolite (Pt/Al ₂ O ₃ (H-*BEA/4.2-Pt/Al ₂ O ₃ and H-MOR/12-Pt/Al ₂ O ₃)) at 225°C.....	19
Fig. 3.1 Scanning Electron Microscopy with Energy Dispersive Spectroscopy (SEM-EDS) (JEOL, model JSM-5480LV)	26
Fig. 3.2 Surface area analyzer (Quantachrome, model ASiQwin).....	27
Fig. 3.3 Transmission electron microscopy (TEM) (JEOL, model JEM1400).....	28
Fig. 3.4 X-ray diffractometer (XRD) (Bruker, model D8 advance)	29
Fig. 3.5 Nuclear magnetic resonance spectrometer (solid state - NMR) (BRUKER, AVANCE III HD-Ascend 400 WB).....	30
Fig. 3.6 Chemisorption analyzer (MicrotracBEL, model BELCAT II).....	31
Fig. 3.7 Inductively coupled plasma - optical emission spectrometry (ICP-OES) (Perkin Elmer Inc., AVIO 200).....	32
Fig. 3.8 Thermo gravimetric analyzer (TGA) (model TGA8000, PerkinElmer).	34
Fig. 3.9 Gas chromatography mass spectrometer (model Shimadzu-2010, Shimadzu).	34
Fig. 3.10 CHN analyzer (model PE 2410, PerkinElmer).	35

Fig. 3.11 Differential scanning calorimeter (DSC) model DSC822 (METTLER).	36
Fig. 4.1 N ₂ adsorption-desorption isotherm and pore size distribution of (a) beta, (b) beta-0.25M-deA, (c) beta-0.50M-deA, and (d) beta-0.75M-deA.....	38
Fig. 4.2 XRD pattern of parent zeolite and dealuminated zeolites (a) beta, (b) beta-0.25M-deA, (c) beta-0.50M-deA, and (d) beta-0.75M-deA.	39
Fig. 4.3 ²⁷ Al MAS NMR spectra of (a) beta, (b) beta-0.25M-deA, (c) beta-0.50M-deA, and (d) beta-0.75M-deA.....	40
Fig. 4.4 NH ₃ -TPD profiles of (a) beta, (b) beta-0.25M-deA, (c) beta-0.50M-deA, and (d) beta-0.75M-deA.....	42
Fig. 4.5 Pyridine FTIR spectra of (a) beta, (b) beta-0.25M-deA, (c) beta-0.50M-deA, and (d) beta-0.75M-deA.....	43
Fig. 4.6 Replacement of the aluminum associated hydroxyl with fluoride [55].....	44
Fig. 4.7 N ₂ adsorption-desorption isotherm and pore size distribution of (a) Ni/beta, (b) Ni/beta-0.25M-deA, (c) Ni/beta-0.5M-deA, and (d) Ni/beta-0.75M-deA catalysts. ...	45
Fig. 4.8 TEM images and distribution of the size of nickel crystallites on the surface of (a) Ni/beta and (b) Ni/beta-0.25M-deA catalysts.....	46
Fig. 4.9 XRD patterns of (a) Ni/beta, (b) Ni/beta-0.25M-deA, (c) Ni/beta-0.5M-deA, and (d) Ni/beta-0.75M-deA catalysts.....	47
Fig. 4.10 H ₂ TPR profiles of (a) Ni/beta, (b) Ni/beta-0.25M-deA, (c) Ni/beta-0.50M-deA, and (d) Ni/beta-0.75M-deA catalysts.	48
Fig. 4.11 Product distribution obtained from hydroisomerization of palm olein under various initial H ₂ pressure over (a) Ni/beta, (b) Ni/beta-0.25M-deA, (c) Ni/beta-0.50M-deA, and (d) Ni/beta-0.75M-deA catalysts at 340 °C for 5 h.	51
Fig. 4.12 GCMS chromatograms of (a) jet A-1 and liquid product obtained from hydroisomerization of palm olein over (b) Ni/beta, (c) Ni/beta-0.25M-deA, (d) Ni/beta-0.50M-deA and (e) Ni/beta-0.75M-deA catalysts under 30-50 bar initial H ₂ pressure at 340 °C for 5 h.....	53

- Fig. 4.13** Selectivity to chemical compositions in the liquid product obtained from the hydroisomerization of palm olein catalyzed by Ni-based catalysts under (a) 30 bar, (b) 40 bar and (c) 50 bar initial H₂ pressure at 340 °C for 5 h. 56
- Fig. 4.14** Carbon distribution in the liquid product obtained from the hydroisomerization of palm olein at 340 °C for 5 h over (a) Ni/beta, (b) Ni/beta-0.25M-deA, (c) Ni/beta-0.5M-deA, and (d) Ni/beta-0.75M-deA under initial H₂ pressure of (1) 30 bar, (2) 40 bar and (3) 50 bar..... 58
- Fig. 4.15** Product yields obtained from hydroisomerization of palm olein over (a) Ni/beta, (b) Ni/beta-0.25M-deA, (c) Ni/beta-0.5M-deA, and (d) Ni/beta-0.75M-deA under 40 bar initial H₂ pressure at 320-360 °C for 5 h. 60
- Fig. 4.16** %Selectivity to each composition in the liquid product obtained from the hydroisomerization of olein catalyzed by Ni-based catalysts under 40 bar initial H₂ pressure at (a) 320, (b) 340 and (c) 360 °C for 5 h..... 62
- Fig. 4.17** Distribution of carbon number in the liquid product obtained from the hydroisomerization of palm olein over (a) beta, (b) beta-0.25M-deA, (c) beta-0.50M-deA, and (d) beta-0.75M-deA catalysts under 40 bar initial H₂ pressure at (1) 320, (2) 340 and (3) 360 °C. 64
- Fig. 4.18** N₂ adsorption-desorption isotherm and pore size distribution of (a) beta, (b) beta-0.25M-deS, (c) beta-0.50M-deS, and (d) beta-0.75M-deS..... 66
- Fig. 4.19** N₂ adsorption-desorption isotherm and pore size distribution of (a) Ni/beta, (b) Ni/beta-0.25M-deS, (c) Ni/beta-0.5M-deS, and (d) Ni/beta-0.75M-deS catalysts. 67
- Fig. 4.20** XRD pattern of parent and desilicated zeolites (a) beta, (b) beta-0.25M-deS, (c) beta-0.50M-deS, and (d) beta-0.75M-deS. 69
- Fig. 4.21** ²⁹Si MAS NMR spectra of (a) beta, (b) beta-0.25M-deS, (c) beta-0.50M-deS, and (d) beta-0.75M-deS..... 70
- Fig. 4.22** NH₃-TPD profiles of (a) beta, (b) beta-0.25M-deS, (c) beta-0.50M-deS, and (d) beta-0.75M-deS..... 71

Fig. 4.23 Py-FTIR spectra of (a) beta, (b) beta-0.25M-deS, (c) beta-0.50M-deS, and (d) beta-0.75M-deS.....	72
Fig. 4.24 TEM images and distribution of the size of nickel crystallites on the surface of (a) Ni/beta and (b) Ni/beta-0.25M-deS catalysts.....	73
Fig. 4.25 XRD patterns of (a) Ni/beta, (b) Ni/beta-0.25M-deS, (c) Ni/beta-0.50M-deS, and (d) Ni/beta-0.75M-deS catalysts.....	74
Fig. 4.26 H ₂ TPR profiles of (a) Ni/beta, (b) Ni/beta-0.25M-deS, (c) Ni/beta-0.50M-deS, and (d) Ni/beta-0.75M-deS catalysts.....	75
Fig. 4.27 Product distribution obtained from hydroisomerization of palm olein at 340 °C under 40 bar initial H ₂ pressure over Ni catalyst supported on desilicated zeolite.....	76
Fig. 4.28 TGA thermograms of spent Ni-based catalysts prepared by using desilicated beta zeolite applied in hydroisomerization of palm olein at 340 °C under 40 bar initial H ₂ pressure.....	77
Fig. 4.29 Selectivity to chemical compositions in the liquid product obtained from the hydroisomerization of palm olein catalyzed by Ni-based catalysts supported on beta zeolite with and without desilication under 40 bar initial H ₂ pressure at 340 °C for 5 h.....	78
Fig. 4.30 Proposed conversion routes for aromatics hydrocarbon formation in hydro-processing of fatty acids [67].....	78
Fig. 4.31 Distribution of carbon number in liquid products obtained from the hydroisomerization of palm olein over (a) beta, (b) beta-0.25M-des, (c) beta-0.50M-deS, and (d) beta-0.75M-deS catalysts at 340 °C under 40 bar initial H ₂ pressure.....	80
Fig. 4.32 DSC thermograms of liquid biofuels having different iso/normal alkane ratios obtained from hydroisomerization of palm olein over Ni-based catalyst supported on beta zeolite and commercial jet A-1.....	81

CHAPTER 1

INTRODUCTION

1.1 The Statement of Problem

Before COVID-19 pandemic, the jet fuel consumption has been forecasted to increase 1.3% in year 2030. Fossil fuels produce CO₂ and greenhouse gas (GHGs) emissions through chemical reactions. Thus, the alternative sources to produce the aviation fuels have been attractive for every country. European Union has announced that the aviation industry consumed the biofuels approximately 2 million tons in 2020 [1]. Sustainable aviation fuels (SAF) or biofuels can decrease the volume of CO₂ emissions up to 80% compared with the conventional jet fuel [2]. Biofuels derived from vegetable oils to form Jet-A fuel can also reduce the particulate matter in the exhaust gas obtained from the onboard of aircraft engines about 50 to 70% compared to the conventional jet fuels [3]. Bio-jet fuels produced from Fischer–Tropsch (F–T) synthesis and hydro-processing of oils have been approved by ASTM International (ASTM) Method D7566 for blending with the conventional jet fuel at the level up to 50%. However, the hydro-processing of vegetable and waste oils is ready for large-scale deployment [4].

In the recent research works, the triglyceride-based oils is popular to be used as the raw materials for bio-jet production via hydro-processing of palm oil [4-6]. The worldwide palm oil production produced 71 million tons in 2018 [7]. This hydro-processing can convert palm oil into bio-jet fuel range up to 55 wt% yield of feedstock [8]. The mechanism of hydro-processing for bio-jet fuel derived from triglyceride commonly consists of (i) hydrogenation of C=C bonds in triglycerides, (ii) hydrogenolysis of triglyceride into fatty acid, (iii) hydrodeoxygenation of fatty acids into normal alkanes, and (iv) hydrocracking and hydroisomerization of normal alkanes into short chains (C₈-C₁₆) with iso-structure that is suitable for applying as the jet fuel. From above process, hydrogen activating metals used as catalysts involves with the

noble metal catalysts such as Pd [9], Pt [8, 10], and Rh [5] catalysts and non-noble metals Ni [11, 12], Co [13, 14] and Mo [15] catalysts. The fourth step of hydro-processing requires metal-acid bifunctional catalysts [9, 16, 17]. Zeolites have been most widely used as solid acid catalysts due to their strong acidity and shape-selectivity [18]. From the previous studies, Ni-based catalysts supported on the various structure of zeolites were used to convert palm oil as the bio-jet fuel [4, 19]. At low temperature (below 350 °C), hydro-processing usually produces straight-chain alkanes in the diesel-like fuel in the range from C₁₅ to C₁₈. The subsequent cracking of long-chain alkanes and isomerization can increase the yield of kerosene range iso-alkanes [20]. However, the limitation of zeolite in the hydro-processing is mass diffusion into microporous structural zeolite (<2 nm) [21]. To overcome this restriction, the large pore of zeolite is required. The previous study indicated that the conversion of palm oil into bio-jet fuel via hydro-processing using Pt catalyst supported on the nanocrystalline beta zeolite having the large porous structure provided the high yield of bio-jet fuel (64.0 wt%) with high iso/normal alkanes ratio at 4.02 [8].

The mesopore zeolites with higher pore volume and larger pore size (2-50nm) can be developed by 2 major methods in demetallization of Si and Al of zeolite framework via acid leaching (dealumination) and base leaching (desilication) [22]. Mesoporous zeolites have benefit in terms of activity, selectivity, and lifetime in a wide range of catalytic reactions, including alkylation, acylation, isomerization, aromatization, cracking, pyrolysis [22, 23]. The dealumination is applied to enlarge the micropores to mesopores by removal of Al from the zeolite framework [10, 24]. This process usually generates isolated cavities rather than the interconnected mesopores resulting in the reduction of mass transport limitation of substrates involving in the catalytic reactions [22]. From the previous study, the dealuminated ZSM-22 zeolite loading Pt catalyst having higher Bronsted and Lewis acid sites could improve the catalytic activity of hydroisomerization of n-dodecane to provide the

iso-alkane products [25]. The advantages of mesoporous zeolites obtained by desilication also develop the structure to allow the improved accessibility of the reagents and products in and out the active sites [26]. From the previous investigation, the hydro-conversion of methyl palmitate using Ni-containing mesoporous Y zeolite generated via desilication could provide the percentage of selectivity of bio-jet fuel up to 64.8% from 28.7% obtained from the use of untreated Y zeolite [27].

In this research, the bio-jet fuel was obtained from hydroisomerization of palm olein over the Ni-based catalysts supported on mesoporous beta zeolites synthesized by dealumination and desilication. The effect of Si/Al atomic ratio in the treated zeolites obtained from each process on the hydroisomerization of palm olein to produce the bio-jet fuel range was investigated. The effects of process parameters such as the initial H₂ pressure and reaction temperature on the product yields, chemical components, and carbon distribution in the liquid product obtained from hydroisomerization of palm olein were also examined.

1.2 Objectives

The objectives of this research were stated as followed:

- 1.2.1 To develop and to study the physicochemicals of the Ni-catalysts supported on the mesoporous NH₄-beta zeolite prepared by dealumination and desilication.
- 1.2.2 To study the effects of treated zeolites obtained from 1.2.1, initial H₂ pressure, and reaction temperature on the yield of iso-alkanes and product selectivity obtained from hydroisomerization of palm olein over Ni-based catalysts.

1.3 The Scope of This Research Work

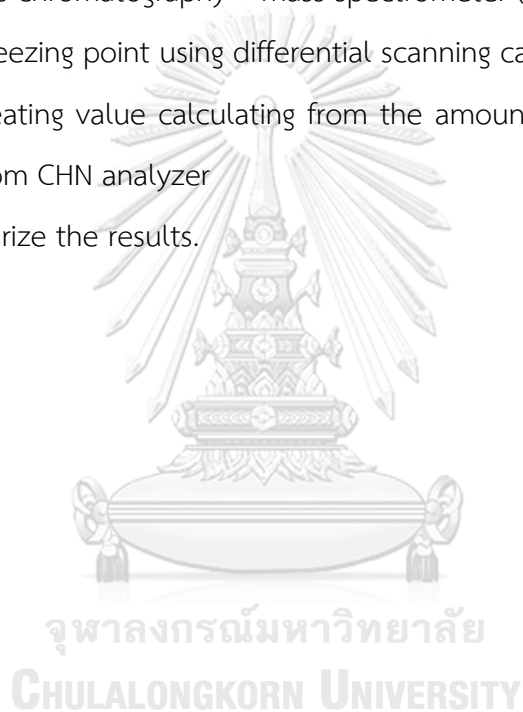
- 1.3.1 Survey previous literatures related to this work and prepare materials and instrument for this research.
- 1.3.2 Prepare mesoporous beta zeolite via dealumination in the presence of hydrofluoric acid (HF) in ammonium fluoride (NH_4F) solution and desilication using sodium hydroxide (NaOH) solution at various concentrations of acidic and basic solutions.
- 1.3.3 Prepare 10 wt% Ni catalyst supported on mesoporous zeolites obtains from 1.3.2 via incipient wetness impregnation method.
- 1.3.4 Characterize the zeolite supports and Ni/zeolite catalysts before and after dealumination and desilication in terms of
 - Textural properties: BET surface area analysis and BJH pore size distribution
 - Crystallinity and NiO crystalline size: X-ray powder diffraction (XRD)
 - Surface acidity: NH_3 -Temperature program desorption (NH_3 -TPD) and pyridine Fourier transform infrared spectrometer (py-FTIR)
 - Reducibility: H_2 temperature program reduction (H_2 -TPR)
 - Removal of Al species from framework of dealuminated zeolite: ^{27}Al magic-angle spinning nuclear magnetic resonance (^{27}Al MAS NMR)
 - Removal of Si species from framework of desilicated zeolite: ^{29}Si magic-angle spinning nuclear magnetic resonance, (^{29}Si MAS NMR)
 - Ni contents loading on zeolites: Inductively coupled plasma - optical emission spectrometry (ICP-OES)
- 1.3.5 Investigate the effect of parameters on the hydroisomerization of palm olein.
 - Types of zeolite: dealuminated zeolite and desilicated zeolite

- Acid or base concentrations for treating zeolite: 0.25M, 0.50M and 0.75M
- Initial H₂ pressure: 30-50 bar
- Reaction temperature: 320-360 °C

1.3.6 Characterize the product obtained from 1.3.5

- Solid product or coke: thermal gravimetric analyzer (TGA)
- Liquid product: composition and carbon number distribution using gas chromatography – mass spectrometer (GC-MS)
- Freezing point using differential scanning calorimeter (DSC)
- Heating value calculating from the amount of C, H, and O obtained from CHN analyzer

1.3.7 Summarize the results.



CHAPTER 2

THEORY AND LITERATURE SURVEYS

2.1 Sustainable aviation fuel [28]

In October 2017, International Civil Aviation Organization (ICAO) convened Conference on Aviation and Alternative Fuels in Mexico City, Mexico. In conference, ICAO agreed to a Declaration, endorsing the 2050 ICAO Vision for Sustainable Aviation Fuels (SAF). Industry and other stakeholders had the agreement to substitute the conventional aviation fuels with SAF in 2050 for international civil aviation to significantly reduce carbon emissions.

Although revolutionary aircraft technologies have been proposed to reduce fuel consumption such as propellers electrically powered by photovoltaic cells, fuel cells, or ultracapacitors, the large commercial aircrafts have no alternatives to liquid fuel for the near- to mid-term. After half a century of development, gas turbines are reliable and economically competitive. Since they have a vast power/weight ratio and allow excellent range due to the high energy density of liquid fuels. SAF are highly relevant as a means to reduce net CO₂ emissions, depending on the feedstock and production process adopted. Fig. 2.1 shows the expected aircraft CO₂ emissions from the international aviation, reflecting contributions from the ICAO Basket of Measures, including the possible impact of SAF on the evolution of life cycle greenhouse gases (GHGs) emissions from international civil aviation.

The potential of SAF to reduce aviation GHG emissions has been recognized by ICAO, Member States and the aviation industry. Thus, SAF are included amongst the “basket of measures” to put forward to assist States in designing their action plans on CO₂ emissions reductions. According to the ICAO 2016 trends assessment, 100% substitution of aviation fuel with SAF can expectedly reduce 63% of the baseline CO₂ emissions from international flights in 2050. This will be aviation’s most

significant contribution towards achieving carbon neutral growth. While the combustion of SAF emits similar quantities of CO₂ to the combustion of conventional fuels, SAF still provides an environmental benefit on a life cycle basis. A fuel life cycle is made up of multiple steps from the feedstock to the final use in an engine. The total carbon footprint of the fuel is obtained by adding all these emissions together in a life cycle assessment. When all those emissions are considered, SAF can produce the less emissions than the jet fuel with the baseline life cycle value of 89 g CO₂ /MJ. These emissions reductions is depend on the feedstock, production practice, conversion technology, logistics, as well as the land-use change incurred by bioenergy expansion. Certain aspects of a SAF life cycle may be considered during the sustainability certification process.

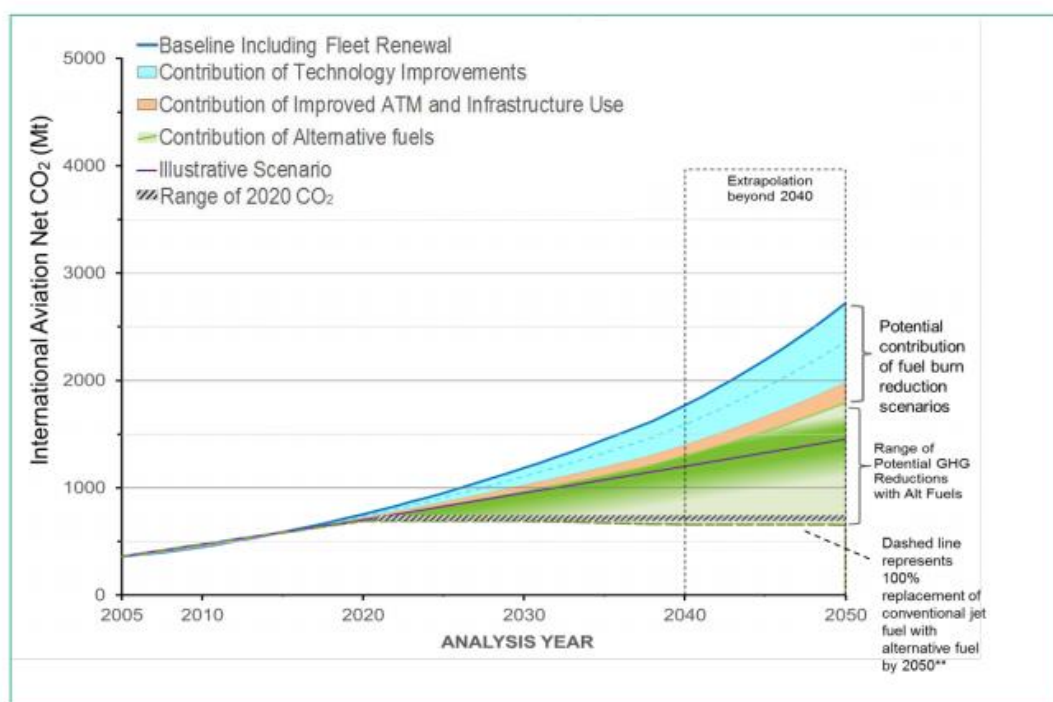


Fig. 2.1 Expected aircraft CO₂ emissions from international aviation, reflecting contributions from the ICAO Basket of Measures towards international aviation's global aspirational goals (Source: ICAO, 2016).

2.2 Jet fuels

2.2.1 Compositions of jet fuels [29]

Jet fuels is hydrocarbon blends. They contain 8-16 carbon atoms in the molecules. Hydrocarbon structures in the jet fuels are classified into 4 types: iso-alkane(40%), normal alkanes (n-alkanes) (20%), cycloalkanes (20%) and aromatics (20%) [29]. Each structural hydrocarbon affects the jet fuel properties. Among these components, the high n-alkanes content increases the freezing point of jet fuels [8]. Whereas,-the iso-alkanes have the lowest freezing point as shown in Table 2.1. To consider the aromatic compounds, they provide the lubrication properties of jet fuel and inhibit the leakage in the jet engine. However, the large amount of aromatics in the jet fuels increases the smoking burn and damages engines. Moreover, aromatics compounds have lower heating value than other chemical structures. Therefore, the suitable quantity of aromatics at 5-25% is recommended for the jet fuels.

Table 2.1 Heating value, boiling point and freezing point of compound: aromatic, cyclo-aromatic, n-alkane, iso-alkane [30]

Carbon no..	Compounds	Heating value		Boiling point (°C)	Freezing point (°C)
		MJ/m ³	MJ/Kg		
C12	n-Hexyl-benzene	32.8	39.5	258	-42
	n-Hexyl-cyclohexane	36.5	45	254	-52
	n-Dodecane	33.2	44.1	264	-10
	4-Methyl-undecane	33.2	44.1	205	-68
C13	n-Heptyl-benzene	33.4	39.7	262	-40
	n-Heptyl-cyclohexane	36.6	44.9	260	-47
	n-Tridecane	33.6	44.1	268	-6
	3-Methyl-dodecane	33.5	44.1	213	-60
C14	n-Octyl-benzene	33.9	39.8	284	-39
	n-Octyl-cyclohexane	35.5	43.5	280	-20
	n-Tetradecane	33.8	44.1	279	6
	5-Methyl-tetradecane	33.8	44.1	222	-51

2.2.2 Jet fuel properties [4]

Due to the safety reasons, the properties of the jet fuel is therefore more strictly controlled than other fuels. Currently, there are 3 standards for jet fuel specification: ASTM-D1655, Defense Standard 91-91 (DEFSTAN91-91), and IATA. According to these standards, the properties of aviation fuels in terms of volatility, fluidity, combustion properties, corrosion, chemical stability, thermal stability, contaminant and additives are specified for common jet fuels produced from fossil ones. In the case of alternative jet fuel or aircraft biofuels, they use the criteria of ASTM D7566 for controlling the properties of jet fuels as summarized in Table 2.2.

Table 2.2 Jet fuel specifications [4]

jet A-1	ASTM D1655-04a	IATA	Def stan 91-91	ASTM D7566
composition				
acidity, total (mg KOH/g)	0.1, max	0.015, max	0.1, max	0.1, max
Aromatics (vol%)	25, max	25, max	25, max(8, min)	25, max(8, min)
Sulfur, total (wt%)	0.3, max	0.3, max	0.3, max	0.3, max
Volatility				
Distillation temperature:				
10% Recovery (°C)	205, max	205, max	205, max	205, max
20% Recovery (°C)	-	-	-	-
50% Recovery (°C)	-	-	-	(15, min)
90% Recovery (°C)	-	-	-	(40, min)
Final BP (°C)	300, max	300, max	300, max	300, max
Flash point (°C)	38, min	38, min	38, min	38, min
Density @ 15°C (kg/m ³)	775-840	775-840	775-840	775-840
Fluidity				
freezing point(°C), max	-47	-47	-47	-40 Jet A; -47 Jet A-1
Viscosity @ 20°C(cSt)	8, max	8, max	8, max	8, max
combustion				
Net heat of comb.(MJ/kg)	42.8, min	42.8, min	42.8, min	42.8, min
smoke point (nm)	25, min	25, min	25, min	25, min
Smoke point (nm) and naphthalenes(vol%)	19 (min), 3 (max)	19 (min), 3 (max)	19 (min), 3 (max)	18 (min), 3 (max)
Thermal stability				
JFTOT Delta P@260°C (mm Hg)	25, max	25, max	25, max	25, max
Tube deposit Rating (visual)	<3	<3	<3	<3
Conductivity				
conductivity (pS/m)	50-450	50-450	50-600	-
Lubricity				
BOCLE wear scar diameter (nm)	-	0.85, max	0.85, max	0.85, max

2.2.3 Bio-jet fuels [4]

Biomass-derived jet fuels (bio-jet fuels) are a potential alternative way to replace the petroleum jet fuel. Many process technologies that can convert biomass-based materials into jet fuel substitutes are available for commercial or pre-commercial scale. Whereas, some technologies are still in the research and development stage. These technologies are varied and strongly depended on the types of feedstock. In the case of oil-based feedstocks, they can be converted to bio-jet fuels via hydroprocessing technologies, including hydrotreating, deoxygenation, and isomerization/hydrocracking. The catalytic hydrothermolysis (CH) has been developed to treat triglyceride-based oils. Solid-based feedstocks are converted to biomass derived intermediates via gasification. Moreover, alcohol or sugars can be converted as the bio-jet fuels or related additives via biochemical or thermochemical processes. The pyrolysis of solid biomass can also produce bio-oils. The produced syngas, alcohols, sugars, and bio-oils can be further upgraded to bio-jet fuels via a variety of synthesis such as fermentative, or catalytic processes. Among these technologies, the bio-jet fuels obtained from Fischer-Tropsch (F-T) synthesis and oil hydro-processing technologies have been approved by ASTM International (ASTM) Method D7566 for blending with fossil jet at levels up to 50%. Hydro-processing technologies using vegetable and waste oils are only conversion pathways that are ready for the large-scale deployment.

2.2.4 Sustainable aviation fuel productions and feedstocks [28]

The main feedstocks and SAF conversion processes have already been approved to produce bio-jet fuel. ASTM international have certified alternative fuels from six conversion processes under the standard ASTM D7566 (Table 2.3):

- (1) Synthesized paraffinic kerosene (SPK) from the Fischer-Tropsch process (FT-SPK)
- (2) SPK from hydro-processed esters and fatty acids process (HEFA-SPK)

(3) Synthetic iso-paraffins (SIP) from hydro-processed fermented Sugars (HFS-SIP)

(4) SPK from the alcohol-to-jet process (ATJ-SPK),

(5) Synthesized kerosene with aromatics derived by alkylation of light aromatics from non-petroleum sources (FT-SPK/A)

(6) Co-processing.

Table 2.3 Conversion processes of SAF approved by ASTM international [28]

Conversion process	Abbreviation	Possible feedstocks	Blending ratio by volume	Commercialization proposals
Fischer-Tropsch hydro-processed synthesized paraffinic kerosene	FT-SPK	Coal, natural gas, biomass	50%	Fulcrum Bioenergy, Red Rock Biofuels, SG Preston, Kaidi, Sasol, Shell, Syntroleum
Synthesized paraffinic kerosene produced from hydro-processed esters and fatty acids	HEFA-SPK	Bio-oils, animal fat, recycled oils	50%	World Energy, Honeywell UOP, Neste Oil, Dynamic Fuels, EERC
Synthesized iso-paraffins produced from hydro-processed fermented sugars	SIP-HFS	Biomass used for sugar production	10%	Amyris, Total
Synthesized kerosene with aromatics derived by alkylation of light aromatics from nonpetroleum sources	SPK/A	Coal, natural gas, biomass	50%	Sasol
Alcohol-to-jet synthetic paraffinic kerosene	ATJ-SPK	Biomass from ethanol or isobutanol production	50%	Gevo, Cobalt, Honeywell UOP, Lanzatech, Swedish Biofuels, Byogy
Co-processing	-	Fats, oils, and greases (FOG) from petroleum refining	5%	

The operating conditions for the sustainable aviation fuel production are depended on the fuel supply in different States, high safety requirements and demand strict quality assurance of fuel, based on globally accepted standards. To complement the general standard for aviation turbine fuels (ASTM D1655), every new process has to be certified and this standard is amended and incorporated in a new annex. As of December 2018, there were six conversion processes approved for SAF production under the standard ASTM D7566 and ASTM 1655, which specify blending limits for these fuels (as shown in Table 2.3). The first certified conversion process announced in 2009 was the FT-SPK derived from coal, natural gas or biomass. Its current restriction blend is 50% (in volume terms).

In 2011, the HEFA-SPK process was approved, with the same current restriction blend (ASTM, 2011). The HFS-SIP process, restricted to 10% by blend, was approved in 2014. In 2016, the ATJ-SPK process from isobutanol was certified, being eligible to be used up to 30% by blend (Gevo, 2016). In 2018, ASTM updated the maximum blend percentage to 50%, and added the possibility for co-processing fats, oils, and greases from petroleum refining (ICAO GFAAF, 2018).

In the bio-jet fuel production, four types of feedstocks can be used on these conversion processes such as Alcohol, oil, sugar/starch, and lignocellulosic feedstocks. For the Alcohol-to-jet (ATJ) process it is also called as alcohol oligomerization. The alcohol feedstock used in this process such as methanol, ethanol, butanol, and long-chain fatty alcohols. The biological and catalytic conversion of sugars to hydrocarbons provide a biochemical route to the production of liquid transportation fuels and chemicals. However, oil to jet conversion technology such as hydro-processing is at a relatively high maturity level and commercially available. The properties of bio-jet fuel obtained from the hydro-process is equivalent to the conventional petroleum. Moreover, the obtained bio-jet fuel has the advantages of the higher cetane number with lower aromatic content and sulfur contents, resulting in the potentially lower GHG emissions [4].

2.3 Hydro-processing [20]

The hydro-processing can be applied for the removal of sulfur, nitrogen, organometallic compounds, oxygen, and halide. The saturation of olefins and aromatic compounds will be simultaneously occurred. The hydrotreating reactions proceed in the following order: metal removal, olefin saturation, sulfur removal, nitrogen removal, oxygen removal, halide removal, and aromatic saturation. The hydroprocessing pathway is consisted of the chemical conversion of triglyceride feedstock through hydrodeoxygenation, hydroisomerization and hydrocracking to produce bio-jet fuels as shown in Fig. 2.1. The triglyceride feedstock is firstly converted to linear long chain hydrocarbons using a solid catalyst under high pressure and temperature. For the deoxygenation and decarbonylation, they are performed and generate water, carbon monoxide (CO) and carbon dioxide (CO₂) as byproducts. The linear long chain hydrocarbons produced in the first reactor are fed to a second one, where cracking and isomerization are occurred. In this step, the hydrocarbon chains are in the range between C₈ and C₁₆, corresponding to bio-jet fuels. Additionally, light gases, naphtha and green diesel are produced. Thus, the separation of the renewable hydrocarbons is required usually by means of distillation. Triglyceride feedstock involves with the natural oils produced from plants or animals can be converted to bio-fuels.

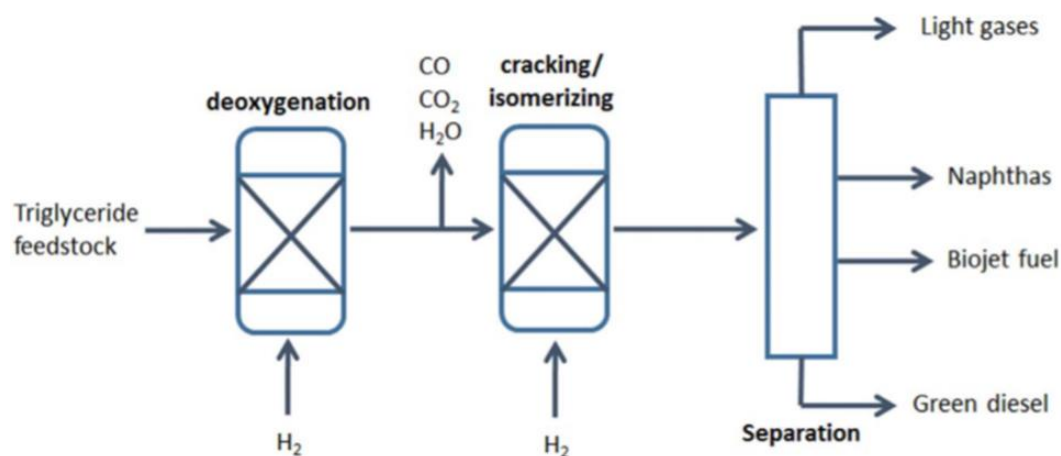


Fig. 2.2 Hydro-processing pathway of triglyceride [20]

Although biofuels can be made from a wide variety of feedstocks, triglyceride and free fatty acid (FFA) are useful for production of biofuels. It is important to know the general composition of the petroleum-based fuels that biofuels are intended to supplement or replace. Fatty acids and triglycerides are most commonly used to produce diesel and jet fuel (middle distillates) because their fatty acid carbon chains roughly match the carbon number profiles of typical petroleum diesel and jet fuels. If the fatty acid carbon chains are isolated and saturated with hydrogen and converted into paraffins, they can substitute the petroleum-based fuel quite well because the paraffins derived from fatty acids are virtually chemically indistinguishable from major components of petroleum diesel and jet fuels [31].

Several process technologies based on the concept of triglyceride, free fatty acid, or tall oil hydrotreatment have been developed to convert plant- and animal-based oils into biofuels. The following discussion reviews the major process steps required to complete this conversion, including the production of primarily triglyceride oils via typical vegetable oil refining, deoxygenation to produce fully hydrocarbon n-paraffins, and isomerization and cracking of n-paraffin to make biofuels [31].

2.4 Hydroisomerization [32]

Hydroisomerization of long chain paraffins for the production of branched alkanes has recently been intensively studied due to a large availability of these compounds. The most interesting research topics have been the development of novel bifunctional catalysts to maximize the yield of isomers and to suppress the cracking reactions. Since both of these reactions are catalyzed by Brønsted acid sites, the optimum catalyst exhibits equal amounts of metal and acid sites, and it facilitates the rapid mass transfer. Thus, several hierarchical and nano-shaped zeolites have been developed. The composite catalysts containing both micro- and mesoporous phases are also created. The effect of the reactant structure, optimal

reaction conditions, catalyst stability and comparison of batch vs continuous operations on the degree of isomerization have been investigated [33].

In hydroisomerization, the structure of the feedstock are transformed from normal hydrocarbons to branched ones having the same carbon number. Selective hydroisomerization is highly desired in oil refineries. This process involves the improvement of the octane number for the gasoline pool (C5–C6), and dewaxing of long-chain hydrocarbons for improvement in their cetane number and cold flow properties. However, they show the adverse fuel properties such as freezing and pour points. Whereas the branched alkanes have superior cold flow properties, and they do not compromise other properties of the fuel. In hydroisomerization of long-chain alkanes, several products are formed, such as light hydrocarbons (C1–C4), hydrocarbons in the gasoline range (C5–C8), jet fuels (C9–C14), and diesel (C15–C18). The pour point has been correlated with the product distribution in the hydroisomerization of hexadecane and presented as a function of conversion [10]. It has been reported that the pour point increased with increasing in the paraffin molecular weight, but its value decreased with increasing the level of branching.

2.5 Mesoporous zeolite [22]

From several years, substantial efforts have focused on the more effective utilization of zeolites in heterogeneously catalyzed reactions. The sub-optimal use of this class of aluminosilicates is implied by the limited access to, and diffusional constraints within, their micropores structure of zeolite. Mesoporous zeolites have received increasing attention due to their improved performance in catalytic reactions with respect to conventional (purely microporous) zeolites. Mesoporous zeolites can be prepared via many processes: synthesis mesopore zeolite and steaming, demetallization (dealumination & desilication). In practical, the resulting mesoporous zeolite materials can be categorized into three distinctly different types of materials such as hierarchical zeolite crystals, nanosized zeolite crystals, and

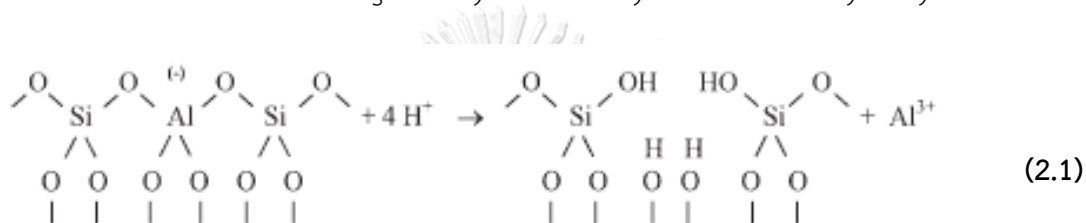
supported zeolite crystals. The hierarchical zeolite porosity appears in each individual zeolite crystal. Depending on their size, these additional pores are either mesopores (diameter below 50 nm) or macropores (diameter above 50 nm). Accordingly, the hierarchical zeolite crystals could be further categorized as either mesoporous or macroporous zeolite crystals.

2.5.1 Dealumination [34]

Dealumination of zeolite is one of the most important subjects in the field of zeolite secondary synthesis and modification. For decades, zeolite scientists have investigated dealumination routes and techniques in order to optimize the properties and functions of zeolites. Generally, there are three dealumination routes presented as follows:

- (1) Dealumination and ultra-stabilization of zeolites through high temperature thermal treatment and hydrothermal treatment.
- (2) Chemical dealumination route. This technique has been used for decades. It involves with the use of acids (including inorganic and organic acids) or alkalis salts in solution to react with the zeolite for dealumination, or other reagent involves with inorganic ligands such as F⁻.
- (3) Optimal combination of high-temperature hydrothermal and chemical dealumination routes. Zeolite dealumination not only increases the Si/Al ratio, but it also results in various extra-framework aluminum (EFAL) atoms in the pores, channels, and surfaces of zeolites. Furthermore, dealumination may also lead the framework defects, local structure collapse, or even blocking of some channels. As a result, the properties and functions of zeolites, especially their acidity, channel structures, and thermal stability and catalytic performance, may be changed, which is depended on the routes, methods, and conditions adopted for dealumination.

Removal of aluminum from a zeolite framework was first reported in 1964 by Barrer and Makki. They extracted aluminum from clinoptilolite by refluxing with hydrochloric acid. Depending on the acid concentration, up to 100% of the framework aluminum could be removed; However, the thermostability of the products gradually decreased when the dealumination degrees were higher than 65%. Dealumination with acids was accompanied by ion exchange of lattice cations by protons. The overall process was suggested to proceed according to Eq. 2.1 under the formation of defect sites generally denoted by the term of “hydroxyl nest”.



2.5.2 Desilication

The mesopores zeolites prepared by the alkaline-mediated leaching (base leaching) of framework Si has become a very attractive method due to the combination of both experimental simplicity and efficiency of the hierarchical zeolites obtained. The mesopores induced by alkaline treatment are interconnected and accessible from the external surface of the zeolite crystal representing a clear advantage for access-limited and diffusion-constrained reactions. The use of base leaching as a post-synthetic modification to increase zeolite performance in adsorption and catalysis was first patented by Dean Arthur Young in the 1960s. It was claimed that alkaline-treated mordenite displayed preserved crystallinity and a significantly increased benzene adsorption capacity. Moreover, catalytic evaluation in gas-oil hydrocracking revealed a 3 times higher conversion for an alkaline treated Pd/mordenite than for the untreated zeolite [22].

For example, alkaline treatment of ZSM-5 put intense effort into exploring the potential of mesoporous MFI (Fig. 2.4). They established optimal conditions (especially in terms of time and temperature) and claimed that the long-range order

and Brønsted acidity of the zeolite were mostly unchanged upon alkaline treatment. Additionally, the superiority of NaOH-treated zeolites in diffusion and catalysis compared to the corresponding purely microporous parents was demonstrated. On the other hand, by using a single ‘standard’ experimental desilication condition (0.2 M of NaOH, 65 °C, 30 min), they identified a significant limitation in the confined range of molar Si/Al ratios (25–50) for which optimal introduction of intracrystalline mesopores could be achieved. [23].

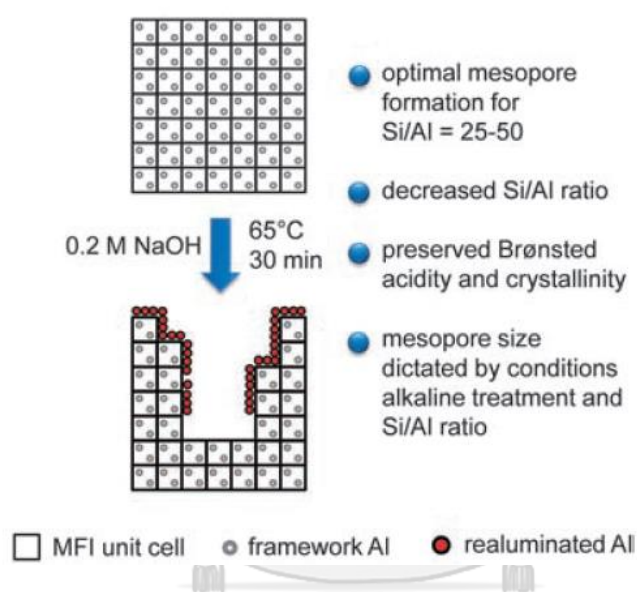


Fig. 2.3 Schematic representation of MFI desilication by NaOH treatment [23].

2.6 literature review

Sazama et al. [35] studied the use of Pt/H-BEA zeolite for isomerization of n-hexane. They described an attempt to understand the relations between the local arrangement of active sites and skeletal isomerization of n-hexane in order to adapt the structure of zeolite catalysts to increase the reaction rates of isomerization. For this purpose, they used a different structural topology such as Al-rich BEA zeolite synthesized by sol-gel method, commercial high-silica BEA zeolites and hierarchical mordenite zeolite prepared by desilication with NaOH. All the zeolites were ion-exchanged with 0.5 M NH_4NO_3 at room temperature. Pt was loading into the zeolites by incipient wetness impregnation. Pt catalyst supported on Al-rich H-BEA zeolite (Pt/H-BEA/4.2) gave the highest yield of iso-C₆ alkanes to 76.8% at 215 °C.

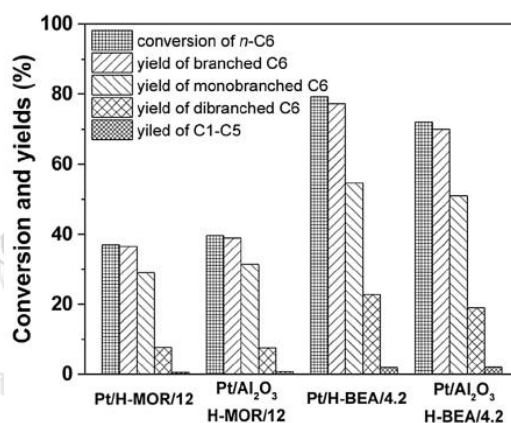


Fig. 2.4 Comparison of the conversions of n-hexane and the yields of branched C₆ isomers and C₁–C₅ by-products in the hydroisomerization reaction over*BEA and MOR catalysts with Pt introduced by a conventional incipient wetness impregnation (Pt/H-*BEA/4.2 and Pt/H-MOR/12) and the mechanical mixtures of the protonic form of zeolite (Pt/Al₂O₃(H-*BEA/4.2-Pt/Al₂O₃ and H-MOR/12-Pt/Al₂O₃)) at 225 °C.

Wang et al. [36] studied the hydrophilicity and hydrophobicity of zeolites. Acids leaching of natural zeolite changed $\text{SiO}_2/\text{Al}_2\text{O}_3$ ratios was performed by using nitric acid solution (0.1 to 3.0 M). It was found that 5.05–23.26 wt% aluminium were removed. In the case of alkali solution – NaOH (0.05 to 0.8 M), it could remove the silicon from the zeolite structure ca. 0.49–7.64 wt%. The treated zeolite by acid

leaching showed hydrophobicity with the enhancement of specific surface area. For the base leaching, the increase in the basic concentration decreased surface area. Water vapor adsorption on the untreated zeolite sample was 0.74 mg/m^2 . The water adsorption on zeolite sample gradually increased decreasing the $\text{SiO}_2/\text{Al}_2\text{O}_3$ ratio. The water adsorptions on 0.05–0.70 M alkali treated zeolites having $\text{SiO}_2/\text{Al}_2\text{O}_3$ ratios between 5.44 and 5.87 was $0.83\text{--}1.45 \text{ mg/m}^2$, while the adsorption of water vapor on 0.05–3.00 M acid treated zeolites ($\text{SiO}_2/\text{Al}_2\text{O}_3$ ratios = 6.18–7.66) was $0.27\text{--}0.54 \text{ mg/m}^2$. This result showed that hydrophilicity/hydrophobicity of zeolite was highly related to the $\text{SiO}_2/\text{Al}_2\text{O}_3$ ratio.

Natalia et al. [37] studied the expansion of the pores of beta zeolite using various hydrofluoric acid concentrations in ammonium fluoride (NH_4F) solution at room temperature and 40°C . This process increased the Si/Al ratio from 20 to 22–34 and the pore size of the modified beta zeolite was in the range (5–20 nm). The highest Si/Al ratio and pore size range of dealuminated beta zeolite was prepared with 1.00 M HF in NH_4F solution at 40°C for 30 min. Beta zeolite before and after dealumination by using HF/ NH_4F solution were applied in isomerization and disproportionation of meta-xylene (m-xylene) carried out in a glass fixed-bed reactor, under atmospheric pressure at 350°C for converting to trimethyl benzenes (TMB). The $\text{N}_2/\text{m-xylene}$ molar ratio was 4 (130 mL/min total flow). However, the total concentration of Bronsted and Lewis sites remained unchanged when dealumination was conducted with 0.50 M HF concentration. Thus, the beta zeolite dealuminated by 0.20–0.50 M was applied in the catalytic reaction. Although the %conversion of m-xylene obtained from the system using dealuminated beta zeolite were lower than that of the parent Beta zeolite, the 1,2,4 TMB selectivity generated from the use of dealuminated zeolite prepared by 0.50 M HF for 5 min at room temperature was increased from 7.96% to 8.76% with 14.8% m-xylene conversion.

Yu et al. [38] studied catalytic cracking under N_2 atmosphere via mesopore IM-5 zeolite prepared by alkaline treatment. The level of desilication of IM-5 zeolite

was depended on the stirring time (0.5-4 h) at 70 °C. From the ^{29}Si MAS NMR, spectrum of mesoporous IM-5, the Si(4Si,0Al) units were preferentially removed from the IM-5 framework during the alkaline treatment and a small amount of the framework Al was eluted. Meanwhile, the desilication resulted in the loss of strong acid sites. Under the optimal conditions, the mesopore volume of mesoporous IM-5 increased relatively by 178% from 0.11 cm³/g of the untreated IM-5 to 0.31 cm³/g, while the micropore volume slightly decreased. This reflected that its microporous structure was mostly preserved. Although introducing mesopores decreased the acid amount of IM-5, it possessed better diffusion performance. Thus, mesoporous IM-5 exhibited the higher yield of light olefins (especially propylene) and catalyst lifetime in catalyzing n-alkane than conventional IM-5 and ZSM-5. Furthermore, the higher gasoline yield and lower coke formation over mesoporous IM-5 were obtained when compared to the conventional IM-5 in the heavy oil cracking. To compare with ZSM-5 with the same SiO₂/Al₂O₃ ratio, the higher acid strength and higher amount of Bronsted acid sites gave mesoporous IM-5 had more B acid site give IM-5 better catalytic performance with higher catalytic activity and higher yields for light olefins and iso-butane.

Tamizhdurai et al. [39] studied the performance of the Pt supported on mordenite modified by dealumination for isomerization of n-hexane, n-pentane and light naphtha. Dealuminated mordenite was prepared by using hydrochloric acid (HCl) at 100 °C for 0.5, 1.0 and 3.0 h. A dealumination at 0.5 h, the crystallinity of the modified mordenite was approximately 17% and increased to 37% when dealumination was allowed for 1.5 h. The result obtained from high-resolution-scanning electron microscopy (HR-SEM), and high-resolution transmission electron microscopy (HR-TEM) showed the more roughness of dealuminated mordenite with higher Pt dispersion. The modified mordenite with Si/Al ratio of 40 was reactive for hydroisomerization of n-hexane and light naphtha due to the higher specific surface area. The result of obtained from NH₃ temperature programmed desorption (NH₃-TPD), the increasing time of dealumination decreased the acidity on the modified mordenite. Pt/unmodified mordenite had very low iso-pentane (28%) and iso-hexane

(26%) when the reaction was performed at 180 °C. Whereas, Pt/dealuminated mordenite (Si/Al ratio = 40) promoted hydroisomerization of n-pentene and n-hexane at 250 °C to achieve the highest %conversion to 88% for n-pentane and 91.4% for n-hexane.



CHAPTER 3

EXPERIMENTAL

This chapter includes the information of chemicals, materials, instrument, experimental procedure and analysis of products.

3.1 Materials

1. Palm oil (refined palm olein, Morakot Industries Co., Ltd., Thailand)
2. Jet A-1 (jet fuel, JETA-1 grade, PTT Public Co., Ltd., Thailand)
3. Nickel (II) nitrate hexahydrate, $(\text{Ni}(\text{NO}_3)_2 \cdot 6\text{H}_2\text{O})$ (AR grade, Ajax Finechem Pty Ltd., Australia)
4. Ammonium-beta zeolite (NH_4 -Beta zeolite) (TOSOH Co., Ltd., Japan)
5. Hydrofluoric acid (HF) (AR grade, QRëC, New Zealand)
6. Ammonium fluoride (NH_4F) (AR grade, VWR International, LLC., USA)
7. Sodium hydroxide (NaOH) (1.0N volumetric solution, Molecule Co., Ltd., Thailand)
8. Hydrogen gas (H_2) (99.99% purity, Bangkok Industrial Gas Co., Ltd., Thailand)
9. Nitrogen gas (N_2) (99.99% purity, Bangkok Industrial Gas Co., Ltd., Thailand)
10. Oxygen gas (O_2) (99.99% purity, Bangkok Industrial Gas Co., Ltd., Thailand)
11. Helium gas (He) (99% purity, Praxair Co., Ltd., Thailand)
12. Argon gas (Ar) (99.95% purity, Bangkok Industrial Gas Co., Ltd., Thailand)
13. Hydrogen in Argon gas (5% (V/V) H_2/Ar gas, Bangkok Industrial Gas Co., Ltd., Thailand)
14. Ammonia in Helium gas (5% (V/V) NH_3/He gas, Bangkok Industrial Gas Co., Ltd., Thailand)
15. Hydrochloric acid (HCl) (AR grade, QRëC, New Zealand)
16. Nitric acid (HNO_3) (AR grade, QRëC, New Zealand)
17. Acetone (AR grade, QRëC, New Zealand)

3.2 Instruments

1. Stainless steel high pressure reactor 300mL (Parr, Germany)
2. Vacuum rotary evaporator (Heidolph, Germany)
3. Vacuum pump (Ilmvac, model MPC 105T, country)
4. Oven (Binder, model ED115, USA)
5. Muffle furnace (Carbolite, model CWF-1300, Germany)
6. Hot plate and stirrer (IKA, C-MAG HS, China)
7. Buchner funnel filtration apparatus
8. Micro syringe 10 μL
9. Scanning electron microscopy (SEM) (JEOL, model JSM-6400, Japan)
10. Surface area analyzer (Quantachrome, model ASiQwin, USA)
11. Chemisorption analyzer (MicrotracBEL, model BELCAT II, Japan)
12. X-ray diffraction (XRD) (Bruker, model D8 advance, USA)
13. Thermogravimetric analyzer (TGA) (Perkin Elmer Inc., model TGA8000, USA)
14. Gas chromatography – mass spectrometer (GC-MS) (Shimadzu, model QP2010A, Japan) equipped with DB-5MS column ($\varnothing=0.25$ mm., L=60 m.)
15. Fourier transform infrared spectrometer (Thermo Fisher Scientific, model Nicolet iS10, country)
16. Scanning electron microscopy with energy dispersive spectroscopy (SEM-EDS) (JEOL, model JSM-5480LV, Japan)
17. Inductively coupled plasma - optical emission spectrometry (ICP-OES) (Perkin Elmer Inc., AVIO 200, USA)
18. Solid state - nuclear magnetic resonance spectrometer (solid state - NMR) (BRUKER, AVANCE III HD-Ascend 400 WB, USA)
19. CHN analyzer (model PE 2410, PerkinElmer, USA)
20. Differential scanning calorimeter (DSC) (model DSC822, METTLER, USA)

3.3 Experiment

3.3.1 Preparation of treated supports

3.3.1.1 Dealumination [37]

NH₄-beta zeolite (10 g) was dealuminated via acid treatment using 0.25–0.75 M HF solutions (60 mL) containing 10 g NH₄F. The mixture was stirred at room temperature for 1 h. The dealuminated zeolite was washed with deionized water and centrifuged several times until neutral and then dried at 110 °C for 24 h before calcination at 550°C for 4 h. The dealuminated zeolites were denoted following the HF concentrations: beta-0.25M-deA, beta-0.50M-deA and beta-0.75M-deA.

3.3.1.2 Desilication [40]

NH₄-zeolite (10 g) was desilicated using 60 mL NaOH solutions with concentrations in the range of 0.25–0.75 M. The mixture was stirred at room temperature for 1 h. The desilicated zeolite was neutralized to pH 7 by adding 1 M hydrochloric acid and centrifuged to obtain the solid sample. Then, the treated zeolite was dried at 110 °C for 24 h and calcinated at 550 °C for 4 h. The prepared samples were denoted according to the concentration of NaOH solution: beta-0.25M-deS, beta-0.50M-deS and beta-0.75M-deS.

3.3.2 Catalyst preparation

10 wt% nickel (Ni) catalysts supported on the prepared zeolites were synthesized via incipient wetness impregnation method. Briefly, 2.75 g Ni (NO₃)₂·6H₂O dissolved in DI water (5.5 mL) was dropped to 5 g treated zeolites, dried at 110 °C overnight and then calcined at 550 °C for 4 h. The calcined catalyst was *ex-situ* reduced in a horizontal tubular furnace at 600 °C for 2 h under H₂ atmosphere at a flow rate of 10 mL/min. Then, the reduced catalyst was passivated using O₂/N₂ mixed gas (5% O₂) at a flow rate of 0.2 L/h at room temperature for 2 h before use.

3.3.3 Hydroisomerization of palm olein

Hydroisomerization of palm olein was performed in a stainless-steel high-pressure reactor (Parr instrument company). After loading the passivated catalyst (1.25 g/batch) into the reactor, the refined palm olein (25 mL or 22 g) was charged into the reactor using a syringe. Then, the system was purged by using H₂ gas for 30 min to remove air. After pressuring to the desired initial H₂ pressure, the reaction was performed at 340 °C for a given reaction time under agitation with a stirring rate of 200 rpm. When the reaction was ceased, the liquid and solid products were separated by using the buchner funnel filtration. Whereas, the gaseous product was collected in gas bag when the system was cooled down to 40 °C.

3.3.4 Catalyst characterization

3.3.4.1 Scanning electron microscopy equipped with energy dispersive spectroscopy (SEM-EDS)

The surface morphology of the calcined catalysts and Si/Al atomic ratio of zeolite supports before and after treating were investigated by using SEM-EDS (JEOL, model JSM-5480LV) (Fig 3.1). The scanning microscope was operated at an accelerating voltage of 15 kV. Before analysis, the samples were sputter-coated with gold for increasing a conductivity.



Fig. 3.1 Scanning Electron Microscopy with Energy Dispersive Spectroscopy (SEM-EDS) (JEOL, model JSM-5480LV)

3.3.4.2 Textural properties of zeolites and Ni-based catalysts

The Brunauer-Emmett-Teller (BET) specific surface area, microporous and mesoporous pore volume, pore radius of the supports and catalysts were analyzed by N₂ physisorption at -196 °C (Surface area analyzer (Quantachrome, model ASiQwin) (Fig. 3.2). Before measurement, the sample was degassed under high vacuum at 250 °C for 25 h. The specific surface area was calculated using BET method in the relative pressure range of $0 < P/P_0 < 0.06$. The total pore volume and the pore size distributions were obtained from the desorption branch and calculated by the Barrett Joyner-Halenda (BJH) method at a relative pressure (P/P_0) of 0.99 [41]

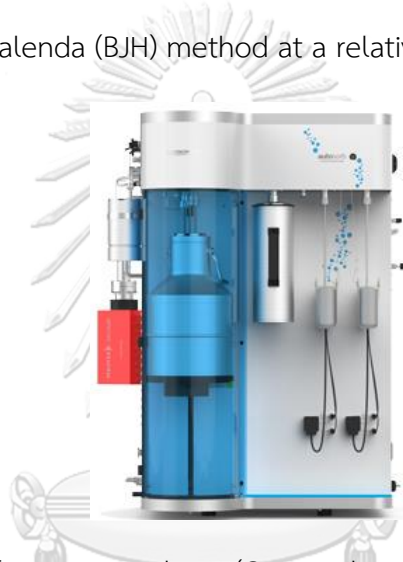


Fig. 3.2 Surface area analyzer (Quantachrome, model ASiQwin)

3.3.4.3 Transmission electron microscopy (TEM)

The particle size and dispersion degree of Nickel oxide (NiO) deposited on the surface of zeolite were examined using TEM (JEOL, model JEM1400) (Fig. 3.3) operated at an accelerating voltage of 80 kV with 100,000x magnification. Before analysis, the catalysts were dispersed in methanol then dropped on the grid to fix sample.



Fig. 3.3 Transmission electron microscopy (TEM) (JEOL, model JEM1400)

3.3.4.4 X-rays diffraction patterns of modified zeolite supports and Ni-based catalysts

The X-ray diffraction patterns of NH_4 -beta zeolite before and after dealumination and desilication were examined by X-ray diffractometer (Bruker, model D8 advance) (Fig. 3.4). It was operated using CuK α radiation $\lambda = 1.5406 \text{ \AA}$ and an X-ray power of 40 kV and 40 mA. The measurement was started from $2\theta = 5^\circ$ to 80° with a scanning step of 0.0197 and a count time of 1 sec to identify the type and dispersion of crystalline on the surface of the samples. The signals appeared in the XRD pattern were identified by comparison with the standard in a database and previous literatures. The crystallite size of NiO in each catalysts was calculated following Scherrer Equation as shown in Eq. 3.1 [42]

$$d_p = \frac{k\lambda}{\beta \cos\theta} \quad (3.1)$$

d_p = crystallite size (nm)

λ = X-ray wavelength (nm) at 0.15406 nm

β = full width at half maximum (FWHM)

K = Scherrer constant at 0.9



Fig. 3.4 X-ray diffractometer (XRD) (Bruker, model D8 advance)

3.3.4.5 Solid state nuclear magnetic resonance (NMR) spectroscopy

^{27}Al MAS NMR spectra were recorded on a Bruker Avance III 400WB spectrometer ($B_0 = 9.4$ T) using a 4 mm cylindrical zirconia rotor and spun at a spinning frequency of 104.3 MHz. Acquisition parameters are a pulse duration of 0.5 ms corresponding to a flip angle of $\pi/12$ and a 0.5 s recycle delay. ^{27}Al chemical shifts were relative to an aqueous solution of aluminum nitrate ($\text{AlCl}_3 \cdot 6\text{H}_2\text{O}$) [43].

^{29}Si NMR spectra were recorded at 99.4 MHz with a Bruker Avance III 400WB spectrometer and 4 mm zirconia rotors. Chemical shifts of silicon were measured by reference to tetramethylsilane. ^{29}Si MAS NMR spectra were obtained with 5 kHz rotors spinning speed, 3 μs excitation pulse duration and 10 s recycle delay. 3-(Trimethylsilyl)-1-propanosulfonic sodium salt was used for setting the Hartmann–Hahn condition. The proton $\pi/2$ pulse duration, the contact time and recycle delay were 6.35 μs , 5 ms and 5 s, respectively [44].



Fig. 3.5 Nuclear magnetic resonance spectrometer (solid state - NMR) (BRUKER, AVANCE III HD-Ascend 400 WB).

3.3.4.6 NH₃ Temperature programmed desorption (NH₃-TPD)

The acidity of the supports and catalysts was measured by using chemisorption analyzer (BELCAT II, MicrotracBEL) (Fig. 3.6). Before evaluation, the samples were heated to 500 °C for 1 h under He gas flow to remove water and impurities on the catalyst surface. After cooling down to 100 °C, NH₃/He gas (5% (v/v)) at a flow rate of 30 mL/min was fed into the samples cell for 30 min. Then, the adsorbed and non-adsorbed NH₃ were removed by purging with He gas at 100 °C (flow rate =50 mL/min) for 30 min followed by rising the temperature from 100 °C to 900°C at a heating rate of 10 °C/min. The quantity of NH₃ eluted from the NH₃-adsorbed surface was determined by using a thermal conductivity detector (TCD).



Fig. 3.6 Chemisorption analyzer (MicrotracBEL, model BELCAT II).

3.3.4.7 Fourier transform infrared spectra of pyridine adsorption (py-FTIR)

In order to quantify the Bronsted and Lewis acidic sites of each zeolite surfaces, the calcined NH_4 -beta zeolites before and after surface treatments were characterized by py-FTIR spectroscopy on the sample surfaces. The Bronsted and Lewis acid sites of samples were calculated from the FTIR profiles obtained from Fourier transform infrared spectrometer (Thermo Fisher Scientific, model Nicolet iS10) (Fig. 3.7). Before analysis, the sample (35 mg) was shaped as pellet (1cm) followed by heating at 500 °C for 1 h. After cooling down to 50 °C, pyridine was charged into the sample cell for 30 min. The absorbance peaks appeared at the wavelength in the range of 1,450-1,550 cm^{-1} were attributed to the Bronsted (B) and Lewis (L) acid peaks. The amount of each type of acid site was calculated following Eq. 3.2-3.3 [45].

$$C(\text{pyridine on B sites}) = \frac{1.88 \text{ IA(B)} R^2}{W} \quad (3.2)$$

$$C(\text{pyridine on L sites}) = \frac{1.42 \text{ IA(L)} R^2}{W} \quad (3.3)$$

C = concentration ($\text{mmol/g}_{\text{catalyst}}$)

IA(B,L) = integrated absorbance area of B or L band (cm^{-1})

R = radius of catalyst disk (cm)

W = weight of disk (mg)

3.3.4.8 Hydrogen temperature programmed reduction (H₂-TPR)

The reduction temperature in the presence of H₂ atmosphere for all catalysts was evaluated by using chemisorption analyzer (BELCAT II, MicrotracBEL). The integrated area of the TPR profile was the total consumed H₂ volume. Typically, 0.05 g each calcined catalyst was pretreated under Ar atmosphere at a flow rate of 30 mL/min and 500 °C for 30 min to remove impurities and moisture. The reduction step in the presence of H₂/N₂ mix gas (5 vol% H₂) gas at a flow rate of 30 mL/min was then operated from ambient temperature to 900 °C with a heating rate of 10 °C/min.

3.3.4.9 Actual NiO content supported on beta zeolites

Inductively coupled plasma - optical emission spectrometry (ICP-OES) (Perkin Elmer Inc., AVIO 200, USA) (Fig. 3.7) was used to evaluate the actual metal contents in each catalyst. Before analysis, 40 mg sample was digested in 10 mL HNO₃ /HCl solution (1/3 (v/v)), which was adjusted to achieve 50 mL (800 ppm sample). This solution was diluted again using DI water to obtain the concentration of 5 ppm sample. The amounts of digested Ni in the acid solution was obtained from the calibration curve prepared from the plasma-grade single-element standards.



Fig. 3.7 Inductively coupled plasma - optical emission spectrometry (ICP-OES) (Perkin Elmer Inc., AVIO 200).

3.3.4.10 Ni metal dispersion on zeolite before and after dealumination and desilication

CO pulse adsorption measurements were performed using Chemisorption analyzer (MicrotracBEL, model BELCAT II) The sample was heated to 673 K in an oxygen flow and held at this temperature for 15 min. After purging with He, the sample was reduced in mix H₂/N₂ gas (5 %(v/v)) for 120 min and then cooled to 40 °C in a helium flow. CO pulses were injected at that temperature until the adsorption reached saturation. The concentration of the CO pulse was determined by a thermal conductivity detector (TCD). The outlet gas was monitored also by a mass spectrometer (ULVAC, MMC-200). The amount of CO adsorption was calculated as the difference between the total amount of CO injected and the amount measured at the outlet from the sample. The metal dispersion was calculated by assuming a CO to surface metal atom ratio of 1:1.

3.3.5. Characterization of products

3.3.5.1 Coke deposition on catalyst surface

Thermogravimetric analyzer (TGA8000, PerkinElmer) (Fig. 3.8) was used to evaluate the weight loss of the spent catalysts, which was defined as the amount of coke deposited on the surface of catalysts after the reaction. The spent catalyst (5.0 mg) was heated from 30°C to 900 °C with a heating rate 10 °C/min under 30 mL/min O₂ gas flow rate and then cooled down to room temperature.

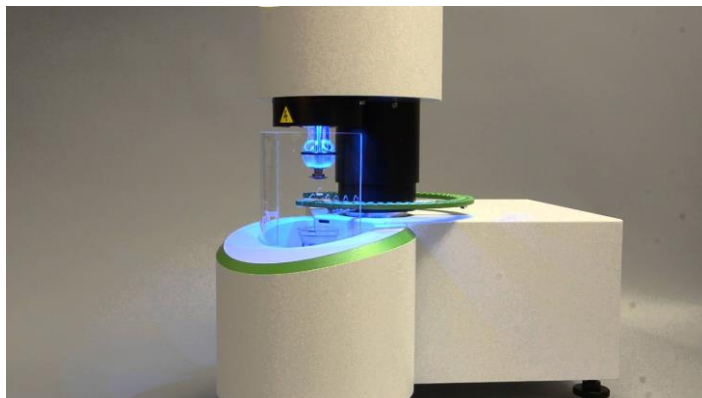


Fig. 3.8 Thermo gravimetric analyzer (TGA) (model TGA8000, PerkinElmer).

3.3.5.2 Chemical composition in liquid products

Before evaluation, the liquid products was diluted in acetone to a concentration of 800 ppm. Then, the mixture (1 μL) was injected into the gas chromatography mass spectrometer (Shimadzu-2010) (Fig. 3.9) equipped with a DB-5 column ($\varnothing=0.25\text{mm}$, $L=30\text{m}$) for separation and indication of the chemical species found in the obtained liquid products. The temperature of injector was 270 $^{\circ}\text{C}$ and the split ratio of 1:100 was applied. The oven temperature was controlled at 40 $^{\circ}\text{C}$ for 3 min and then increased to 200 $^{\circ}\text{C}$ at a heating rate of 5 $^{\circ}\text{C}/\text{min}$. Subsequently, the temperature of oven was increased to 280 $^{\circ}\text{C}$ with a heating rate of 15 $^{\circ}\text{C}/\text{min}$ and held at this temperature for 15 min. The detector temperature was controlled at 230 $^{\circ}\text{C}$.



Fig. 3.9 Gas chromatography mass spectrometer (model Shimadzu-2010, Shimadzu).

3.3.5.3 Heating value of liquid products

The Higher heating value (HHV) and lower heating value (LHV) analysis for liquid product were calculated using Dulong's equation is shown in Eq. 3.4. The calculation is based on the weight ratio of the carbon, hydrogen and oxygen elements in the biofuels by using CHN analyzer (model PE 2410, PerkinElmer) (Fig. 3.10). Heating values can be reported as higher and lower heating value, HHV (gross) and LHV (net), respectively. The difference between HHV and LHV is equal to the heat of vaporization of water formed by combustion of the fuel. The high heating values in this study were obtained from calculation by Dulong as shown in Eq. 3.4 and the low heating values were calculated by the Eq. 3.5 proposed by Oasmaa [46].

$$\text{HHV (MJ/kg)} = \frac{338.2 \times 1442.8 \times \left(\frac{C}{100} + \frac{H}{8} - \frac{O}{8} \right)}{1000} \quad (3.4)$$

$$\text{LHV (MJ/kg)} = \text{HHV} - (0.218 \times H) \quad (3.5)$$



Fig. 3.10 CHN analyzer (model PE 2410, PerkinElmer).

3.3.5.4 Freezing point of liquid products

The freezing point of the liquid product was analyzed by using differential scanning calorimeter (DSC) model DSC822 (METTLER) as shown in Fig. 3.11. The phase transformation from liquid to solid of the liquid sample was detected from the exothermic heat. The evaluation was conducted from 25 °C to -100°C on aluminium pan under atmospheric condition.



Fig. 3.11 Differential scanning calorimeter (DSC) model DSC822 (METTLER).



CHAPTER 4

RESULTS AND DISCUSSION

4.1 The effect of dealumination on hydroisomerization of palm olein

4.1.1 Characterization of beta zeolite supports before and after dealumination

Fig. 4.1 shows the N₂ adsorption–desorption isotherms of beta zeolite before and after dealumination using HF/NH₄F solution at different HF concentrations. The results obtained from the testing were summarized in Table 4.1. It was observed that the parent beta zeolite after calcination showed the N₂ adsorption isotherm to an adsorbed quantity of 430 cm³/g at high P/P₀ value (Fig. 4.1a). This resulted from the high external surface area (283 cm³/g) generated from the interparticle mesoporous formed from the aggregation of the small crystallites in the beta zeolite [19, 47].

After dealumination, the hysteresis loop of the dealuminated beta zeolite was shifted from the P/P₀ of 0.40-0.80 to 0.50-0.95 (Fig. 4.1b-4.1d). Moreover, the continuous N₂ adsorption isotherms for all dealuminated beta zeolites reached the high value of adsorbed quantity to 450-530 cm³/g depended on the HF concentration. This behavior exhibited the mesopore characteristics. The increase in the HF concentration in the HF/NH₄F solution from 0.25-0.75 M remarkably decreased the BET surface area (S_{BET}) from 673 to 583 cm³/g and external surface area (S_{external}) from 283 to 182 cm³/g. This indicated that non-microporous area decreased with slightly higher micropore area after dealumination due to the Al leaching. To consider the pore volume of the zeolites, the pore volume of mesopore (V_{BJH}) increased resulting in the higher total pore volume. The use of HF/NH₄F solution with 0.25 M HF concentration provided the modified zeolite with the highest total pore volume and mesopore volume at 0.81 and 0.65 cm³/g, respectively. The dealumination also expanded the average and BJH pore radius of zeolite from 19.8 and 3.87 Å to 26.3 and 3.94 Å, respectively. This exhibited that the use of 0.25 M HF concentration in the HF/NH₄F solution had the highest efficiency to enlarge the micropore of beta zeolite to the mesoporous material.

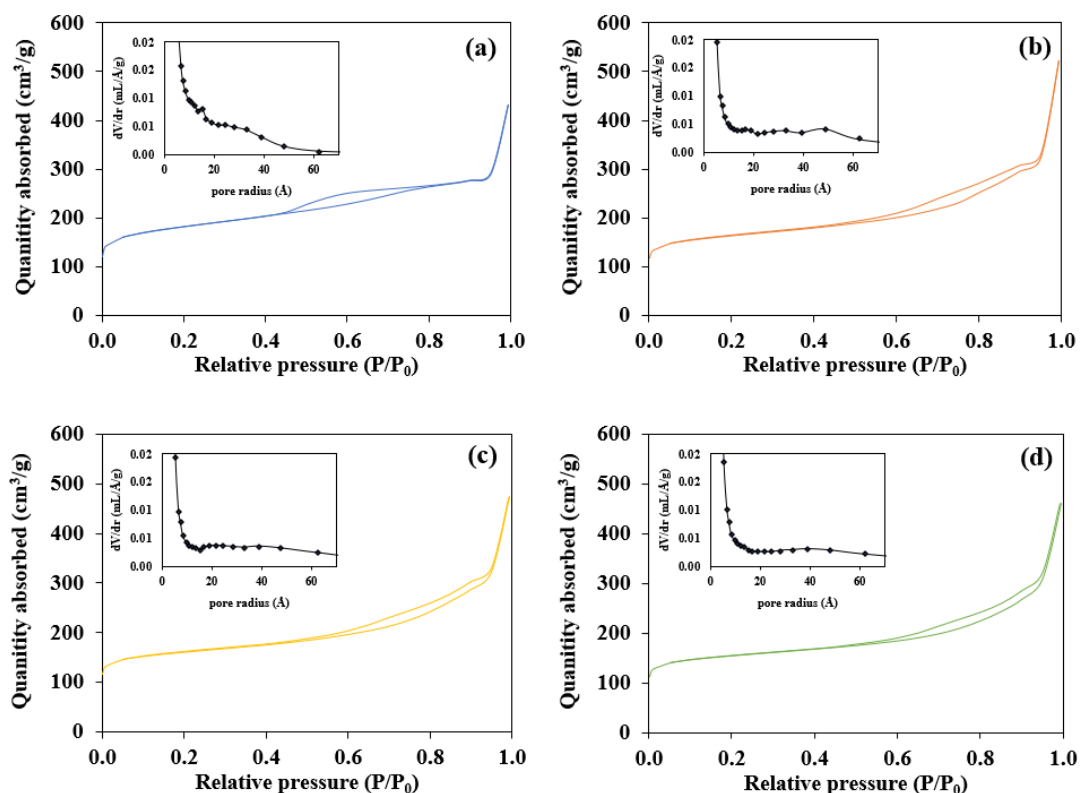


Fig. 4.1 N_2 adsorption-desorption isotherm and pore size distribution of (a) beta, (b) beta-0.25M-deA, (c) beta-0.50M-deA, and (d) beta-0.75M-deA.

Table 4.1 Textural properties of beta zeolite before and after dealumination

Samples	Surface area (m^2/g)			Pore volume (cm^3/g)			Pore radius (\AA)		RC	d_{302} (\AA)
	S^a_{BET}	S^b_{micro}	$S^c_{external}$	V^d_{micro}	V^e_{BJH}	V^f_{total}	R^g_{avg}	R^h_{BJH}		
beta	673	390	283	0.16	0.50	0.67	19.8	3.87	100	3.97
beta-0.25M-deA	615	405	209	0.16	0.65	0.81	26.3	3.94	108	3.93
beta-0.50M-deA	610	416	194	0.16	0.57	0.73	24.1	3.93	106	3.95
beta-0.75M-deA	583	401	182	0.16	0.56	0.72	24.4	3.94	111	3.94

^a MultiPoint BET method

^b t-method micropore surface area

^c t-method external surface area

^d micropore volume was obtained using t-plot method.

^e mesopore volume was obtained from BJH method cumulative desorption

^f Total pore volume for pores with Radius less than 1755.00 \AA at $P/P_0 = 0.994517$

^g Average pore radius

^h Pore radius was obtained from BJH method.

Fig. 4.2 shows the XRD patterns of beta zeolites before and after treating with HF/NH₄F solution with different HF concentrations. It was observed that all treated samples also remained the BEA-type structure [48, 49]. The integrated intensity of the diffraction peak at 2 θ of 22.4° was used to calculate the relative crystallinity (RC) of the samples [50]. Before acid treatment, the beta zeolite had 100% RC as shown in the Table 4.1. The dealumination by using HF/NH₄F solution increased the RC values of beta zeolite to 106-115% with increasing the HF concentrations. This phenomenon was also observed in the dealumination of HZSM-5 by using citric acid and oxalic acid [24]. They explained that the acid treatment removed the extra-framework Al and other amorphous substances in the zeolites resulting in the enhancement of overall crystallinity. The decrease in the d₃₀₂ spacing of beta zeolite after upon dealumination indicated some relaxation of beta zeolite matrix, which could strongly suggest the removal of Al atom from the beta zeolite framework [51].

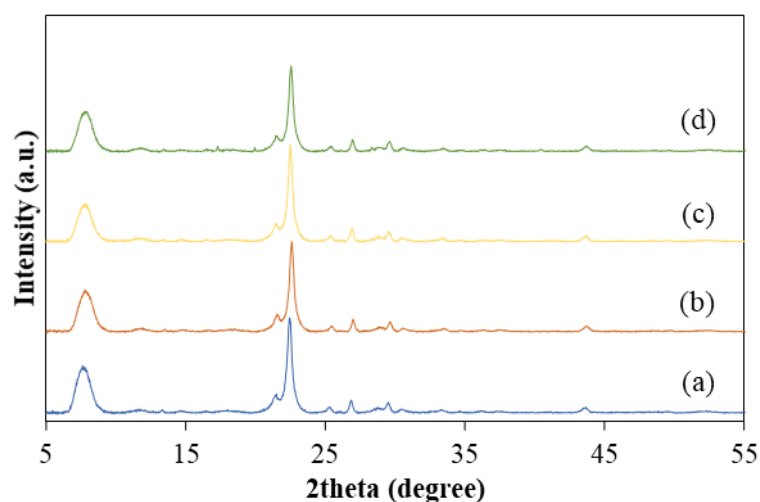


Fig. 4.2 XRD pattern of parent zeolite and dealuminated zeolites (a) beta, (b) beta-0.25M-deA, (c) beta-0.50M-deA, and (d) beta-0.75M-deA.

²⁷Al MAS NMR spectra of beta zeolite before and after dealumination were depicted in Fig. 4.3. The signal at 0 ppm was the extra-framework octahedral Al species [52]. The sharp peak was the characteristics of the well-ordered octahedral form, while the broad one indicated the distorted octahedral Al species [52]. The

signals appeared in the range of 40-65 ppm were assigned as the tetrahedral Al species [52]. Whereas the frameworks of the Al atoms occupying T1-T2 and T3-T9 sites exhibited the signal at 54 ppm and 57 ppm, respectively [52]. The signal of extra-framework tetrahedral Al species was also located at 63 ppm [52].

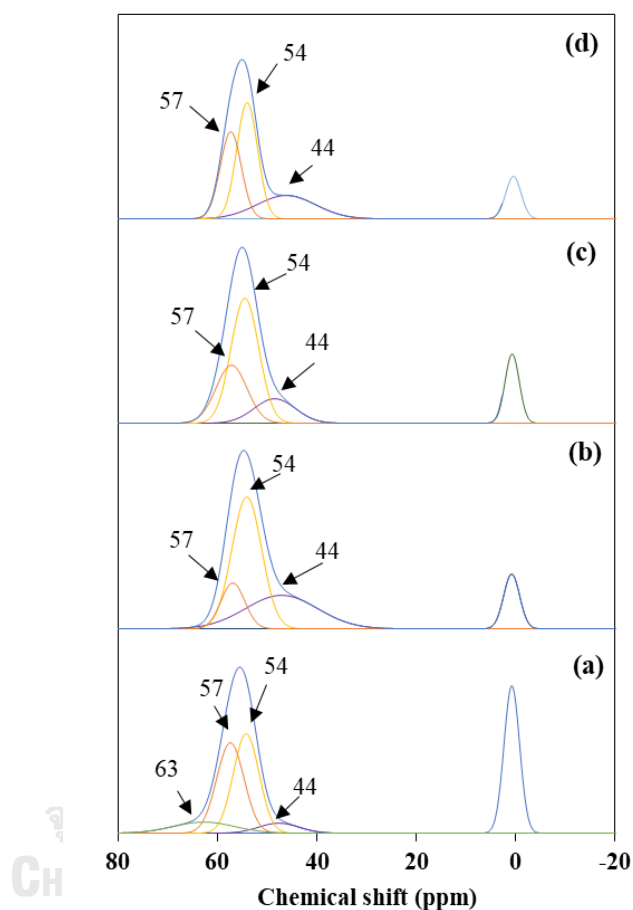


Fig. 4.3 ^{27}Al MAS NMR spectra of (a) beta, (b) beta-0.25M-deA, (c) beta-0.50M-deA, and (d) beta-0.75M-deA.

The %relative peak area for each signal was calculated and presented in Table 4.2. The parent beta zeolite was consisted of 71.4% tetrahedral Al framework with 28.7% octahedral one. After dealumination, the %relative area of total missing Al of samples increased to 3.70-27.2% with increasing the HF concentration in the HF/ HN_4F solution to 0.25-0.75 M. The deconvolution of ^{27}Al MAS NMR spectra

indicated that the extra-framework of Al species in the tetrahedral coordination at 63 ppm was totally eliminated. Moreover, the %relative area of octahedral Al species at 0 ppm and Al framework occupying T₃-T₉ at 57 ppm decreased from 28.7% to 7.50-11.5% and from 28.7 to 12.6-21.2%, respectively after dealumination using HF concentration in the range of 0.25-0.75M. However, the %relative area of extra-framework of Al in the distorted environment at 44 ppm and Al framework of T₁-T₂ sites at 54 ppm remarkably increased from 4.70% and 29.8% to 28.1 and 45.4% when the HF concentration in the HF/NH₄F solution was 0.25 M. This was due to the conversion of extra-framework octahedral Al species to the extra-framework tetrahedral Al species [53]. At the HF concentration higher than 0.25 M, the %relative peak area of both signals tended to be decreased. This was due to the reversible formation of the removed Al species to the zeolite framework resulting in the higher signal intensity at 57 ppm [53].

Table 4.2 Relative peak areas for each signal in ²⁷Al MAS NMR spectra of beta zeolite before and after dealumination

Supports	%Relative peak area (%) ^a					
	Extra-framework octahedral Al species at 0 ppm	Tetrahedral Al species at				Missing Al
		44 ppm (extra-framework)	54 ppm	57 ppm	63 ppm (extra-framework)	
beta	28.7	4.70	29.8	28.7	8.20	0.00
beta-0.25M-deA	10.1	28.1	45.4	12.6	0.00	3.70
beta-0.50M-deA	11.5	12.2	40.5	21.2	0.00	14.7
beta-0.75M-deA	7.50	16.1	28.0	21.2	0.00	27.2

^a Calculated by comparison of peak area of each signal to total integral peak area of untreated beta zeolite [52].

Fig. 4.4 and Table 4.3 summarized the acidity of the beta supports detect by NH₃-TPD analysis. The parent beta zeolite having Si/Al ratio of 14.4 had total acidity of 1,561 μmol NH₃/g with weak, medium and strong acid sites of 467, 676 and 418 μmol NH₃/g, respectively. After dealumination using 0.25 M HF/NH₄F solution, the Si/Al ratio of the beta-0.25M-deA increased to 15.5 with decreasing the total acidity to 1,290 μmol NH₃/g resulting from the reduction of all acidic sites. However, the

increase in the HF/NH₄F solution to 0.50-0.75 M increased the total acidity to 1,600-1,659 $\mu\text{mol NH}_3/\text{g}$ with increasing the amount of all acidic types. It was possible that the higher HF concentration in the presence of NH₄F provided the higher amount of highly electronegative fluoride ions subsequently incorporated in the zeolite lattice to increase the acidity of the treated zeolite [54].

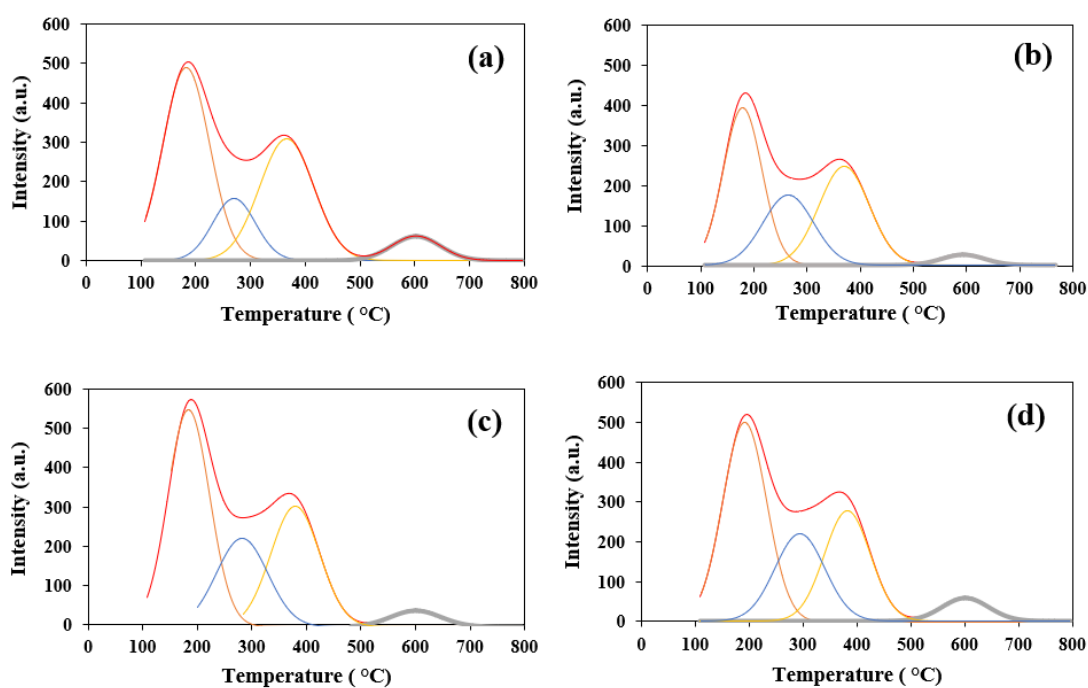


Fig. 4.4 NH₃-TPD profiles of (a) beta, (b) beta-0.25M-deA, (c) beta-0.50M-deA, and (d) beta-0.75M-deA.

The number of Lewis and Bronsted acid sites was also evaluated using pyridine-probed FTIR analysis. The infrared spectra of the pyridine adsorption of beta zeolite before and after dealumination shown in Fig. 4.5 exhibited the Bronsted and Lewis acid sites at 1,550 and 1,450 cm^{-1} , respectively. Not only increase in the Si/Al ratio, the higher HF concentration in the HF/NH₄F solution also increased the amount of Lewis acid site from 97 to 164-197 $\mu\text{mol py}/\text{g}$. This was due to the replacement of the aluminum-associated hydroxyl with fluoride as shown in Fig. 4.6 [55]. This result provided the enhancement of Lewis acid strength with lowering Bronsted acid sites/Lewis acid sites (B/L ratio). The amount of Lewis acid site of the zeolite seems

to be in line with the trend of Si/Al ratio. The higher Si/Al ratio indicated the higher content of the Lewis acid site [10]. When HF concentration in HF/NH₄F solution was increased the Bronsted acid sites increased from 147 $\mu\text{mol py/g}$ for using 0.25 M HF to 188-206 $\mu\text{mol py/g}$ for 0.50-0.75 M HF. The B/L ratio in the beta zeolite treated by HF/NH₄F solution was opposite to that was treated by citric acid and sulfuric acid [10]. The B/L ratio of the zeolites treated by citric or sulfuric acid was increased due to the proton transfer from the acids to the zeolite framework [10].

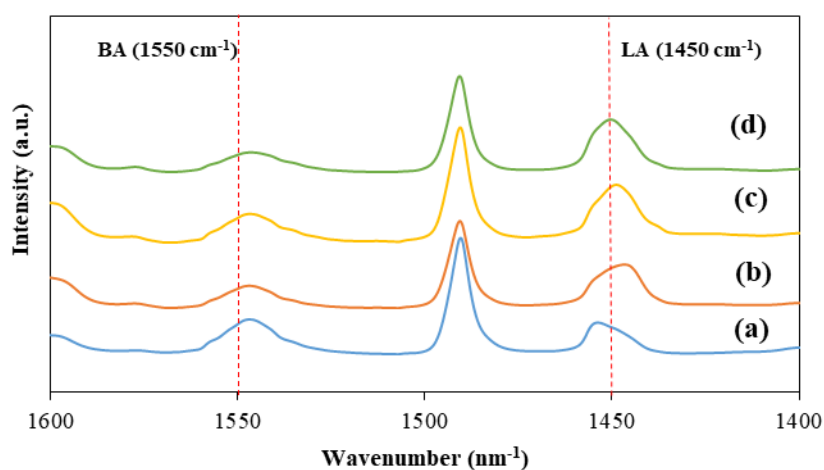


Fig. 4.5 Pyridine FTIR spectra of (a) beta, (b) beta-0.25M-deA, (c) beta-0.50M-deA, and (d) beta-0.75M-deA.

Table 4.3 Acidic properties of beta zeolite before and after dealumination

Supports	Si/Al atomic ratio ^a	NH ₃ -TPD ($\mu\text{mol NH}_3/\text{g}$)				Py-FTIR ($\mu\text{mol py/g}$)		
		Weak (< 200 °C)	Medium (200-350 °C)	Strong (350-600 °C)	Total acid	Lewis (L)	Bronsted (B)	B/L
beta	14.4	467	676	418	1,561	97.1	212	2.18
beta-0.25M-deA	15.5	399	568	323	1,290	164	147	0.89
beta-0.5M-deA	15.9	474	701	425	1,600	197	206	1.05
beta-0.75M-deA	16.1	494	695	470	1,659	194	188	0.96

^a Evaluated by % atomic from EDX.

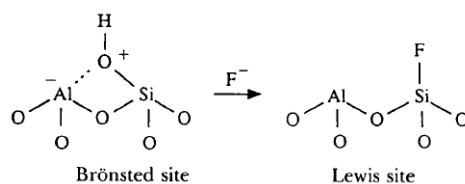


Fig. 4.6 Replacement of the aluminum associated hydroxyl with fluoride [55].

4.1.2 Characterization of Ni-based catalysts supported onto beta zeolite with and without dealumination

Fig. 4.7 shows the N_2 adsorption–desorption isotherms of Ni catalyst supported on beta zeolite with and without dealumination using HF/ NH_4F solution at different HF concentrations. All calcined catalysts exhibited types IV isotherm with H4 type loop that were also found with some mesoporous zeolites [56]. The isotherms showed a rapid aggrandizement in adsorption indicating that the mesopores were connected at the surface with intracrystalline micropores and caused the capillary condensation at P/P_0 in 0.95-1.00 range [57]. From the pore radius distribution, the Ni catalyst supported on unmodified beta zeolite had the board peak of pore radius distribution in the range of 20-60 Å. After dealumination with 0.25 M HF in the HF/ NH_4F solution, the high intensity of pore radius distribution was observed at 20-30 Å resulting in enhancement of the surface area from 149 m^2/g to 170 m^2/g for BET surface area (S_{BET}) and micropore surface area (S_{micro}), respectively as shown in Table 4.4. It was possible that the acid leaching was partial damaged of Al framework [57]. The increase in the HF concentration in the HF/ NH_4F solution from 0.50-0.75M remarkably decreased S_{BET} from 560 m^2/g to 513-540 m^2/g , while mesoporous volume (V_{BJH}) increased from 0.45 cm^3/g to 0.52-0.56 cm^3/g . This was possible that increased HF concentration increased mesoporous structure formation [58].

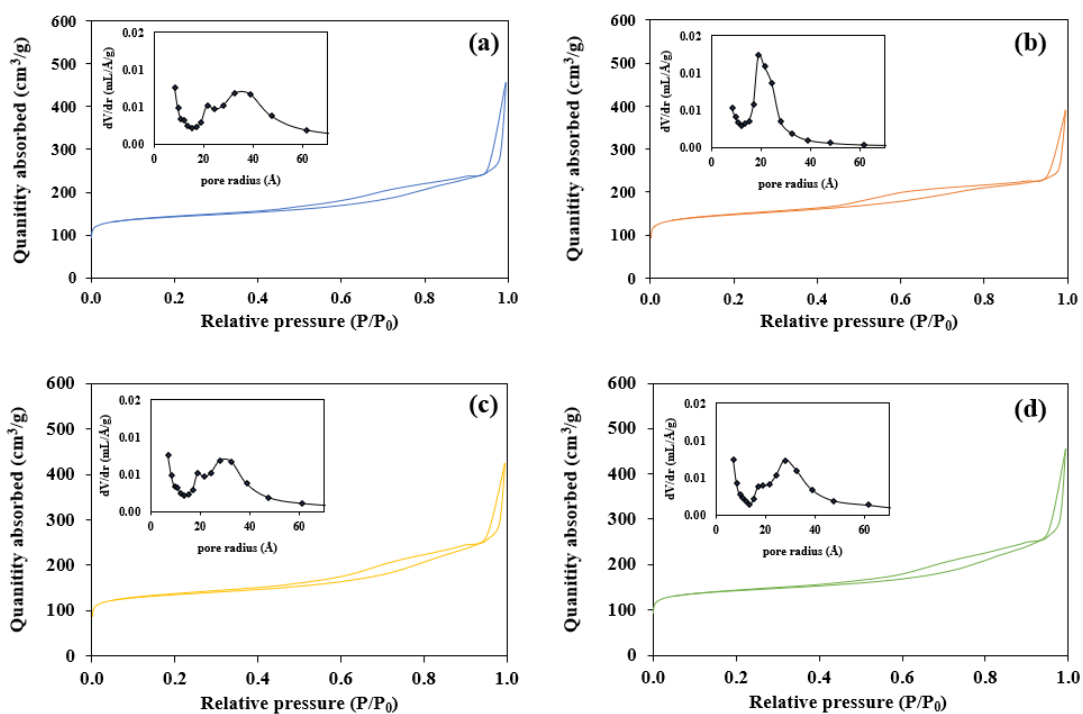


Fig. 4.7 N_2 adsorption-desorption isotherm and pore size distribution of (a) Ni/beta, (b) Ni/beta-0.25M-deA, (c) Ni/beta-0.5M-deA, and (d) Ni/beta-0.75M-deA catalysts.

Table 4.4 Textural properties of Ni supported beta zeolites before and after dealumination

Catalysts	Surface area(m ² /g)			Pore volume (cm ³ /g)			Pore radius (Å)	
	S ^a _{BET}	S ^b _{micro}	S ^c _{external}	V ^d _{micro}	V ^e _{BJH}	V ^f _{total}	R ^g _{avg}	R ^h _{BJH}
Ni/beta	540	149	391	0.15	0.56	0.71	26.2	3.01
Ni/beta-0.25M-deA	560	170	390	0.15	0.45	0.6	21.5	3.00
Ni/beta-0.5M-deA	513	154	359	0.14	0.52	0.66	25.5	3.00
Ni/beta-0.75M-deA	540	147	393	0.15	0.56	0.71	26.1	3.00

^a MultiPoint BET method

^b t-method micropore surface area

^c t-method external surface area

^d Micropore volume was obtained using t-plot method.

^e Mesopore volume was obtained from BJH method cumulative desorption

^f Total pore volume for pores with Radius less than 1755.00 Å at P/P₀ = 0.994517

^g Average pore radius

^h Pore radius was obtained from BJH method.

Fig. 4.8 showed TEM images of the NiO particles supported on beta zeolite with and without dealumination. The histograms of particle size distributions were inserted in their corresponding TEM images and NiO particles size. The particle size distribution of Ni/beta showed NiO particle size at 22.8 nm in Fig. 4.8a. The NiO particle size of Ni/beta-0.25M-deA were decreased to 13.8 nm as shown in Fig. 4.8b. To comparing XRD patterns, the NiO particle size of Ni/beta-0.25M-deA reduced from 22.3 nm (Ni/beta) to 12.7 nm that wasn't different from TEM images. This was possibly that dealumination increased Ni dispersion. The presence of stronger interaction between nickel oxide and dealuminated beta zeolite to reduce NiO particle size [59].

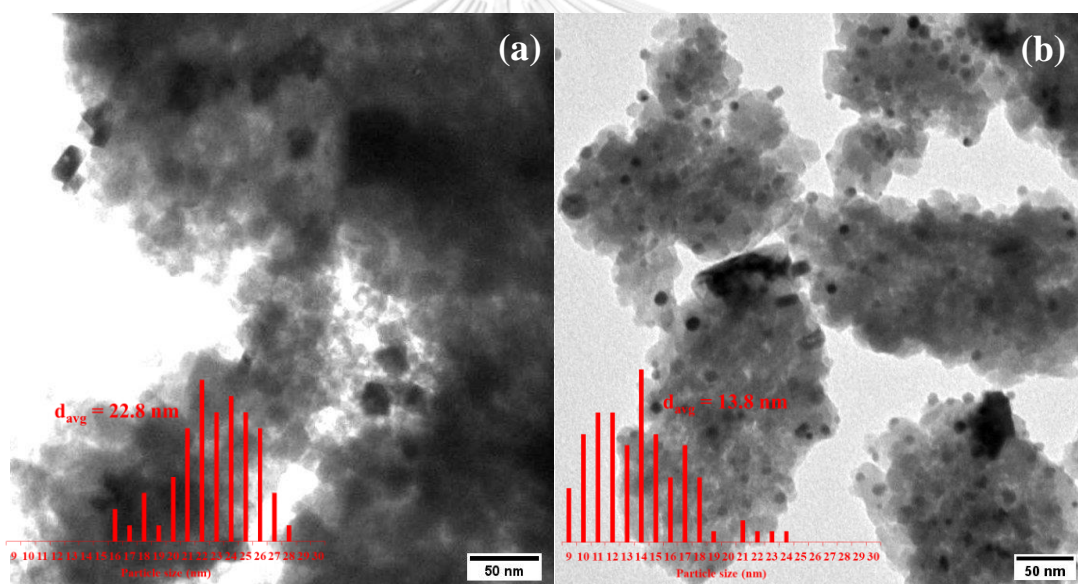


Fig. 4.8 TEM images and distribution of the size of nickel crystallites on the surface of (a) Ni/beta and (b) Ni/beta-0.25M-deA catalysts.

The X-ray diffraction patterns (Fig. 4.9) show an incorporation of Ni onto dealuminated beta zeolite. The results indicated that the signals were observed at 2θ of 37.2° , 43.2° , 62.8° , 75.3° , and 79.4° , which were attributed to the nickel oxide (NiO) phase [60]. The XRD technique was also used to estimate the NiO crystallite size by Scherrer equation [42]. From Table 4.5, the NiO crystallite size on the dealuminated zeolites was in the range of 12.7-13.8 nm, which was smaller than one

supported on the unmodified zeolite (22.3 nm). This implied that the interaction between Ni particles and surface of dealuminated zeolite was stronger. The result was also confirmed by using H₂-TPR technique as shown in Fig. 4.9. This was possible that the interaction between Ni particles and surface of dealuminated zeolite was stronger resulting in the higher degree of Ni dispersion from 1.67% to 4.43-5.22%.

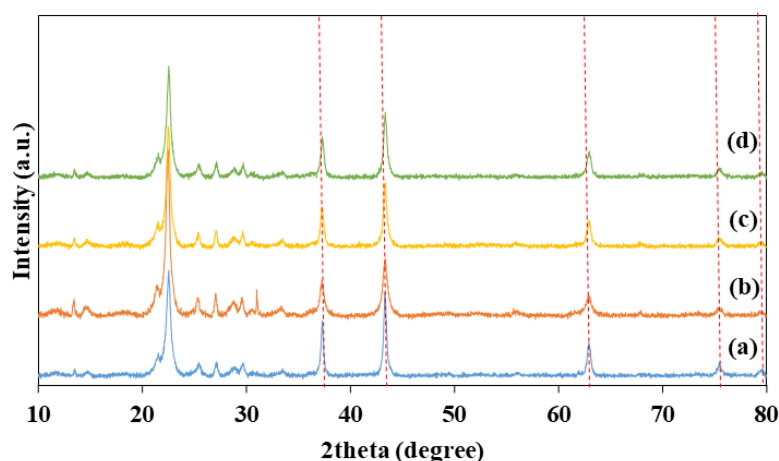


Fig. 4.9 XRD patterns of (a) Ni/beta, (b) Ni/beta-0.25M-deA, (c) Ni/beta-0.5M-deA, and (d) Ni/beta-0.75M-deA catalysts.

Since the size of the NiO particles and reducibility of the catalyst strongly affect the catalytic activity, the reduction ability of Ni containing beta zeolite catalyst was characterized by hydrogen temperature programmed reduction (H₂-TPR) and corresponding profiles are shown in Fig. 4.10. It exhibited that the reduction temperature of Ni catalysts supported on dealuminated zeolite was shifted to the higher temperature from 560 °C (Ni/beta catalyst) to 660 °C (Ni/beta-0.25M-deA catalyst). The reduction temperature at 600 °C might be the reduction of nickel aluminate (NiAl₂O₄) or nickel silicate (Ni₂SiO₄) specie [59, 61]. For the use of the higher HF concentration (0.50-0.75 M), the higher reduction temperature which was 660 °C on Ni/beta-0.25M-deA catalyst shifted to lower temperature (580-600 °C) as shown in Fig. 4.9. This was possibly due to the lower Ni metal dispersion in the cationic positions of BEA and the formation of larger nickel oxide clusters as seen in Table

4.5. This was consistent with the significant decrease in the Al content in the beta zeolite following the acid treatment [62]. Although, the Ni/dealuminated zeolite catalyst showed the higher reduction temperature reflecting the higher metal support interaction than one supported on the parent zeolite, they had higher reducibility ca. 92-95%, while the Ni/beta catalyst had 88.6% reducibility. This was related to the degree of Ni dispersion. This result was consistent with the previous literature [62].

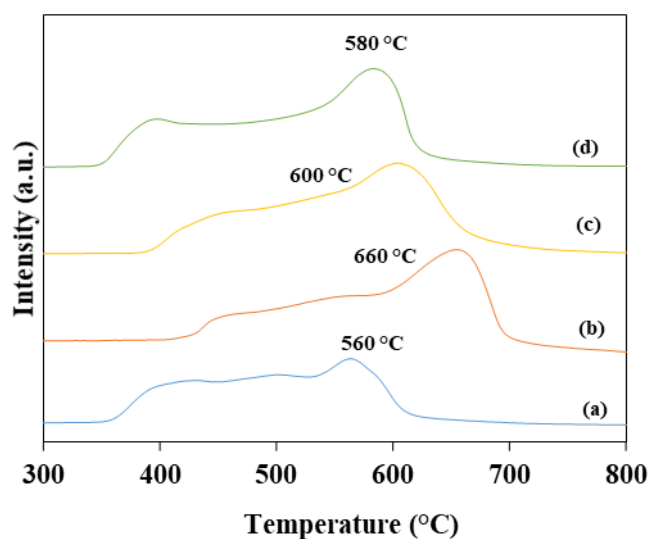


Fig. 4.10 H₂ TPR profiles of (a) Ni/beta, (b) Ni/beta-0.25M-deA, (c) Ni/beta-0.50M-deA, and (d) Ni/beta-0.75M-deA catalysts.

Table 4.5 Actual Ni content, NiO crystalline size, Ni dispersion, H₂ consumption and reducibility Ni-based catalysts.

Catalysts	Actual Ni content ^a	NiO crystalline size (nm) ^b	Ni dispersion ^c (%)	H ₂ consumption ^d (mmol/g)	Reducibility ^e (%)
Ni/beta	9.5	22.3	1.67	2.37	88.6
Ni/beta-0.25M-deA	8.2	12.7	5.22	2.86	95.1
Ni/beta-0.5M-deA	8.7	13.6	5.10	2.56	93.5
Ni/beta-0.75M-deA	9.2	13.8	4.43	2.43	91.9

^a %wt of Ni loading on zeolite was measured by ICP OES.

^b NiO crystalline size was measured from XRD.

^c %Ni dispersion was measured from CO-pulse method.

^d H₂ consumption of Ni zeolite catalysts was measured from H₂ TPR profiles.

^e Evaluated by comparing the total H₂ consumption obtained from the H₂-TPR technique and the theoretical value calculated from the reduction of all metal oxides.

4.1.3 Hydroisomerization of palm olein over Ni/dealuminated beta zeolite catalysts

Palm olein is triglyceride which can be transformed to liquid bio-fuels consisting of n-alkanes, iso-alkanes, cyclo-alkanes and aromatic compounds by hydrotreating process [63]. The conversion of triglyceride via hydrotreatment involves with complex reaction pathways such as hydrocracking, hydrodecarboxylation, hydrodecarbonylation, hydrodeoxygenation, and hydroisomerization [64]. Therefore, it is important to find the appropriate catalyst for the selective production of fuel-range hydrocarbons [64]. For hydroisomerization, the increase in the Si/Al ratio can enhance catalytic activity to convert n-alkanes to iso-alkanes [39]. During the bio-jet fuel production from hydrotreating process of palm oil, the iso/n-paraffins ratio was monitored to keep high iso-alkanes content [65]. In order to maximize the yield of bio-jet containing a high iso-alkanes fraction, the effects of initial hydrogen (H₂) pressure and reaction temperature on the product yields, chemical composition and carbon number distribution in the liquid product were observed for hydroisomerization of palm olein over nickel (Ni) supported on dealuminated beta zeolite using different HF concentrations in the HF/NH₄F solution.

4.1.3.1 Effect of initial H₂ pressure on hydroisomerization of palm olein over Ni/dealuminated zeolites

The effects of initial H₂ pressure on the product yields (liquid, gas, and solid products), chemical compositions (n-alkanes, iso-alkanes, cyclics, aromatics, oxygenated and unsaturated species) and carbon number distribution in the liquid product obtained from hydroisomerization of palm olein over Ni catalyst supported on beta zeolites with and without modified by dealumination using HF/NH₄F solution with various HF concentrations were shown in Fig. 4.10-4.13.

The reaction temperature and time were kept constant at 340 °C for 5 h. To consider the product yields (Fig. 4.11), the hydrotreating operated under 30 bar initial H₂ pressure gave insignificant difference of the liquid yield (82-85 wt%) obtained from the Ni-based catalysts supported on beta zeolite with or without acid leaching. However, the increasing initial H₂ pressure to 40-50 bar remarkably decreased the liquid product to 69-75 wt%. This was possible that the high H₂ pressure promote the hydrogenolysis to induce the C-C cleavage of triglyceride [19]. Moreover, the liquid product obtained from the system using the Ni catalyst supported on the dealuminated beta zeolite was more decreased with higher HF concentration in the HF/NH₄F solution for the acid leaching. This could be explained from two reasons: (1) the larger pore size of the dealuminated beta zeolite could induce the central cracking more than the terminal cracking of alkanes compounds like catalytic cracking of H-ZSM-5 zeolites to obtained more gaseous product [33] and (2) The excessive Bronsted acid sites might promote, the secondary cracking, resulting in the higher amount of light compounds such as C1-C4 gas product and gasoline (C5-C8) [16].

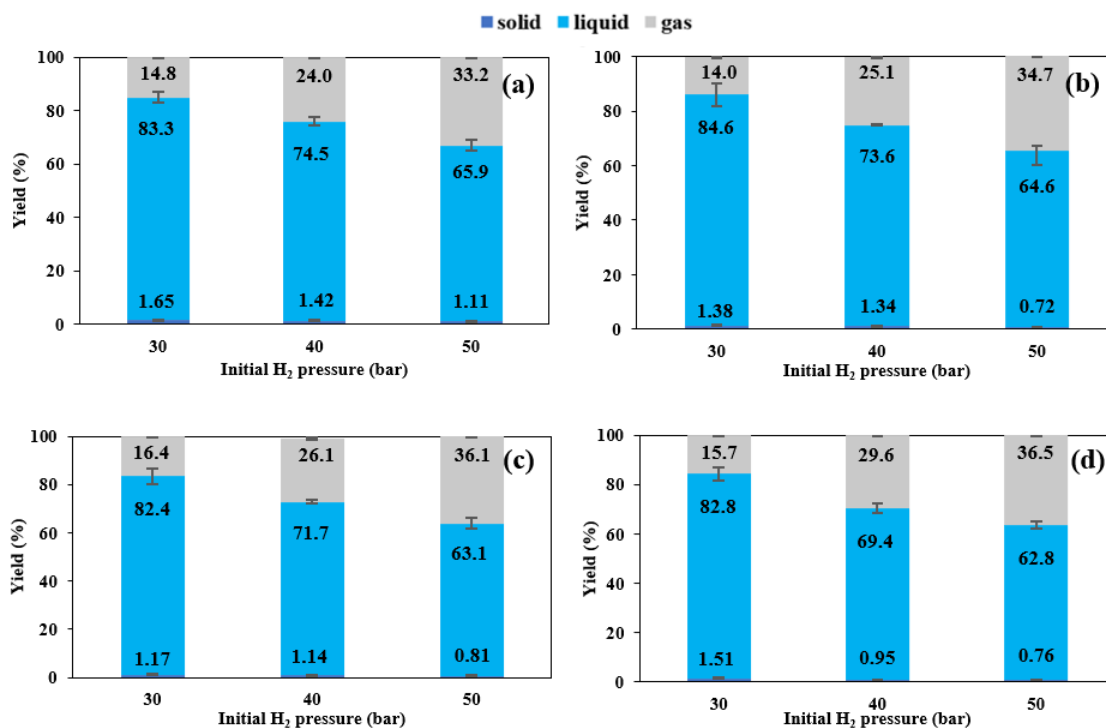


Fig. 4.11 Product distribution obtained from hydroisomerization of palm olein under various initial H₂ pressure over (a) Ni/beta, (b) Ni/beta-0.25M-deA, (c) Ni/beta-0.50M-deA, and (d) Ni/beta-0.75M-deA catalysts at 340 °C for 5 h.

The hydrocarbon types in the liquid product derived from the hydroisomerization of palm olein were identified by GCMS analysis and divided as three types following the number of carbon atoms: bio-gasoline (C8), bio-jet fuel (C9-C14) and green diesel (C15-C18) [6]. Moreover, the GCMS chromatograms also provided the chemical compositions in the liquid products in terms of n-alkanes, iso-alkanes, aromatics, cyclics, oxygenated compounds, and unsaturated compounds and compared to the commercial Jet A-1. From Fig. 4.12a, Jet A-1 was consisted of hydrocarbons in the range of C9-C21. It was observed that the Jet A-1 had the large number of small signals between the peaks of alkanes in the range n-C9 to n-C12. These signals are attributed to the iso- or branch- structure.

To consider the GC-MS chromatograms of the liquid biofuels obtained from hydroisomerization of palm olein, Fig. 4.12b-4.12e showed that the GC-MS chromatograms of the liquid biofuels obtained from the system using Ni supported

on beta zeolite with and without dealumination under 30 bar initial H₂ pressure at 340 °C were similar. They normally contained n-alkanes in the range of n-C15 to n-C18. When the initial H₂ pressure increased to 40 bar, the system using Ni/beta-0.25M-deA catalyst provided the liquid biofuels contained the smaller molecules (n-C10). Whereas, the liquid biofuels generated from the other catalyst were consisted of the larger molecules (n-C15 and n-C17). This was possibly due to the higher surface area with the highest level of Ni dispersion of Ni/beta-0.25M-deA to facilitate the cracking reaction. Moreover, the lowest B/L acid ratio (0.89) of the Ni/beta-0.25M-deA could promote the cracking of alkanes [12]. However, the higher B/L acid ratio of the dealuminated beta zeolites obtained from HF concentrations above 0.25 M decreased the ability for cracking. The increase in the initial H₂ pressure to 50 bar could effectively decrease the amount of the large molecules. It was noticed that the GC-MS chromatogram of the liquid obtained from the system using Ni/beta catalyst showed high intensity of n-C10 (Fig. 4.12b), while the use of Ni/dealuminated zeolite catalyst decreased the intensity of the n-alkanes by converting to the branch structure (Fig. 4.12c-4.12e).

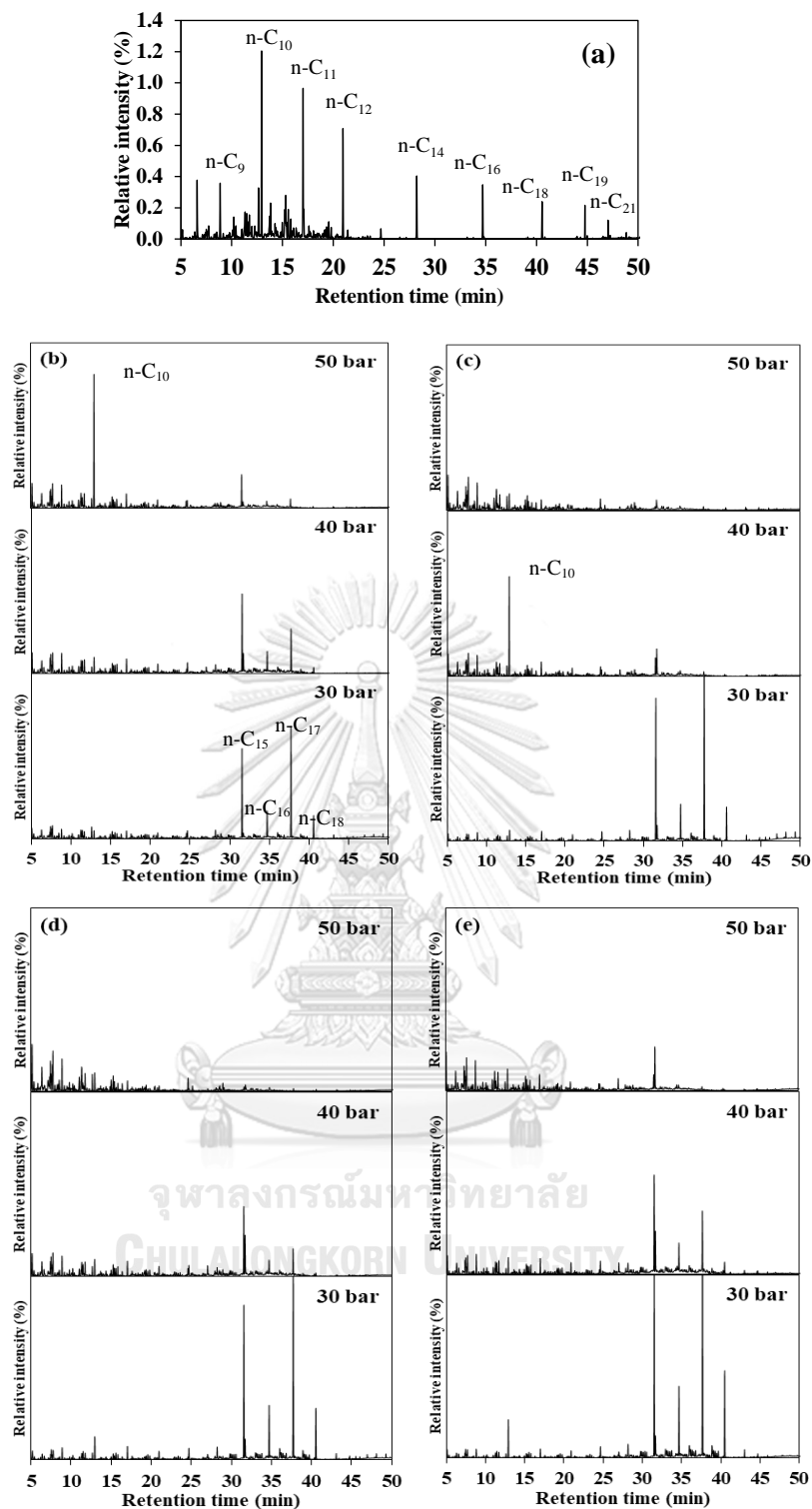


Fig. 4.12 GCMS chromatograms of (a) jet A-1 and liquid product obtained from hydroisomerization of palm olein over (b) Ni/beta, (c) Ni/beta-0.25M-deA, (d) Ni/beta-0.50M-deA and (e) Ni/beta-0.75M-deA catalysts under 30-50 bar initial H₂ pressure at 340 °C for 5 h

The detail in GCMS chromatograms in Fig. 4.12 was classified as the selectivity to n-alkanes, iso-alkanes, aromatics, cyclics, oxygenated compounds and unsaturated species by using the peak area as shown in Fig. 4.13. The result indicated that the liquid product obtained from Ni/beta catalyst was consisted of 53.0% n-alkanes, 27.2% iso-alkanes, 7.90% aromatics, 2.56% cyclics, 8.52% oxygenated compounds and 1.23% unsaturated species when the reaction was operated under 30 bar initial H₂ pressure (Fig. 4.13a). The increase in the initial H₂ pressure to 40-50 bar promoted the hydroisomerization to increase the iso-alkanes selectivity to 34.3-40.9% (Fig. 4.13b-4.13c). However, it was found that the aromatization was induced under high H₂ pressure to obtain the aromatics content to 26.0%. Moreover, some aromatics were simultaneously hydrogenated resulting in the higher amount of the cyclic compounds (13.4%). This indicated that the higher H₂ pressure promoted hydroisomerization, aromatization and hydrogenation. However, the unsaturated compounds and oxygenated species could be easily to be removed at low initial H₂ pressure.

To consider the liquid product obtained from the system using Ni/dealuminated beta zeolite catalysts at 30 bar initial H₂ pressure (Fig. 4.13a), the use of Ni/beta-0.25M-deA catalyst provided the liquid biofuel increased iso-alkanes from 27.2% (Ni/beta) to 35.4%. It was explained that isomerization converted alkanes on the metal via dehydrogenation to alkenes which were protonated to form carbenium ions and then transformed to mono- and multi-branch carbenium ions via β -scission. After that, the iso-intermediate were hydrogenated to form isomers. Thus, the high metal-acid balance of Ni metal indicating by the well dispersion on surface were led alkene intermediate to hydrogenate the high isomer formation [66]. However, the system using Ni/beta-0.50M-deA and Ni/beta-0.750M-deA catalysts provided the higher n-alkane fraction with decreasing the formation of iso-alkanes

and aromatics. This was indicated that the lower Ni dispersion decreased iso-alkanes content as shown in Fig. 4.13a.

When increased initial H₂ pressure to 40-50 bar, Ni/dealuminated beta zeolite gave the liquid biofuel contained higher iso-alkanes selectivity (43.3-47.3%) than Ni/beta (34.3-40.9%). It could be explained that dealumination by using HF/NH₄F solution could increase the interaction between Ni metal and zeolite support to give higher Ni dispersion than loading on parent beta zeolite. The high Ni dispersion was introduced smaller Ni particles that contributed a closer intimacy between Ni metal sites and acid sites to reduce the number of acid steps the alkene intermediates undergo during diffusion for improving hydroisomerization [66]. Although, the increasing initial H₂ pressure increased iso-alkane content, it also increased aromatic content related pressure. It was possible that the use of high H₂ pressure would drive the equilibrium toward hydrogenation as supported by the higher formation level of cyclic compounds from 1.45% to 13.8 wt% via hydrogenation of some portion of aromatic substances to promote alkene aromatization [19, 67].



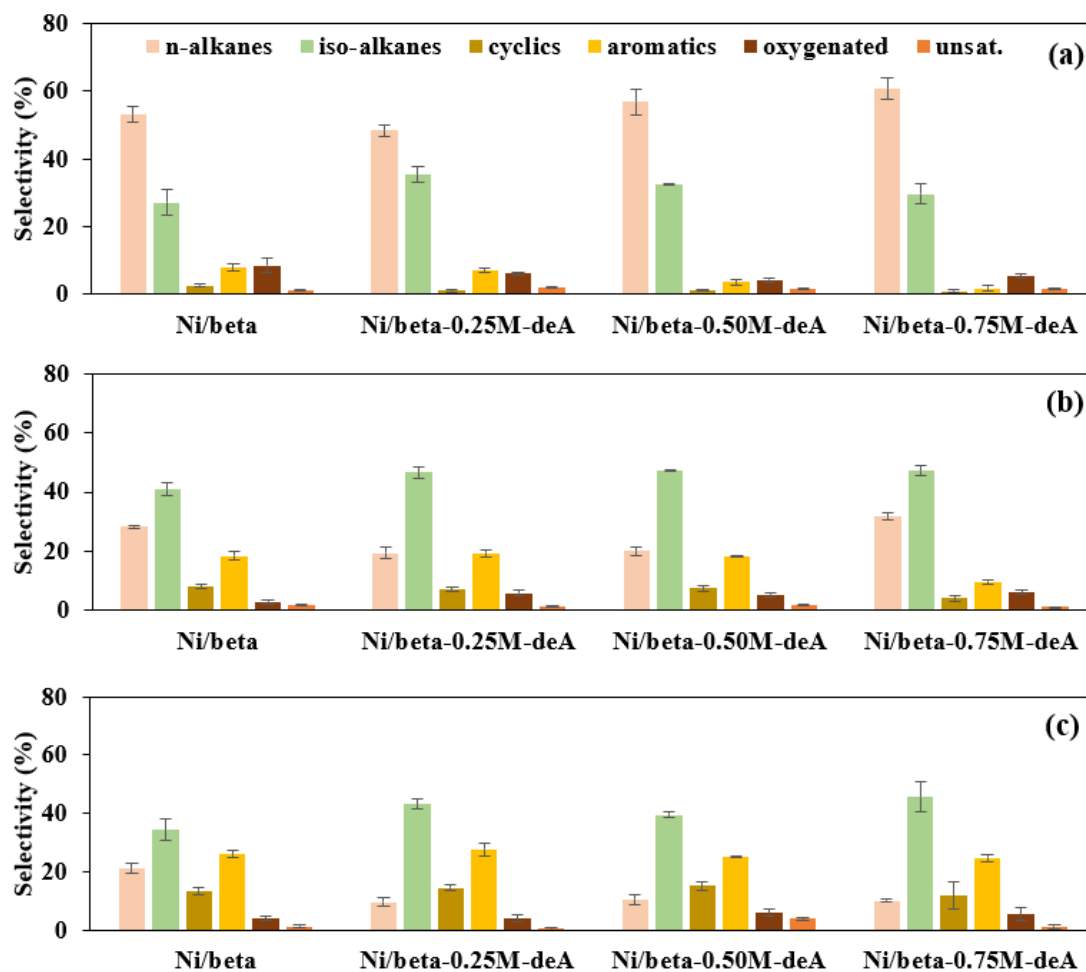


Fig. 4.13 Selectivity to chemical compositions in the liquid product obtained from the hydroisomerization of palm olein catalyzed by Ni-based catalysts under (a) 30 bar, (b) 40 bar and (c) 50 bar initial H_2 pressure at $340^\circ C$ for 5 h.

The hydrocarbon types in the obtained liquid product were also classified as bio-gasoline (<C8), bio-jet fuel (C9-C14) and green diesel (C15-C18) following the carbon number of n-alkanes and iso-alkanes as shown in Fig. 4.14. For hydroisomerization of palm olein over Ni/beta catalyst under 30 bar initial H_2 pressure, Fig. 4.14(a-1) indicated that the liquid product contained 4.58% bio-gasoline, 21.6% bio-jet fuel and 52.4% green diesel with iso/normal alkane ratio at 0.47. When initial H_2 pressure increased to 50 bar, bio-gasoline and bio-jet fuel fractions increased to 12.6% and 39.2%, respectively with decreasing the green diesel to 22.5% as shown in Fig 4.14(a-3). Moreover, the iso/normal alkane ratio increased

to 1.67. This indicated that the increases in the H₂ pressure could promote hydrogenolysis of long chain hydrocarbons to give more gasoline and jet fuel fractions [68].

In the case of hydroisomerization of palm olein over Ni/dealuminated beta zeolite catalysts under 30 bar initial H₂ pressure, the use of Ni/beta-0.25M-deA catalyst provided the liquid biofuels having the highest content of bio-jet fuel range (30.3%) with the highest iso/normal alkane ratio at 0.64. This indicated that high Ni dispersion led Alkane isomerization to increase iso-alkane content [66]. When initial H₂ pressure increased to 40-50 bar, the liquid products had higher bio-gasoline fraction than the use of Ni/beta catalyst at the same initial H₂ pressure. The increase of H₂ pressure led to reduced selectivity to green diesel from 52.4% (Ni/beta at 30bar) to 0.77% (Ni/beta-0.25M-deA at 50bar) and increased iso/normal alkanes from 0.47 to 4.00. This behavior could be explained by considering the bifunctional mechanism. At high hydrogen pressure, the iso-carbenium ion could be rapidly hydrogenated to iso-alkanes on the metal sites, which could be due to a shorter residence time for rearrangement to give high iso-alkane content [16]. However, the increased HF concentration in the HF/NH₄F solution to 0.50-0.75 M trended to decreased iso/normal alkane ratio due to the lower Ni dispersion to reduce the alkene isomerization activity [66].

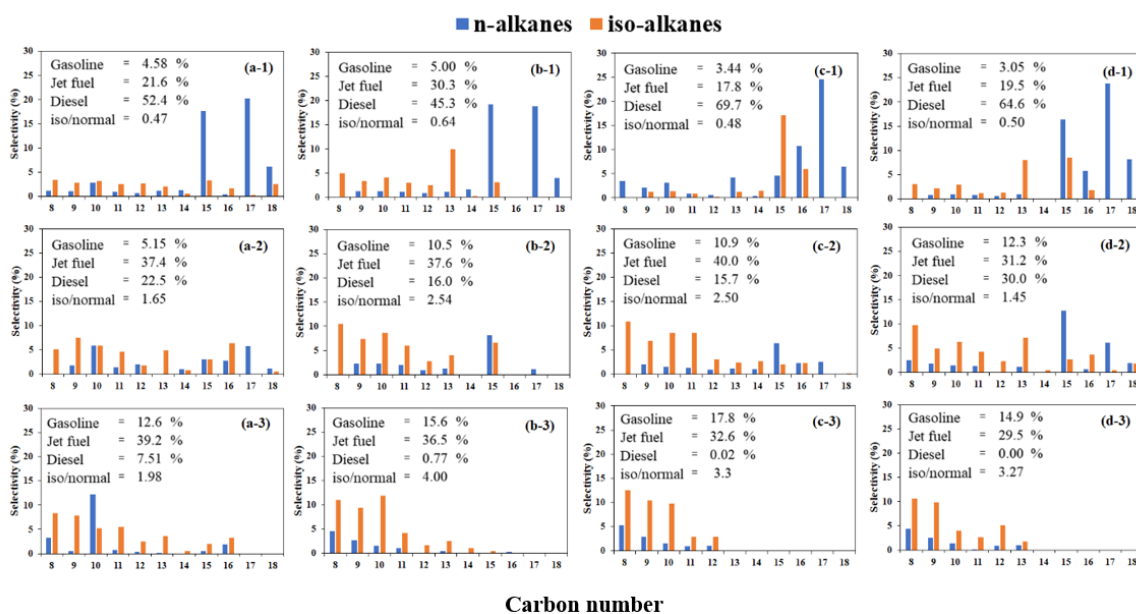


Fig. 4.14 Carbon distribution in the liquid product obtained from the hydroisomerization of palm olein at 340 °C for 5 h over (a) Ni/beta, (b) Ni/beta-0.25M-deA, (c) Ni/beta-0.5M-deA, and (d) Ni/beta-0.75M-deA under initial H₂ pressure of (1) 30 bar, (2) 40 bar and (3) 50 bar.

4.1.3.2 Effect of dealumination and reaction temperature on product distribution and chemical compositions of liquid product.

In this section, the univariate analysis with the central condition of 40 bar initial H₂ pressure at 340 °C for 5 h was applied to study the effect of the reaction temperature on the product yields, chemical compositions, and the degree of iso/normal alkane ratio in the liquid biofuels obtained from the hydroconversion of palm olein using Ni catalysts supported on the beta zeolite with and without dealumination using HF/NH₄F solution containing various HF concentrations as shown in Fig. 4.14-4.16.

To consider the product yields, Fig. 4.15a indicated that the liquid biofuels was ca. 73-74 wt% with 24-25 wt% gas product when the reaction catalyzed by Ni/beta was operated at 320-340 °C. Above this point (360 °C), the obtained liquid

yield was lower to 71 wt% with the higher content of gaseous product (ca. 28 wt%) since the higher reaction temperature promoted the severe cracking to more generate gaseous product [69]. However, it was observed that the yield of liquid product obtained from the system using Ni/dealuminated zeolite catalysts provided the higher liquid biofuels in the range of 79-84 wt% when the reaction temperature was 320 °C. This could be explained that dealuminated beta zeolite slightly decreased Bronsted acid site to decrease cracking resulting in increasing liquid product yield [16]. When the reaction temperature increased to 360 °C, the liquid product yields obtained from the process using all catalysts tended to be decreased to 65-71 wt%. However, the system using Ni/dealuminated beta zeolite catalysts showed the higher reduction of liquid product yields (13-23% reduction) than the Ni/beta catalyst (3.67% reduction). Especially, the hydroisomerization over Ni/beta-0.25M-deA catalyst provided the highest reduction of liquid biofuel (22.8%). This was possible due to the highest Ni-dispersion, which could promote the methanation to produce more gaseous product at elevated temperature [70, 71].

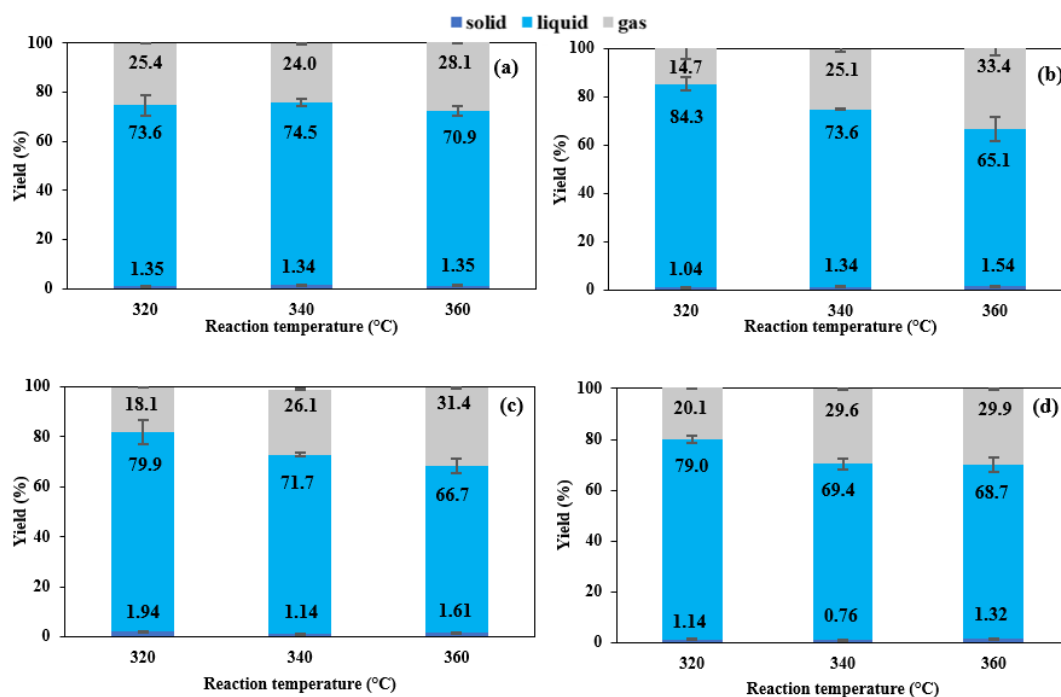


Fig. 4.15 Product yields obtained from hydroisomerization of palm olein over (a) Ni/beta, (b) Ni/beta-0.25M-deA, (c) Ni/beta-0.5M-deA, and (d) Ni/beta-0.75M-deA under 40 bar initial H_2 pressure at 320-360 °C for 5 h.

To consider the components in the liquid biofuels, Fig. 4.16a indicated that the hydroisomerization of palm olein using Ni/beta catalyst under 40 bar initial H_2 pressure at 320 °C for 5 h provided the liquid product mainly consisting of 64.4% selectivity to n-alkanes with 22.3% selectivity to iso-alkanes. Moreover, the small amounts of oxygenated compounds (2.15% selectivity) and unsaturated species (0.80% selectivity) were observed indicating that hydrodeoxygenation and hydrogenation were simultaneously occurred during hydroisomerization. At this condition, the system catalyzed by Ni/beta-0.25M-deA could provide the liquid product with higher iso-alkanes to 36.9% selectivity possibly due to the highest Ni dispersion to promote hydrogenation/dehydrogenation to produce alkenes which were protonated to form carbenium ions, intermediates iso-alkane production [66]. However, the increased in the HF concentration in HF/ NH_4F solution to 0.50 and 0.75M could not promote hydroisomerization because of the lower level of Ni dispersion [16, 72].

When reaction temperature increased to 340 °C the selectivity to n-alkanes in the liquid product obtained from all studied catalyst decreased with increasing the selectivity to iso-alkanes (46.6-47.3%) as seen in Fig. 4.16b. This was due to the lower temperature provided unreactive alkane or wax product [65]. Moreover, the higher reaction temperature promoted the aromatization to increase the selectivity to aromatics [47, 73]. However, the opposite result was observed for the system using Ni/beta-0.75M-deA catalyst. Although, the fraction of iso-structure product increased, the selectivity to n-alkanes was also increased to 31.7% with lowering the aromatics selectivity (9.70%). This was possibly due to its highest total acidity to promote the selectivity for providing β -scission of carbonium to decreased aromatics content [25]. The reaction temperature at 360 °C (Fig. 4.15c), the selectivity to iso-alkanes obtained from all catalysts trended to be decreased with remarkably increasing the selectivity to aromatics. However, the fraction of aromatics in the liquid product obtained from the system catalyzed by Ni/dealuminated beta zeolite catalyst was lower than that from the Ni/beta one. This indicated that the dealumination could suppress the aromatic formation probably due to the lowering B/L acid ratio and the enhancement of mass transfer by the mesopores. These results further indicated the importance of the B/L ratio for aromatization in hydroconversion of triglycerides [74].

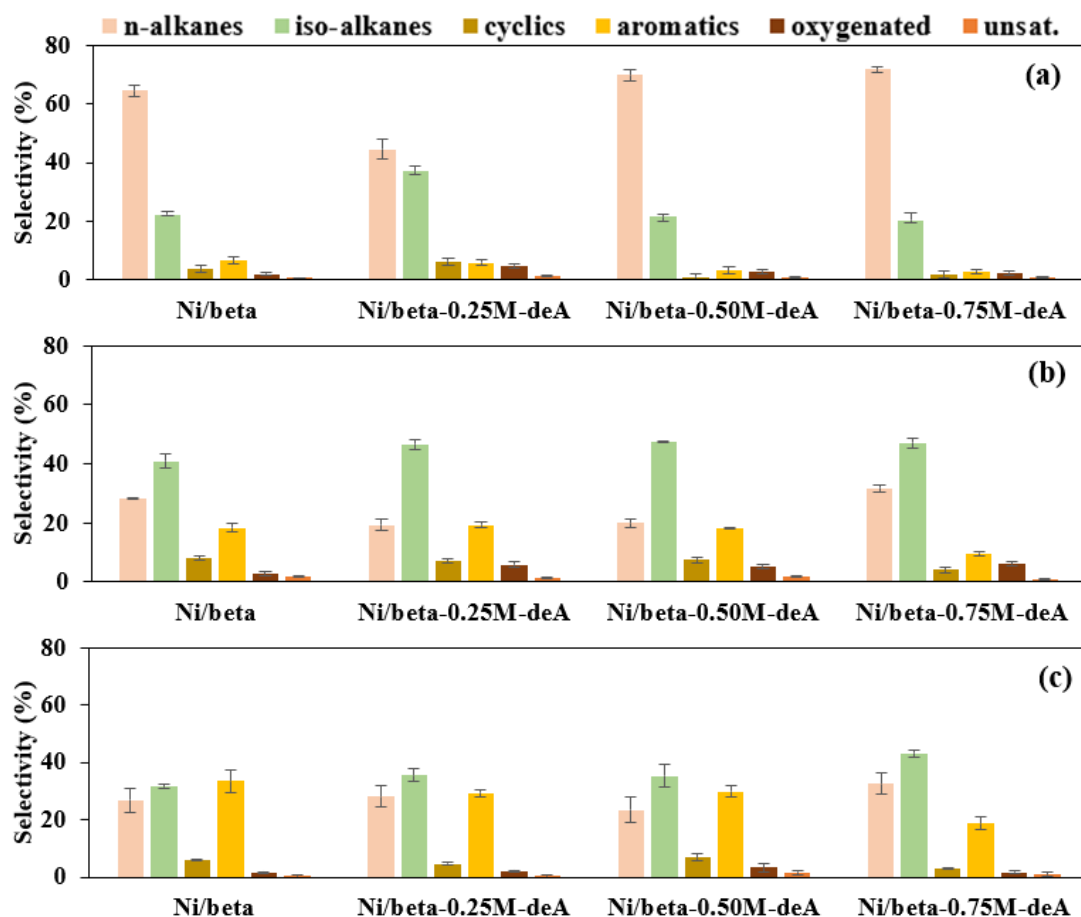


Fig. 4.16 %Selectivity to each composition in the liquid product obtained from the hydroisomerization of olein catalyzed by Ni-based catalysts under 40 bar initial H₂ pressure at (a) 320, (b) 340 and (c) 360 °C for 5 h.

Fig. 4.17 showed the distribution of carbon number of n-alkanes and iso-alkanes in the liquid product obtained from hydroisomerization of olein under 40 bar initial H₂ pressure at 320-360 °C for 5 h. The hydrocarbon types in the liquid product were also classified as bio-gasoline, bio-jet fuel and green diesel range following the number of carbons in the normal or iso alkanes molecules following C₈, C₉-C₁₄ and C₁₅-C₁₈, respectively. For the use of Ni/beta catalyst at 320 °C, the liquid product had C₁₅-C₁₈ as the main component resulting in the high green diesel fraction at 63.2% with 18.8% bio-jet fuel and 3.50% bio-gasoline. The iso/normal alkane ratio of the obtained liquid biofuel was only 0.30.

When the system used Ni/dealuminated beta zeolite as the catalyst for hydroisomerization at the same condition, the use of Ni/beta-0.25M-deA catalyst had ability to decrease the amount of long-chain hydrocarbons to obtain the liquid product containing n-C10 as the main component with the higher content of iso-structure in the range i-C8-i-C16 (Fig. 4.17(b-1)). This condition provided the higher amount of jet fuel range fraction to 48.8% with higher iso/normal alkanes ratio at 0.77. This was due to the higher Lewis acid site from Ni metal sites could promote alkene isomerization [66, 75]. However, the liquid product obtained from the system using Ni/beta-0.50M-deA and Ni/beta-0.75M-deA catalysts had the higher content of n-C15 to n-C18 again (Fig. 4.17(c-1) - 4.17(d-1)). This resulted from the decreasing Ni dispersion and H₂ consumption to affect hydroisomerization and hydrocracking. When the reaction temperature increased to 340-360 °C, the amount of iso-alkanes in the liquid product generated from all catalyst increased resulting in the higher iso/normal alkane ratio of 1.20-2.54 as shown in Fig. 4.17(a-2)-4.17(d-3). In this case, the system using Ni/beta-0.25M-deA and Ni/beta-0.50M-deA catalysts gave the highest iso/normal alkane ratio at 2.50-2.54% with 37.6-40.6% bio-jet fuel fraction (Fig. 4.17(b-2)-4.17(c-2)). However, the use of Ni/beta-0.75M-deA catalyst at 340-360 °C produced the liquid biofuel containing lower jet fuel fraction (31-33%) with low iso/normal alkane ratio in the range of 1.21-1.45. This could be explained that lower Ni dispersion resulting to suppress the hydrocracking [16, 72].

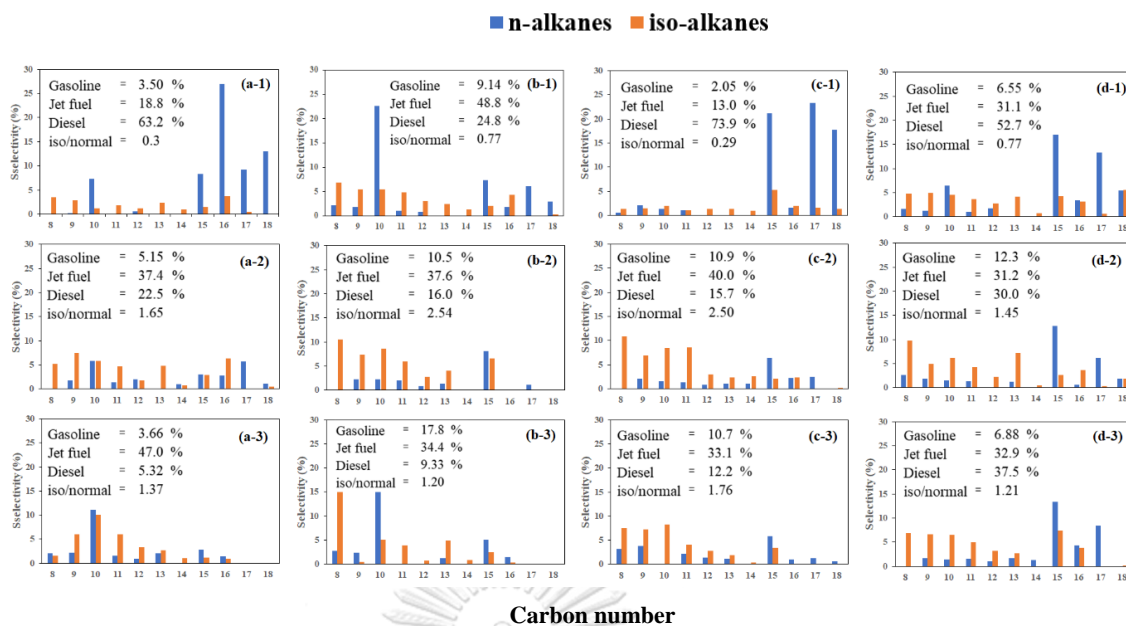


Fig. 4.17 Distribution of carbon number in the liquid product obtained from the hydroisomerization of palm olein over (a) beta, (b) beta-0.25M-deA, (c) beta-0.50M-deA, and (d) beta-0.75M-deA catalysts under 40 bar initial H₂ pressure at (1) 320, (2) 340 and (3) 360 °C.

4.2 The effect of desilication on hydroisomerization of palm olein

4.2.1 Catalyst characterization

Fig. 4.18 shows the N₂ adsorption–desorption isotherms for the beta zeolite before and after desilication using NaOH solution at different concentrations. All samples exhibited a high N₂ uptake (125-150 cm³/g) at low relative pressure ($P/P_0 < 0.01$) due to micropore filling. According to the IUPAC classification, the N₂ adsorption–desorption isotherms of the beta zeolite before and after desilication were close to type IV isotherm, which exhibited the typical characteristics of H4 hysteresis loop related to the uniformed pore formation [56, 76]. The information obtained from N₂ adsorption–desorption isotherms for all sample were summarized in Table 4.6. It was observed that the increase in the NaOH concentration from 0.25-0.75 M remarkably decreased the BET surface area (S_{BET}) and external surface area (S_{external}) from 673 to 578 cm³/g and from 283 to 161 cm³/g, respectively. This indicated that non-micropore area decreased after desilication due to Si leaching. Moreover, the pore volume of mesopore (V_{BJH}) of desilicated beta zeolite was lower resulting in the reduction of the total pore volume. However, the desilication could slightly expand both of average and BJH pore radius of zeolite from 19.8 to 21.3 Å and 3.87 to 3.98 Å, respectively when the desilication of the beta zeolite was performed in the presence of 0.50 M NaOH solution. When the concentration of NaOH solution increased to 0.75 M, microporous surface area increased to 417 cm³/g implying that the desilication generated vacancy secondary pore due to reduction of average pore radius. This was possible that the desilication at room temperature is not conducive to mesopore formation in the beta zeolite with a low Si/Al ratio, but the connectivity of the micropores was improved by the alkali treatment [77].

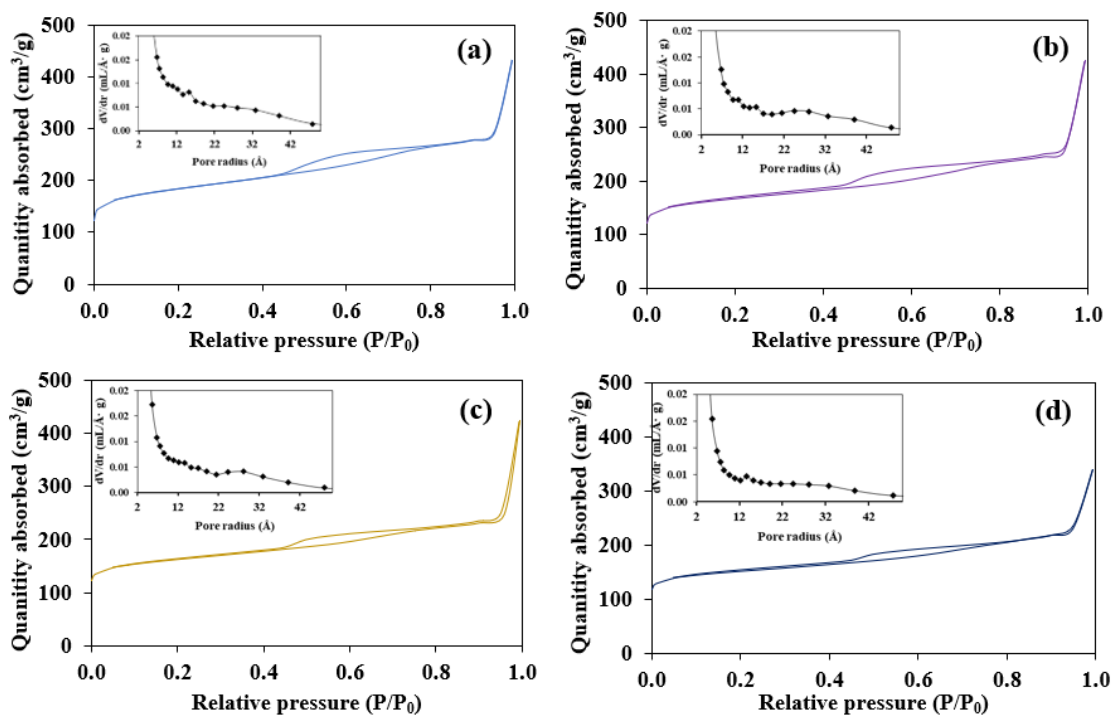


Fig. 4.18 N_2 adsorption-desorption isotherm and pore size distribution of (a) beta, (b) beta-0.25M-deS, (c) beta-0.50M-deS, and (d) beta-0.75M-deS.

Fig. 4.19 shows the N_2 adsorption-desorption isotherms of Ni-based catalyst supported on beta zeolite with and without the desilication using NaOH solution at different concentrations at room temperature. All calcined catalysts exhibited Types IV isotherm with H4 type hysteresis loop indicating the characteristics of the slit pore zeolites [56, 76]. The isotherms showed a rapid aggrandizement in adsorption, indicating that the mesopores were connected at the surface with intracrystalline micropores and caused the capillary condensation from agglomerated Ni particles on outside pore at P/P_0 in 0.95-1.00 range resulting in the increasing external surface area of the zeolite supports [57]. From the pore radius distribution, the Ni catalyst supported on the unmodified beta zeolite had the broad peak of the pore radius distribution in the range of 15-40 Å. For the desilicated beta zeolite, the high intensity of the pore radius distribution was observed at 15-30 Å resulting in the enhancement of the microporous surface area (S_{micro}) from 141 m^2/g to 170 m^2/g as shown in the inset in Fig. 4.19 and Table 4.9. However, the BET surface area (S_{BET}) and external

surface area (S_{external}) of catalysts remarkably decreased from 560 m^2/g to 513-536 m^2/g and 391 m^2/g to 366 m^2/g , respectively. Moreover, the total pore volume, microporous and BJH pore volume decreased for the Ni-based catalysts supported on desilicated beta zeolite prepared by using NaOH solution. This was possible that the agglomerated Ni particles on outside pore provided the higher external surface area than the zeolite supports to form new pores yielding the expanded average pore radius.

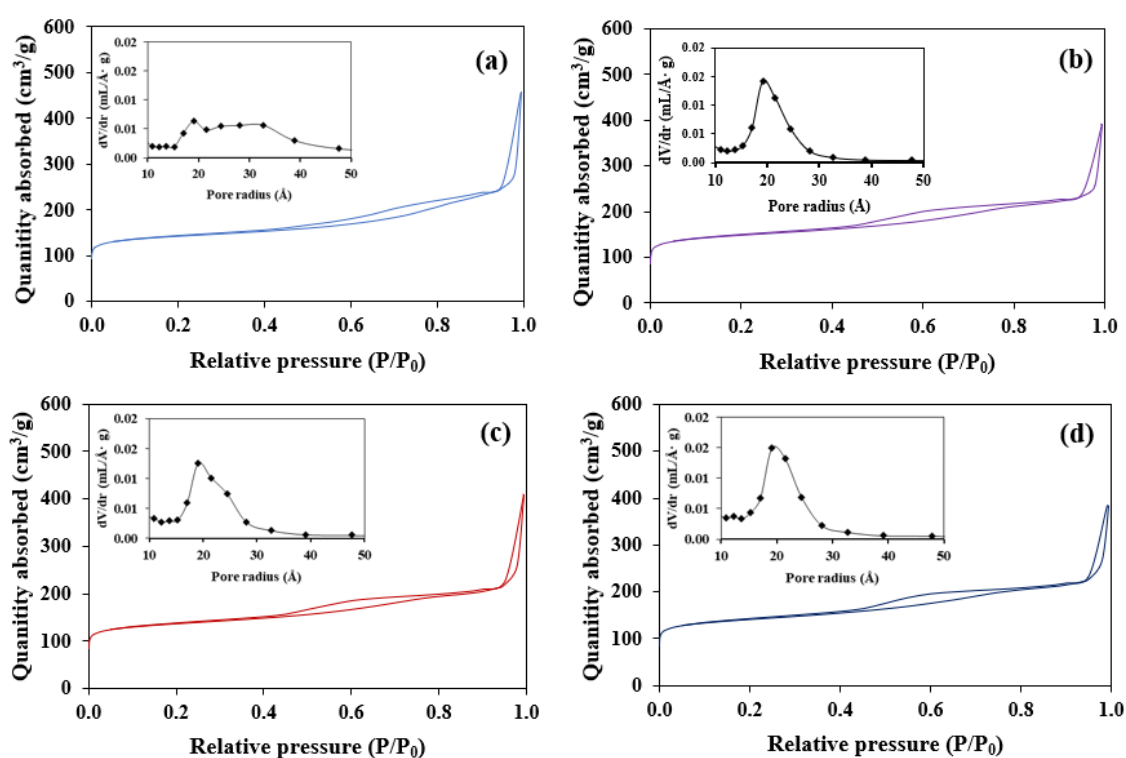


Fig. 4.19 N_2 adsorption-desorption isotherm and pore size distribution of (a) Ni/beta, (b) Ni/beta-0.25M-deS, (c) Ni/beta-0.5M-deS, and (d) Ni/beta-0.75M-deS catalysts.

Table 4.6 Textural properties of beta zeolite before and after desilication

Catalysts	Surface area(m ² /g)			Pore volume (cm ³ /g)			Pore radius (Å)		RC
	S ^a _{BET}	S ^b _{micro}	S ^c _{external}	V ^d _{micro}	V ^e _{BJH}	V ^f _{total}	R ^g _{avg}	R ^h _{BJH}	
beta	673	390	283	0.16	0.5	0.66	19.8	3.87	100
beta-0.25M-deS	622	408	214	0.16	0.49	0.65	21.1	3.93	94.2
beta-0.50M-deS	614	414	200	0.16	0.49	0.65	21.3	3.98	92.1
beta-0.75M-deS	578	417	161	0.16	0.36	0.52	18.1	4.01	92.6
Ni/beta	540	141	391	0.15	0.56	0.71	26.2	3.01	-
Ni/beta-0.25M-deS	519	146	376	0.15	0.47	0.62	23.9	3.13	-
Ni/beta-0.50M-deS	513	157	356	0.14	0.49	0.63	24.6	3.01	-
Ni/beta-0.75M-deS	536	170	366	0.15	0.48	0.63	22.1	3.01	-

^a MultiPoint BET method

^b t-method micropore surface area

^c t-method external surface area

^d Total pore volume for pores with Radius less than 1755.00 Å at P/Po = 0.994517

^e micropore volume was obtained using t-plot method.

^f mesopore volume was obtained from BJH method cumulative adsorption.

^g Average pore radius

^h Pore radius was obtained from BJH method cumulative adsorption.

The XRD patterns showed in Fig. 4.20 indicated that the zeolite before and after desilication via NaOH solution at room temperature with different concentrations exhibited the typical diffraction peaks of the BEA-type structure [48, 49]. This reflected that the zeolite framework was remained. However, the relative crystallinity (RC) decreased after desilication with increasing the NaOH concentrations as shown in Table 4.6. This implied that the alkaline treatment incurred a little damage on the framework of beta zeolite [78].

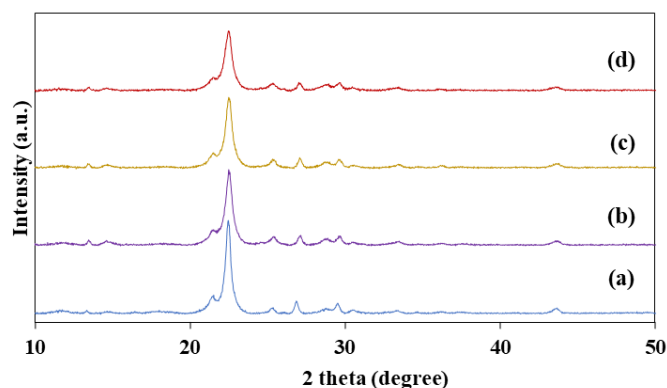


Fig. 4.20 XRD pattern of parent and desilicated zeolites (a) beta, (b) beta-0.25M-deS, (c) beta-0.50M-deS, and (d) beta-0.75M-deS.

Fig. 4.21 shows the ^{29}Si NMR spectra of beta zeolite. The resonance absorption of the Si atoms in $\text{Si}(\text{OAl})_n(\text{OSi})_{4-n}$ were designated for brevity as $\text{Si}(n\text{Al})$, where $n=0, 1, 2, 3$ and 4 corresponded to the number of framework Al atoms in the nearest surrounding of the particular Si atoms. There were three signals at $-98, -104,$ and -111 ppm attributed to the Si atoms bonded to neighboring Al species in the forms of $\text{Si}(2\text{Al}), \text{Si}(1\text{Al}),$ and $\text{Si}(0\text{Al}),$ respectively [79, 80]. The relative intensity of parent beta zeolite presented in Table 4.7 showed 60.8% $\text{Si}(2\text{Al}), 18.3\%$ $\text{Si}(1\text{Al}),$ and 20.9% $\text{Si}(0\text{Al}).$ After desilication, the signals of ^{29}Si NMR spectra of all desilicated zeolite samples appeared at the same positions. However, the intensity of the $\text{Si}(2\text{Al})$ signal was remarkably decreased with increasing NaOH concentration. This was possible that the mesopores were created after the removal of Si from the framework resulting in the higher number of defect sites [81]. When NaOH concentration increased to 0.50 M (beta-0.50M-deS), the relative peak area of $\text{Si}(2\text{Al})$ dramatically decreased to 37.8% with increasing the %relative area of $\text{Si}(0\text{Al}).$ This could be explained that $\text{Si}(2\text{Al})$ configuration consisting Si atom connected to the 2 Al atoms from the outside of four membered rings of beta zeolite could be more easily removed by basic solution [79]. This indicated that the desilication could decrease the amount of Si species of the parent beta zeolite and created some defect silanol groups in the zeolite framework [81].

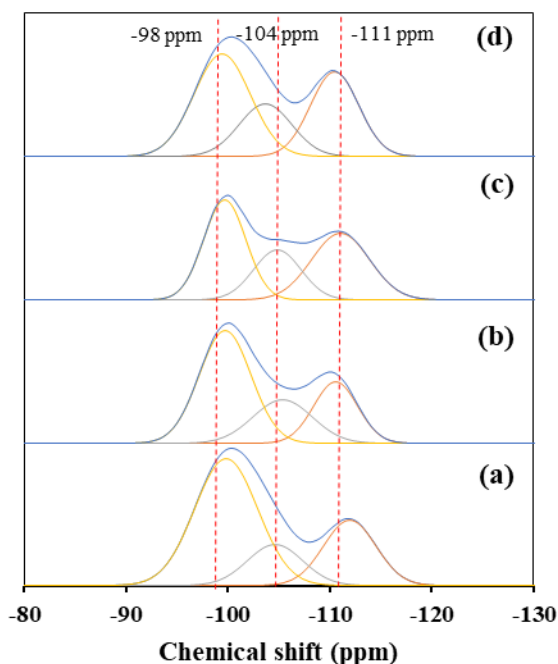


Fig. 4.21 ^{29}Si MAS NMR spectra of (a) beta, (b) beta-0.25M-deS, (c) beta-0.50M-deS, and (d) beta-0.75M-deS.

Table 4.7 %Relative peak area for each signal in ^{29}Si MAS NMR spectra of beta zeolite before and after desilication

Supports	Si(2Al) [%] (-98 ppm)	Si(1Al) [%] (-104 ppm)	Si(0Al) [%] (-111 ppm)
beta	60.8	18.3	20.9
beta-0.25M-deS	52.6	23.3	24.1
beta-0.50M-deS	37.8	21.2	34.9
beta-0.75M-deS	48.3	24.9	34.7

The surface acidity of the beta zeolites before and after desilication was investigated using NH_3 -TPD and py-FTIR spectroscopy techniques as shown in Fig. 4.22 and 4.23, respectively. The detail of analysis was summarized in Table 4.8. To consider the NH_3 -TPD analysis, the beta zeolite with Si/Al ratio of 14.4 had the total acidity of 1,561 $\mu\text{mol NH}_3/\text{g}$ with weak, medium and strong acid sites of 467, 676 and 418 $\mu\text{mol NH}_3/\text{g}$, respectively. After dealumination using various concentrations of NaOH solution, the Si/Al ratio of the desilicated beta zeolite decreased to 12.4 with

lowering the total acidity to 902 $\mu\text{mol NH}_3/\text{g}$ resulting from the reduction of the amount of all acidic sites when the concentration of NaOH solution was 0.75 M. It was possible that the high NaOH concentration could remove the silanol groups for the generation of mesopores [76].

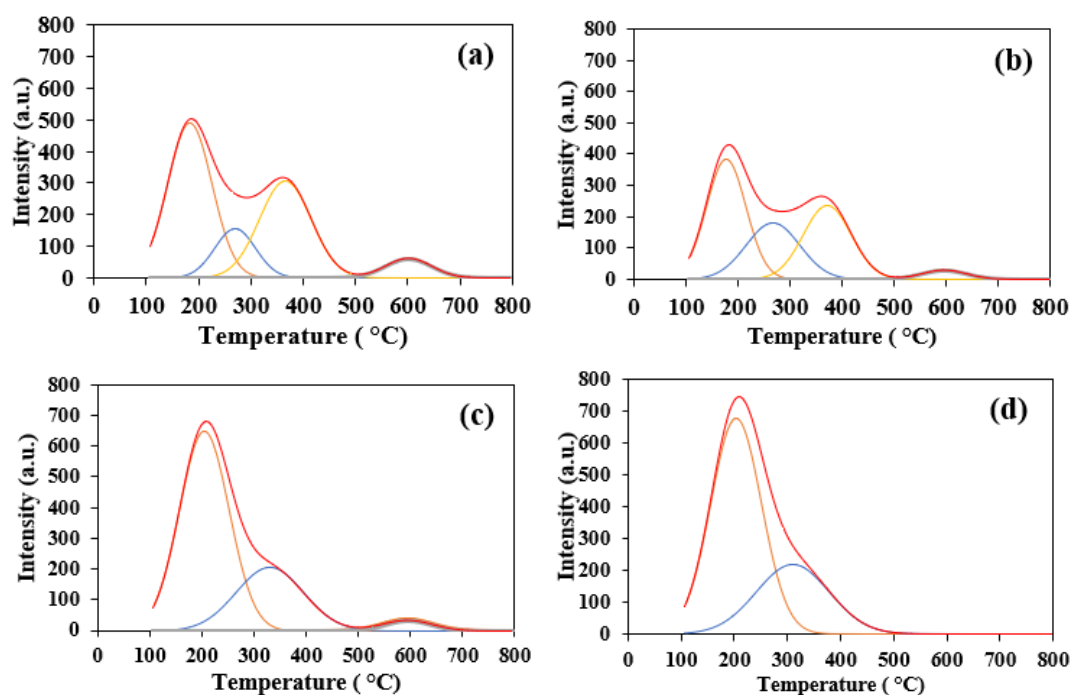


Fig. 4.22 NH_3 -TPD profiles of (a) beta, (b) beta-0.25M-deS, (c) beta-0.50M-deS, and (d) beta-0.75M-deS

For the Bronsted and Lewis acid sites using py-FTIR spectroscopy, Fig. 4.22a showed the signal at $1,550\text{ cm}^{-1}$ and $1,450\text{ cm}^{-1}$ attributed to the Bronsted and Lewis acid sites of the beta zeolite, respectively. The bands at $1,450\text{ cm}^{-1}$ correspond to pyridine interacting with strong Lewis acidic centres (Al^{3+}) and those at $1,445\text{ cm}^{-1}$ to pyridine interacting with weak Lewis acidic centres (hydroxyls) and/or pyridine physisorbed. From Fig. 4.23, the signal at $1,445\text{ cm}^{-1}$ was increased highly intensity after desilication. This was possibly that desilication generated hydroxyl on the surface of beta zeolite and Na ion could absorb pyridine. This phenomenon was also observed in the V loading on beta zeolite from the literature [82].

From the Table 4.8, the amounts of each acidic site of parent beta zeolite that were calculate from amount of pyridine degassed at 50°C 30 min were at 212 $\mu\text{mol py/g}$ for Bronsted acid site and at 97.1 $\mu\text{mol py/g}$ for Lewis acid site. When

beta zeolite was desilicated using 0.25 M NaOH solution, the signal of Lewis acid site was more intensified to 482 $\mu\text{mol py/g}$, while the intensity of Bronsted acid sites was decreased with the pyridine consumption of 133 $\mu\text{mol py/g}$. This was possibly due to the existing Na ion generated from alkaline-exchange with H atom of Si-OH group in the zeolite framework resulting in decreasing Bronsted acid site. The Bronsted acid site of desilicated trend to decrease with increasing the NaOH concentration resulting to lowering B/L acid ratio [83, 84]. This observation confirmed the replacement of H by Na in the desilicated beta zeolite framework.

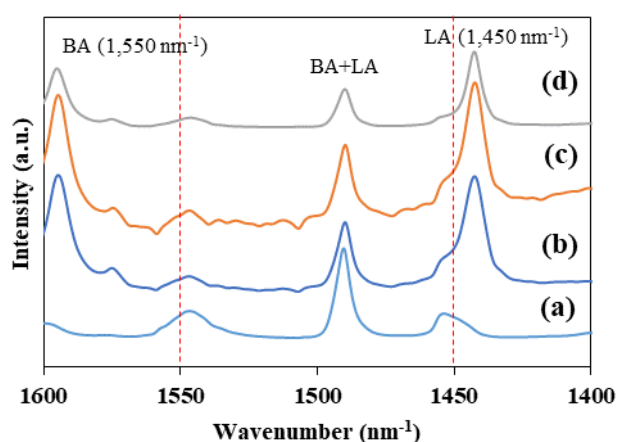


Fig. 4.23 Py-FTIR spectra of (a) beta, (b) beta-0.25M-deS, (c) beta-0.50M-deS, and (d) beta-0.75M-deS.

Table 4.8 Acidic properties of beta zeolite before and after desilication

Supports	Si/Al atomic ratio ^a	NH ₃ -TPD ($\mu\text{mol NH}_3/\text{g}$)			Total acid	Py-FTIR ($\mu\text{mol py/g}$)		
		Weak (< 200 °C)	Medium (200-350 °C)	Strong (350-600 °C)		Lewis (L)	Bronsted (B)	B/L
beta	14.4	467	676	418	1,561	97.1	212	2.18
beta-0.25M-deS	13.0	386	765	239	1,390	482	133	0.28
beta-0.5M-deS	12.7	333	585	152	1,070	481	111	0.23
beta-0.75M-deS	12.4	277	524	101	902	225	59.5	0.26

^a evaluated by % atomic from EDX.

Fig. 4.24 showed TEM images of the NiO particles supported on beta zeolite with and without desilication. The histograms of particle size distributions were inserted in their corresponding TEM images and NiO particles size. The average NiO particle size of Ni/beta was at 22.8 nm in Fig. 4.24a. The NiO particle size of Ni/beta-0.25M-deS were slightly decreased to 17.6 nm as shown in Fig. 4.24b. This was possibly that desilication increased interaction between NiO particles and surface of desilicated beta zeolite to obtained smaller particle [85].

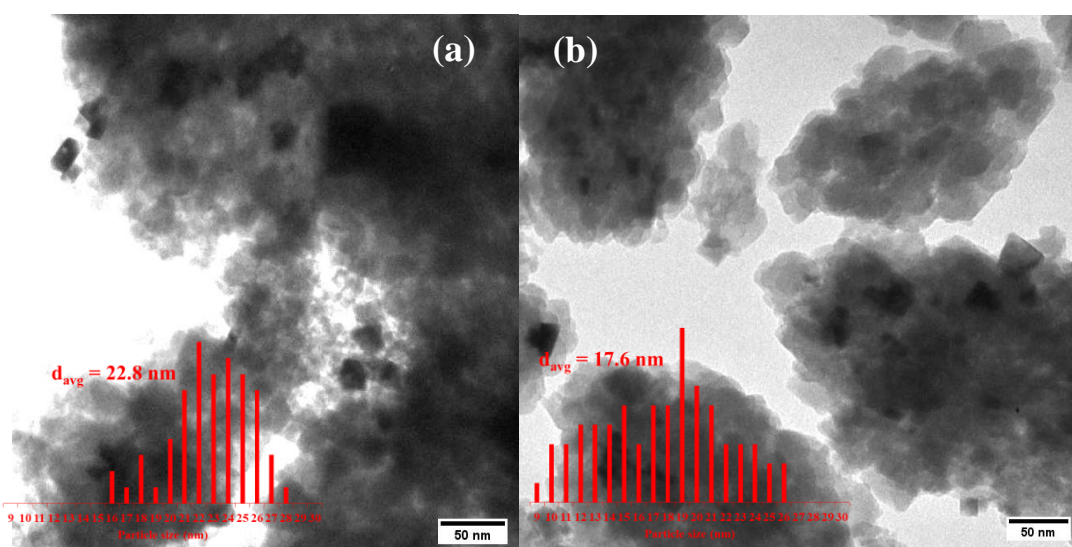


Fig. 4.24 TEM images and distribution of the size of nickel crystallites on the surface of (a) Ni/beta and (b) Ni/beta-0.25M-deS catalysts.

Fig. 4.25 shows the XRD patterns of Ni-based catalysts. The results indicated that the signals at 2θ of 37.2°, 43.2°, 62.8°, 75.3°, and 79.4° were attributed to the nickel oxide (NiO) phase [60]. The XRD technique was also used to estimate the NiO crystallite size by Scherrer equation [42]. From Table 4.10, the NiO crystallite size on the desilicated zeolites was in the range of 22.8-23.4 nm, which was slightly larger than one supported on the unmodified zeolite (22.3 nm). This implied that the interaction between Ni particles and surface of desilicated zeolite was lower than supported on parent zeolite. The result was also confirmed by using CO-pulse technique (Table 4.10). This was possible that the interaction between Ni particles

and surface of desilicated zeolite was lower resulting in the smaller degree of Ni dispersion from 1.67% to 0.35-0.93%.

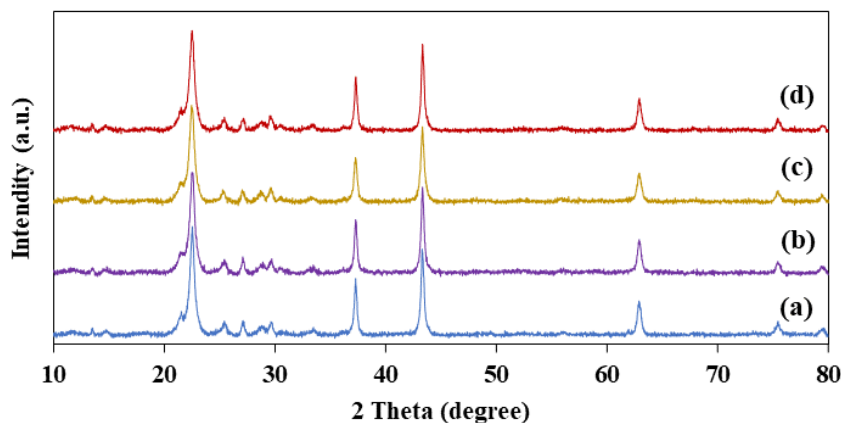


Fig. 4.25 XRD patterns of (a) Ni/beta, (b) Ni/beta-0.25M-deS, (c) Ni/beta-0.50M-deS, and (d) Ni/beta-0.75M-deS catalysts.

Since the size of the NiO particles and reducibility of the catalyst strongly affect the catalytic activity, the reduction ability of Ni-based catalyst was characterized by hydrogen temperature programmed reduction (H_2 -TPR) and corresponding profiles are shown in Fig. 4.26. It exhibited that the two peaks of H_2 -TPR profile of Ni catalysts supported on beta zeolite at 400 °C and 560 °C. This lower reduction temperature at 400 °C was attributed to extraframework NiO and/or octahedral Ni(II) species [59, 61]. Whereas, the reduction temperature at 560 °C was assigned as the reduction of Na^+ ion. Without the leaching of NaOH after desilication, the desilicated beta zeolite contained Ni^+ ion, which was ion exchanged with Ni to form $NiOH^+$ ions in extraframework of zeolite [86, 87]. The Ni/desilicated zeolite catalyst showed the higher reduction temperature reflecting the stronger metal support interaction resulting in the lower reducibility ca. 75.4-79.7%, while the Ni/beta catalyst had 88.6% reducibility. Moreover, the degree of Ni dispersion was lower possibly due to the slightly large NiO particle size as shown in Table 4.9.

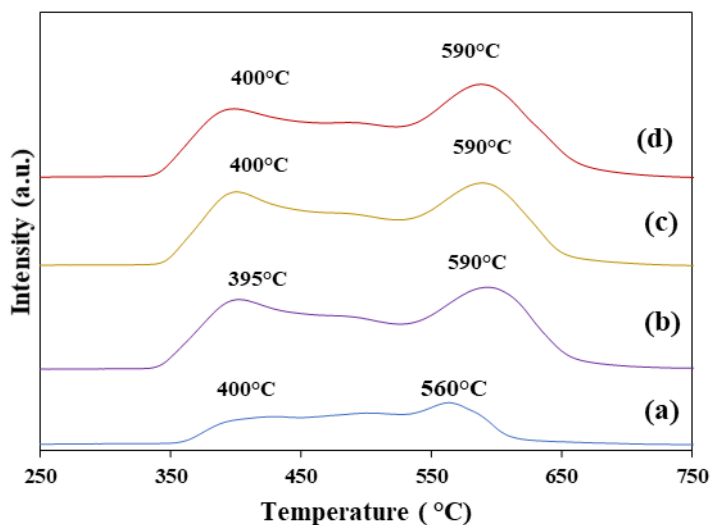


Fig. 4.26 H₂ TPR profiles of (a) Ni/beta, (b) Ni/beta-0.25M-deS, (c) Ni/beta-0.50M-deS, and (d) Ni/beta-0.75M-deS catalysts.

Table 4.9 Actual Ni content, NiO crystalline size, Ni dispersion, H₂ consumption and reducibility of Ni-based catalysts supported on beta zeolites with and without desilication

Catalysts	Actual Ni content (%) ^a	NiO crystalline size (nm) ^b	Ni dispersion ^c (%)	H ₂ consumption ^d (mmol/g)	Reducibility ^e (%)
Ni/beta	9.5	22.3	1.67	2.37	88.6
Ni/beta-0.25M-deS	8.0	22.8	0.35	1.91	75.4
Ni/beta-0.50M-deS	8.2	23.1	0.93	2.03	78.3
Ni/beta-0.75M-deS	8.2	23.4	0.79	2.06	79.7

^a %wt of Ni loading on zeolite was measured by ICP OES.

^b NiO crystalline size was measured from XRD.

^c H₂ consumption of Ni zeolite catalysts was measured from H₂ TPR profiles.

^d %metal dispersion was measured from CO-pulse method. ^e micropore volume was obtained using t-plot method.

^e Evaluated by comparing the total H₂ consumption obtained from the H₂-TPR technique and the theoretical value calculated from the reduction of all metal oxides.

4.2.2 Hydroisomerization of palm olein over Ni based catalysts supported on desilicated beta zeolite

Fig. 4.27 showed the product distribution obtained from the hydroisomerization of palm olein operated at 340 °C under 40 bar initial H₂ pressure for 5 h over Ni-based catalyst supported on the beta zeolite with and without desilication. The use of Ni/beta catalyst gave 74.5% liquid product, 24.0% gas product and 1.42% solid product. The Ni/desilicated beta zeolite catalysts did not significantly affect the product distribution obtained from the same condition. However, the solid product generated from the system using Ni/desilicated zeolite slightly decreased reflecting the inhibition of coke deposition on the surface of the catalyst due to the lower acidity of the desilicated support. The results were confirmed by the TGA thermograms of the spent catalysts as shown in Fig. 4.28 [16].

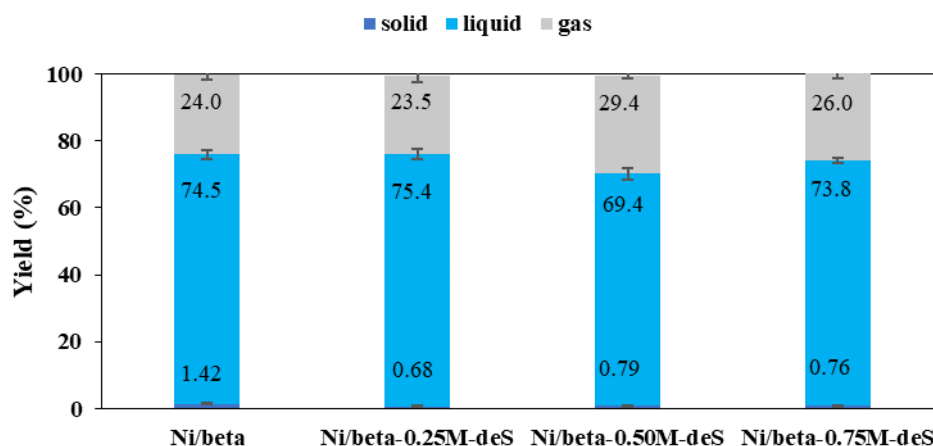


Fig. 4.27 Product distribution obtained from hydroisomerization of palm olein at 340 °C under 40 bar initial H₂ pressure over Ni catalyst supported on desilicated zeolite.

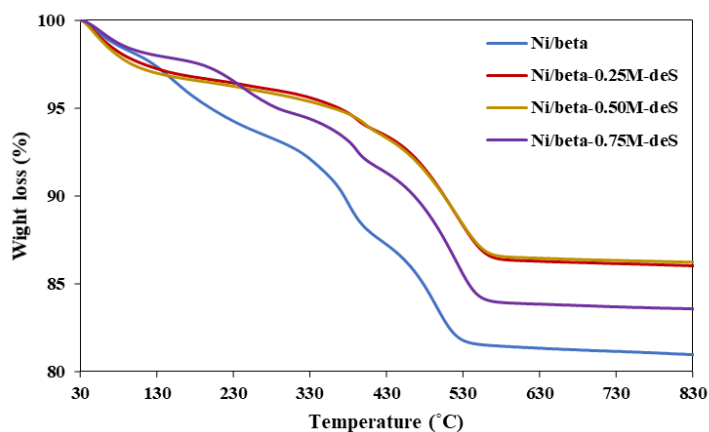


Fig. 4.28 TGA thermograms of spent Ni-based catalysts prepared by using desilicated beta zeolite applied in hydroisomerization of palm olein at 340 °C under 40 bar initial H₂ pressure.

In Fig. 4.29, the %selectivity of each composition in liquid products was calculated from peak area from GC-MS chromatograms. The Ni/beta catalyst operated on hydroisomerization of palm olein at 340 °C under 40 bar initial H₂ pressure provided the liquid product consisted of 28.3% n-alkanes, 40.9% iso-alkanes, 18.4% aromatics, 8.16% cyclics, 2.88% oxygenated compounds and 1.81% unsaturated species. The use of Ni/beta-0.25M-deS and Ni/beta-0.50M-deS catalyst provided the liquid product having lower content of iso-alkanes with higher formation of aromatics and oxygenated compounds. This indicated that the higher Lewis acid site with lowering B/L acid ratio promoted a significant role in the production of renewable aromatics by the tandem Diels–Alder cycloaddition in aromatization process of olefins (1) and alkanes (2) from hydrocracking as shown in Fig. 4.30 [67]. The Lewis acid site was required to promote aromatization [74]. However, the absence of Bronsted acid site decreased hydrodeoxygenation resulting in the higher amount of oxygenated compounds [88]. In the case of Ni/beta-0.75M-deS, the liquid biofuel contained the highest n-alkanes content (49.4%) with lowering iso-alkanes fraction (26.5%). This was indicated that the lowest amount of Lewis and Bronsted acid site decreased hydrocracking rate to generate more carbonium ion [16, 67].

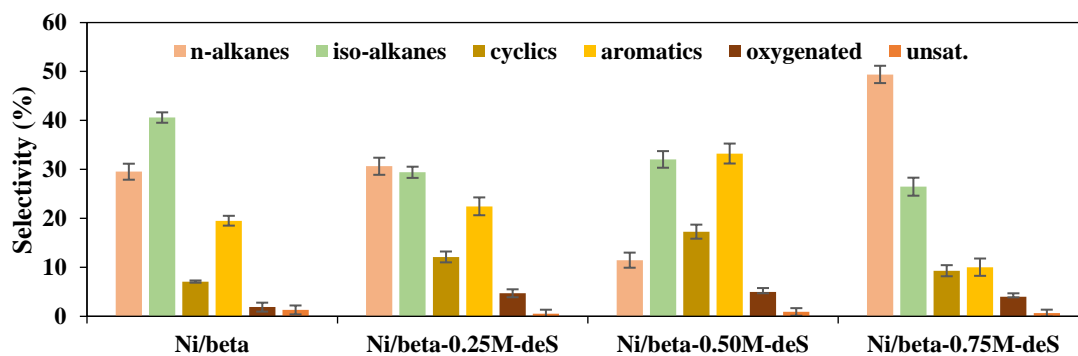


Fig. 4.29 Selectivity to chemical compositions in the liquid product obtained from the hydroisomerization of palm olein catalyzed by Ni-based catalysts supported on beta zeolite with and without desilication under 40 bar initial H_2 pressure at 340 °C for 5 h.

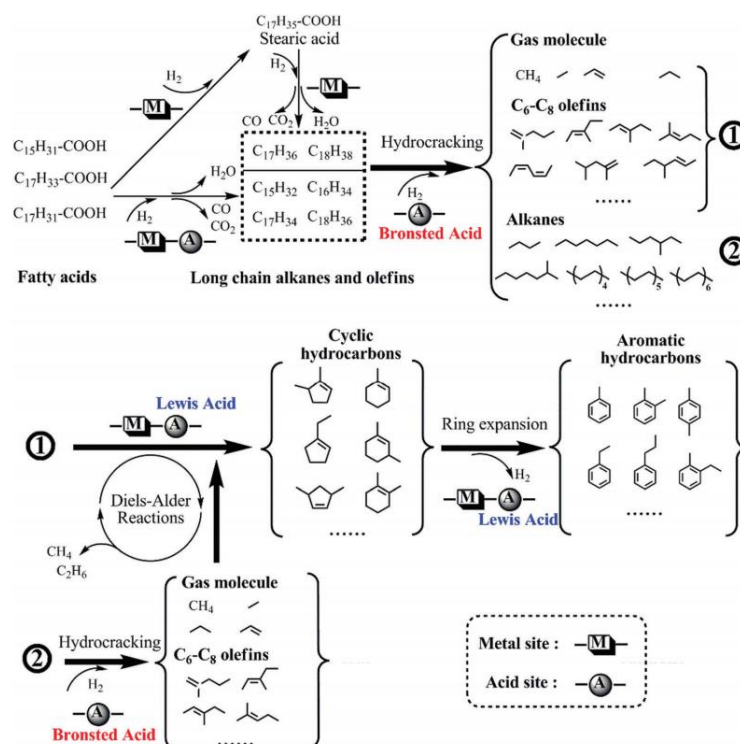


Fig. 4.30 Proposed conversion routes for aromatics hydrocarbon formation in hydro-processing of fatty acids [67].

The hydrocarbon types in the obtained liquid products from hydroisomerization of palm olein were also classified as bio-gasoline (<C8), bio-jet fuel (C9-C14) and green diesel (C15-C18) following the carbon number of n-alkanes and iso-alkanes as shown in Fig. 4.31. The use of Ni/beta catalyst obtained the liquid biofuel having 5.15% bio-gasoline, 37.4% bio-jet fuel and 22.5% green diesel with iso/normal alkane ratio at 1.65. In the case of Ni/beta-0.25M-deS, Fig. 4.29b indicated that the bio jet fuel range fraction was decreased to 24.6% with lower iso/normal alkane ratio (0.93). This indicated that high Lewis acid site decreased aliphatic jet fuel range in hydroconversion of triglyceride [74]. When increasing NaOH concentration to 0.50 M (Ni/beta-0.50M-deS), liquid product contained higher bio-gasoline fraction (10.0%) and lower green diesel (9.34%) with increasing iso/normal alkane ratio (2.49). It could be explained that higher Lewis acid sites promoted aromatization to decrease n-alkane obtained higher iso/normal alkane ratio and lower diesel range [74]. Moreover, iso-alkane content slightly decreased comparing Ni/beta reflecting in lower jet fuel fraction. For the use of Ni/beta-0.75M-deS, liquid biofuel obtained high green diesel fraction resulting to lower iso/normal ratio (0.30) due to the lowest amount of acid site that decreased the ability to hydroisomerization and hydrocracking process [16].

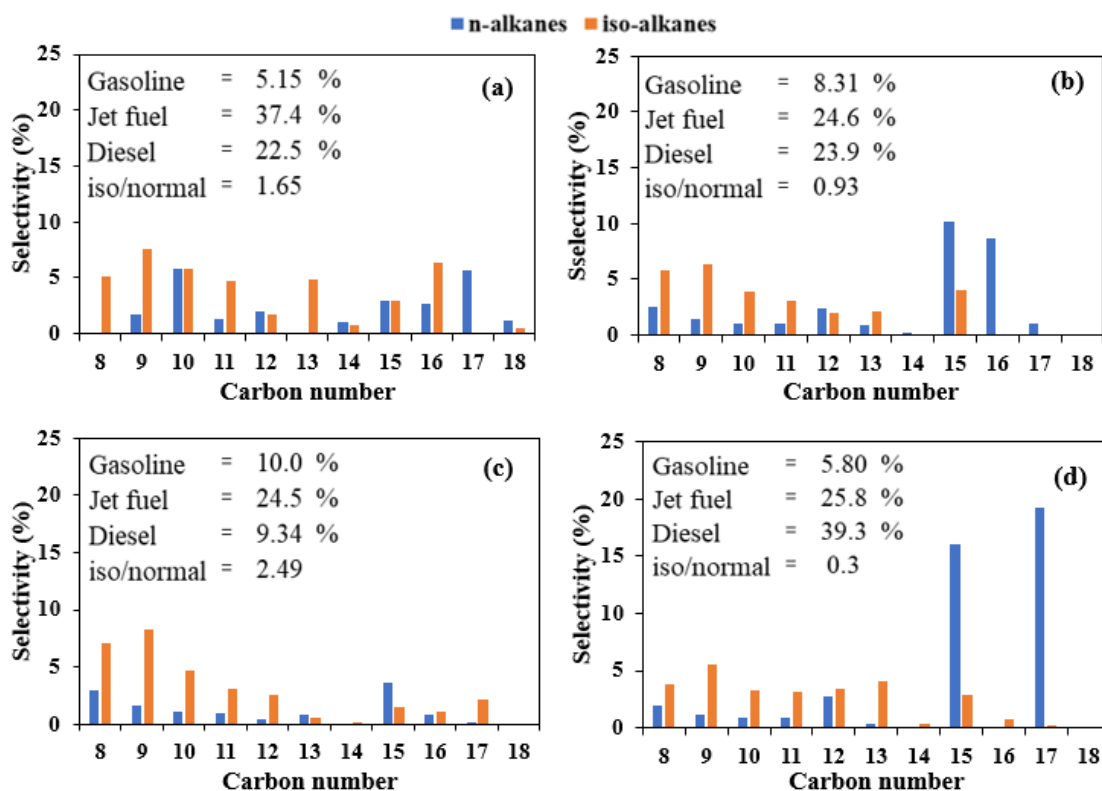


Fig. 4.31 Distribution of carbon number in liquid products obtained from the hydroisomerization of palm olein over (a) beta, (b) beta-0.25M-des, (c) beta-0.50M-deS, and (d) beta-0.75M-deS catalysts at 340 °C under 40 bar initial H₂ pressure.

4.3 Freezing points of biofuel from hydroisomerization

The freezing point (T_f) of the liquid biofuels containing various iso/normal alkane ratios obtained from hydroisomerization of palm olein was determined by using DSC technique as shown in Fig. 4.32. T_{onset} of the exothermic peak obtained from the cooling curves was corresponded to the T_f to crystallize the fuel samples [89]. Since the key properties of the aviation fuels is the freezing point [89], the effect of the iso/normal alkane ratio on the T_f of biofuel from hydroisomerization of palm olein was evaluated as shown in Fig. 4.31. The commercial jet A-1 had T_f at -73.5 °C indicating long-duration, high-altitude aircraft flights expose jet fuel to extremely low ambient temperatures (below -70 °C). The low-temperature fluidity of jet fuels is routinely evaluated according to their freezing point [89]. The use of Ni/beta

catalyzed system at 340 °C under 30 bar initial H₂ pressure having iso/normal alkane ratio 0.30 was appeared T_f (-19.9 °C). When initial H₂ pressure increased to 40 bar, T_f of liquid biofuels decreased to -36.0 °C. This was possible that the reaction condition applied to produce these biofuels generated the smaller iso-molecules in the range of bio-gasoline to decrease the freezing point of the obtained liquid product [63]. At the same conditions, Ni/0.25M-deA, which had higher iso/normal alkane ratio at 2.54 gave the lower T_f from -36.0 °C to 60.1 °C. this was possible that the increase in the content of branched compounds makes it difficult to pack the chains and, consequently, decreased the freezing temperature [63].

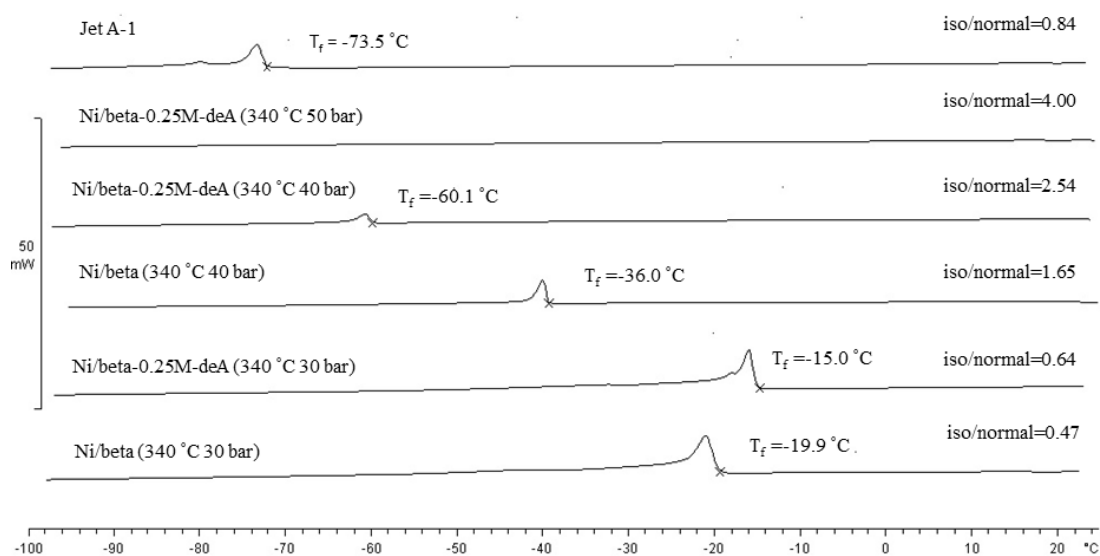


Fig. 4.32 DSC thermograms of liquid biofuels having different iso/normal alkane ratios obtained from hydroisomerization of palm olein over Ni-based catalyst supported on beta zeolite and commercial jet A-1.

CHAPTER 5

CONCLUSION

5.1 Conclusion

This research work aimed to investigate the hydroisomerization of palm olein for bio-jet fuel production via Ni based catalyst supported on dealuminated and desilicated beta zeolite. The effect of reaction parameters: types of support, concentration of acid and base, initial H₂ pressure and reaction temperature on the %selectivity of biofuel in bio-jet fuel range was investigated and the biofuel properties according to ASTM specification (freezing point) was also studied. The results of this research work can be summarized as follows:

5.1.1 The effect of dealumination on hydroisomerization of palm olein

5.1.1.1 Catalyst characterization

The preparation of mesoporous beta zeolite via dealumination by using HF/NH₄F solution at room temperature was successfully to enlarge average pore radius from 19.8 Å to 24.1-26.3 Å. The total acidity on the surface from NH₃-TPD was increased after dealumination at 0.75 M HF concentration in HF/NH₄F solution. Moreover, the Lewis acid site increased when increased HF concentration. When loading Ni metal on dealuminated beta zeolite, H₂-TPR profile showed the high H₂ consumption at high temperature reflecting to stronger interaction between Ni particles and zeolite supports to obtain high Ni dispersion from CO pulse analysis. Ni/beta-0.25M-deA obtained the highest Ni dispersion and H₂ consumption.

5.1.1.2 Catalytic performance

The hydroisomerization of palm olein via Ni-based catalyst supported on with and without dealumination by using HF/NH₄F solution was investigated in two parameters: effect of initial H₂ pressure and reaction temperature. The investigation of various initial H₂ pressure, the use of Ni/beta-0.25M-deA gave the highest

performance to iso/normal alkanes ratio of 4.00 from the system at 340 °C 50 bar. When the varied temperature, Ni/beta-0.25M-deA gave the highest selectivity jet fuel range (48.0%) of aliphatic hydrocarbon in liquid biofuel from the system at 320 °C under 40 bar initial H₂ pressure. The increased initial H₂ pressure and reaction temperature trended to increase aromatic content. Accounting to ASTM D7566 specification, aromatic content was maximum at 25 wt%. Thus, to optimize the conditions would performance at low initial H₂ pressure and reaction temperature.

5.1.2 The effect of desilication on hysisomerization of palme olein

5.1.2.1 Catalyst characterization

The preparation of mesoporous beta zeolite via desilication by using NaOH solution at room temperature. The textural properties could not change significantly due to the mind condition to maintain the acidity on the surface of beta zeolite. Although, the total acid site from NH₃-TPD of desilication trended to decrease due to the Na⁺ ion on the surface from the NaOH solution reduced the Bronsted acid sites. The Lewis acid sites increased from the metal ion on the surface. When impregnated Ni metal to desilicated beta zeolite, the Ni particles had low interaction to zeolite resulting in increasing NiO crystalline size from 22.3 nm to 23.4 nm with decreasing Ni dispersion.

5.1.2.2 Catalytic performance

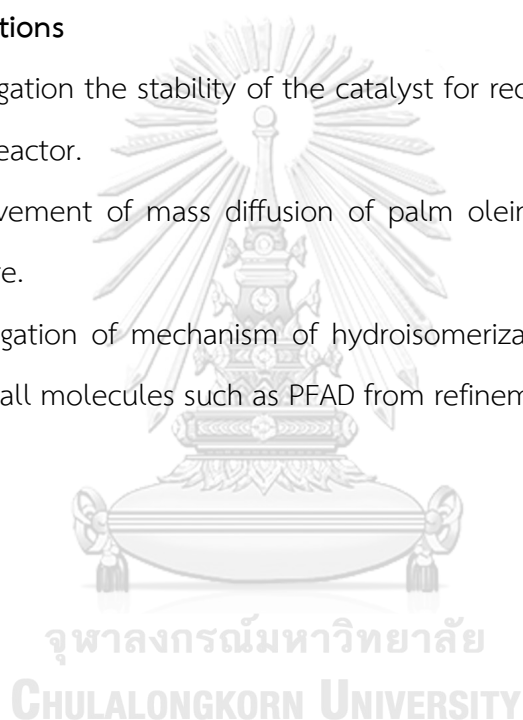
The performance of Ni/desilicated beta zeolite on hydroisomerization of palm olein in various NaOH concentration, the use of Ni/desilicated beta zeolite could reduce coke formation on the spent catalyst. The high Lewis acid sites of Ni/desilicated zeolite catalyst promoted alkene aromatization resulting in high aromatic content and cyclics hydrocarbon, which was hydrogenated under excess H₂ pressure. Whereas, the use of Ni/beta-0.75M-deS gave the lowest aromatic selectivity and the highest n-alkane selectivity due to the lowest total acid sites on the catalyst.

5.1.3 Biofuel properties in freezing point

The freezing point of biofuels from hydroisomerization of palm olein were determined by using DSC technique. The use of Ni/beta-0.25M-deA gave the freezing point at $-60.1\text{ }^{\circ}\text{C}$ from the system $340\text{ }^{\circ}\text{C}$ 40 bar initial H_2 pressure with iso/normal alkane ratio at 2.54 comparing the commercial jet A-1 at $-73.5\text{ }^{\circ}\text{C}$ The high iso/normal alkane ratio could reduce the freezing point to low temperature to closer the freezing point of commercial jet A-1 fuel without distillation.

5.2 Recommendations

- 1) The investigation the stability of the catalyst for recycle use should catalyzed in fix bed reactor.
- 2) The improvement of mass diffusion of palm olein should modified at high temperature.
- 3) The investigation of mechanism of hydroisomerization of palm olein would use the small molecules such as PFAD from refinement of crude palm oil.



APPENDIX A

CALCULATION OF NI-BASED CATALYST PREPARATION

Calculation of amount of Ni precursor to prepare the Ni-based catalyst

Sample Ni-based catalyst supported on beta zeolite was 10 wt% catalyst was prepared 10 g catalyst

$$\text{Amount of zeolite} = 10 \text{ g catalyst} \times \frac{90 \text{ g zeolite}}{100 \text{ g catalyst}} = 9 \text{ g zeolite}$$

$$\text{Amount of Ni metal} = 10 \text{ g catalyst} \times \frac{10 \text{ g Ni metal}}{100 \text{ g catalyst}} = 1 \text{ g Ni metal}$$

$\text{Ni}(\text{NO}_3)_2 \cdot 6\text{H}_2\text{O}$ is used as Ni precursor having $M_w=290.8$ g/mol. Ni metal has $M_w=58.69$ g/mol

$$\text{Amount of Ni precursor} = 1 \text{ g Ni metal} \times \frac{290.8 \text{ g Ni precursor}}{1 \text{ mol Ni precursor}} \times \frac{1 \text{ mol Ni precursor}}{58.69 \text{ g Ni metal}}$$

$$\text{Amount of Ni precursor} = 4.95 \text{ g Ni precursor}$$

APPENDIX B

CALCULATION OF PRODUCT YIELDS

Calculation in product distribution

$$\text{Yield of solid product} = \frac{W_{\text{spent catalyst}} \times \frac{\% \text{coke deposition}^a \times W_{\text{catalyst}}}{100 - \% \text{coke deposition}}}{W_{\text{palm olein}}} \times 100$$

^a %coke deposition obtained from weight loss in temperature range 300-700 °C via TGA analysis

$$\text{Yield of gas product} = \frac{W_{\text{palm olein}} - W_{\text{spent catalyst}}}{W_{\text{palm olein}}} \times 100$$

$$\text{Yield of liquid product} = \frac{W_{\text{palm olein}} - W_{\text{solid product}} - W_{\text{gas product}}}{W_{\text{palm olein}}} \times 100$$

Where: $W_{\text{palm olein}}$ is the weight of palm olein

$W_{\text{spent catalyst}}$ is the weight of spent catalyst from hydroisomerization of palm olein

APPENDIX C

CALCULATION OF SELECTIVITY IN BIOFUELS

The selectivity of bio-gasoline, bio-jet fuel and green diesel was also defined based on peak area fraction of n-alkanes and iso-alkanes from GCMS analysis as follows.

$$\text{gasoline selectivity} = \frac{(\text{product C8})}{(\text{product C8}) + (\text{product C9-C14}) + (\text{product C15-C18})}$$

$$\text{jet fuel selectivity} = \frac{(\text{product C9-C14})}{(\text{product C8}) + (\text{product C9-C14}) + (\text{product C15-C18})}$$

$$\text{diesel selectivity} = \frac{(\text{product C15-C18})}{(\text{product C8}) + (\text{product C9-C14}) + (\text{product C15-C18})}$$

Where: (Product C8) is an peak area fraction of the product in the range of aliphatic hydrocarbon <C8.

(ProductC9 – C14) is an area fraction of the product in the range of aliphatic hydrocarbon C9 – C14.

(ProductC15 – C18) is an area fraction of the product in the range of aliphatic hydrocarbon C15 – C18.

REFERENCES

1. Union, E. *Biofuels*. 2014 20 November 2019 [cited 2019 10 November].
2. *Post-COVID-19 Green Recovery Must Embrace Sustainable Aviation Fuels*. 2020 9 July 2020; Available from: <https://www.iata.org/en/pressroom/pr/2020-07-09-01/>.
3. Moore, R.H., et al., *Biofuel blending reduces particle emissions from aircraft engines at cruise conditions*. *Nature*, 2017. **543**(7645): p. 411-415.
4. Wang, W.-C. and L. Tao, *Bio-jet fuel conversion technologies*. *Renewable and Sustainable Energy Reviews*, 2016. **53**: p. 801-822.
5. Bangjang, T., A. Kaewchada, and A. Jaree, *Hydroprocessing of palm oil using Rh/H-ZSM-5 for the production of biojet fuel in a fixed bed reactor*. *The Canadian Journal of Chemical Engineering*, 2020. **99**(2): p. 435-446.
6. Kaewtrakulchai, N., et al., *Palm Oil Conversion to Bio-Jet and Green Diesel Fuels over Cobalt Phosphide on Porous Carbons Derived from Palm Male Flowers*. *Catalysts*, 2020. **10**(6).
7. Hannah Ritchie, M.R. *palm oil*. 2020 June 2021 [cited 2021 20 June].
8. Kim, M.Y., et al., *Maximizing Biojet Fuel Production from Triglyceride: Importance of the Hydrocracking Catalyst and Separate Deoxygenation/Hydrocracking Steps*. *ACS Catalysis*, 2017. **7**(9): p. 6256-6267.
9. Dik, P.P., et al., *Hydroprocessing of hydrocracker bottom on Pd containing bifunctional catalysts*. *Catalysis Today*, 2016. **271**: p. 154-162.
10. Istadi, I., et al., *Enhancing Brønsted and Lewis Acid Sites of the Utilized Spent RFCC Catalyst Waste for the Continuous Cracking Process of Palm Oil to Biofuels*. *Industrial & Engineering Chemistry Research*, 2020. **59**(20): p. 9459-9468.
11. Studentschnig, A.F.H., S. Schober, and M. Mittelbach, *Conversion of Crude Palm Oil into Hydrocarbons over Commercial Raney Nickel*. *Energy & Fuels*, 2013. **27**(12): p. 7480-7484.
12. Feng, F., et al., *Selective Hydroconversion of Oleic Acid into Aviation-Fuel-Range Alkanes over Ultrathin Ni/ZSM-5 Nanosheets*. *Industrial & Engineering Chemistry*

- Research, 2019. **58**(14): p. 5432-5444.
13. de Barros Dias Moreira, J., D. Bastos de Rezende, and V. Márcia Duarte Pasa, *Deoxygenation of Macauba acid oil over Co-based catalyst supported on activated biochar from Macauba endocarp: A potential and sustainable route for green diesel and biokerosene production*. Fuel, 2020. **269**.
 14. Straka, P., et al., *The Effect of the Reaction Conditions on the Properties of Products from Co-Hydrotreating of Rapeseed Oil and Petroleum Middle Distillates*. Catalysts, 2021. **11**(4).
 15. Kang, K.H., et al., *A review on the Mo-precursors for catalytic hydroconversion of heavy oil*. Journal of Industrial and Engineering Chemistry, 2019. **76**: p. 1-16.
 16. Hengsawad, T., et al., *Effect of Metal–Acid Balance on Hydroprocessed Renewable Jet Fuel Synthesis from Hydrocracking and Hydroisomerization of Biohydrogenated Diesel over Pt-Supported Catalysts*. Industrial & Engineering Chemistry Research, 2018. **57**(5): p. 1429-1440.
 17. Subsadsana, M. and C. Ruangviriyachai, *Effect of NiW Modified HZSM-5 and HY Zeolites on Hydrocracking Conversion of Crude Palm Oil to Liquid Hydrocarbons*. Oriental Journal of Chemistry, 2016. **32**(2): p. 839-844.
 18. Wang, X., X. Zhang, and Q. Wang, *N-dodecane hydroisomerization over Pt/ZSM-22: Controllable microporous Brønsted acidity distribution and shape-selectivity*. Applied Catalysis A: General, 2020. **590**.
 19. Chintakanan, P., et al., *Bio-jet fuel range in biofuels derived from hydroconversion of palm olein over Ni/zeolite catalysts and freezing point of biofuels/Jet A-1 blends*. Fuel, 2021. **293**.
 20. Gutiérrez-Antonio, C., et al., *A review on the production processes of renewable jet fuel*. Renewable and Sustainable Energy Reviews, 2017. **79**: p. 709-729.
 21. Qin, Z., J.-P. Gilson, and V. Valtchev, *Mesoporous zeolites by fluoride etching*. Current Opinion in Chemical Engineering, 2015. **8**: p. 1-6.
 22. Bai, R., et al., *Creating Hierarchical Pores in Zeolite Catalysts*. Trends in Chemistry, 2019. **1**(6): p. 601-611.
 23. Verboekend, D. and J. Pérez-Ramírez, *Design of hierarchical zeolite catalysts by desilication*. Catalysis Science & Technology, 2011. **1**(6): p. 879-890.

24. Xuan Meng, Z.L., Xin Wang, Li Shi, Naiwang Liu, *Effect of dealumination of HZSM-5 by acid treatment on catalytic properties in non-hydrocracking of diesel*. Fuel, 2020. **270**.
25. Wang, G., et al., *Hydroisomerization activity and selectivity of n-dodecane over modified Pt/ZSM-22 catalysts*. Applied Catalysis A: General, 2008. **335**(1): p. 20-27.
26. Sammoury, H., et al., *Impact of desilication of *BEA zeolites on the catalytic performance in hydroisomerization of n -C 10*. Applied Catalysis A: General, 2018. **551**: p. 1-12.
27. Zhang, Z., et al., *Competitive conversion pathways of methyl palmitate to produce jet biofuel over Ni/desilicated meso-Y zeolite catalyst*. Fuel, 2019. **244**: p. 472-478.
28. Organization, I.C.A. *Sustainable aviation guide*. 2018 December 2018.
29. Khan, S., et al., *A review on deoxygenation of triglycerides for jet fuel range hydrocarbons*. Journal of Analytical and Applied Pyrolysis, 2019. **140**: p. 1-24.
30. Eller, Z., Z. Varga, and J. Hancsók, *Advanced production process of jet fuel components from technical grade coconut oil with special hydrocracking*. Fuel, 2016. **182**: p. 713-720.
31. S. A. Treese, P.R.P., David S. J. Jones, *Handbook of Petroleum Processing*. 2 ed. 2015: SpringerReference.
32. Mäki-Arvela, P., et al., *Catalytic Hydroisomerization of Long-Chain Hydrocarbons for the Production of Fuels*. Catalysts, 2018. **8**(11).
33. Song, C., et al., *Cooperativity of adjacent Brønsted acid sites in MFI zeolite channel leads to enhanced polarization and cracking of alkanes*. Journal of Catalysis, 2017. **349**: p. 163-174.
34. *Post-Synthesis Modification I*, in *Molecular Sieves Science and Technology*, W. H. G. Karge, Editor. 2002, Springer-Verlag Berlin Heidelberg. p. 204-255.
35. Sazama, P., et al., *Superior activity of non-interacting close acidic protons in Al-rich Pt/H-*BEA zeolite in isomerization of n-hexane*. Applied Catalysis A: General, 2017. **533**: p. 28-37.
36. Wang, C., et al., *Acid and alkali treatments for regulation of*

- hydrophilicity/hydrophobicity of natural zeolite*. Applied Surface Science, 2019. **478**: p. 319-326.
37. Suárez, N., et al., *Preparation of mesoporous Beta zeolite by fluoride treatment in liquid phase. Textural, acid and catalytic properties*. Microporous and Mesoporous Materials, 2019. **284**: p. 296-303.
38. Yu, Q., et al., *Highly mesoporous IM-5 zeolite prepared by alkaline treatment and its catalytic cracking performance*. Microporous and Mesoporous Materials, 2019. **273**: p. 297-306.
39. Tamizhdurai, P., et al., *Effect of acidity and porosity changes of dealuminated mordenite on n-pentane, n-hexane and light naphtha isomerization*. Microporous and Mesoporous Materials, 2019. **287**: p. 192-202.
40. Zhang, M., et al., *Creating mesopores in ZSM-48 zeolite by alkali treatment: Enhanced catalyst for hydroisomerization of hexadecane*. Journal of Energy Chemistry, 2016. **25**(3): p. 539-544.
41. Wang, B., et al., *Citric acid-modified beta zeolite for polyoxymethylene dimethyl ethers synthesis: The textural and acidic properties regulation*. Applied Catalysis B: Environmental, 2020. **266**.
42. Uvarov, V. and I. Popov, *An estimation of the correctness of XRD results obtained from the analysis of materials with bimodal crystallite size distribution*. CrystEngComm, 2015. **17**(43): p. 8300-8306.
43. Sun, H., et al., *Effect of acidity and porosity of hierarchical HBEA zeolite on catalytic stability of α -methyl naphthalene isomerization*. Journal of Porous Materials, 2018. **26**(4): p. 961-970.
44. Dzwigaj, S., et al., *Incorporation of Nb(V) into BEA zeolite investigated by XRD, NMR, IR, DR UV-vis, and XPS*. Microporous and Mesoporous Materials, 2010. **130**(1-3): p. 162-166.
45. Emeis, C.A., *Determination of Integrated Molar Extinction Coefficients for Infrared-Absorption Bands of Pyridine Adsorbed on Solid Acid Catalysts*. Journal of Catalysis, 1993. **141**(2): p. 347-354.
46. Abnisa, F., et al., *Utilization possibilities of palm shell as a source of biomass*

- energy in Malaysia by producing bio-oil in pyrolysis process. *Biomass and Bioenergy*, 2011. **35**(5): p. 1863-1872.
47. Lin, C.-H., Y.-K. Chen, and W.-C. Wang, *The production of bio-jet fuel from palm oil derived alkanes*. *Fuel*, 2020. **260**: p. 116345.
48. Baran, R., et al., *Hydrodechlorination of 1,2-dichloroethane on nickel loaded Beta zeolite modified by copper: Influence of nickel and copper state on product selectivity*. *Catalysis Today*, 2014. **226**: p. 134-140.
49. Otomo, R., et al., *Dealuminated Beta zeolite as effective bifunctional catalyst for direct transformation of glucose to 5-hydroxymethylfurfural*. *Applied Catalysis A: General*, 2014. **470**: p. 318-326.
50. María Dolores González, Y.C., Pilar Salagre, *Comparison of dealumination of zeolites beta, mordenite and ZSM-5 by treatment with acid under microwave irradiation*. *Microporous and Mesoporous Materials*, 2011. **144** p. 162–170.
51. Baran, R., et al., *Influence of the nitric acid treatment on Al removal, framework composition and acidity of BEA zeolite investigated by XRD, FTIR and NMR*. *Microporous and Mesoporous Materials*, 2012. **163**: p. 122-130.
52. Maier, S.M., A. Jentys, and J.A. Lercher, *Steaming of Zeolite BEA and Its Effect on Acidity: A Comparative NMR and IR Spectroscopic Study*. *The Journal of Physical Chemistry C*, 2011. **115**(16): p. 8005-8013.
53. Omegna, A., et al., *Dealumination and realumination of microcrystalline zeolite beta: an XRD, FTIR and quantitative multinuclear (MQ) MAS NMR study*. *Physical Chemistry Chemical Physics*, 2004. **6**(2).
54. Qin, Z., et al., *Chemical Equilibrium Controlled Etching of MFI-Type Zeolite and Its Influence on Zeolite Structure, Acidity, and Catalytic Activity*. *Chemistry of Materials*, 2013. **25**(14): p. 2759-2766.
55. Kydd, A.K.G.a.R.A., *An infrared study of the effect of HF treatment on the acidity of ZSM-5*. *Zeolites* 1990. **10**: p. 766–771.
56. Thommes, M., et al., *Physisorption of gases, with special reference to the evaluation of surface area and pore size distribution (IUPAC Technical Report)*. *Pure and Applied Chemistry*, 2015. **87**(9-10): p. 1051-1069.
57. Wang, J.X., et al., *Enhancement of light aromatics from catalytic fast pyrolysis*

- of cellulose over bifunctional hierarchical HZSM-5 modified by hydrogen fluoride and nickel/hydrogen fluoride. Bioresour Technol, 2019. 278: p. 116-123.*
58. Bolshakov, A., et al., *Mild dealumination of template-stabilized zeolites by NH₄F. Catalysis Science & Technology, 2019. 9(16): p. 4239-4247.*
59. Grams, J., et al., *Hydrogen-Rich Gas Production by Upgrading of Biomass Pyrolysis Vapors over NiBEA Catalyst: Impact of Dealumination and Preparation Method. Energy & Fuels, 2020. 34(12): p. 16936-16947.*
60. Ryczkowski, R., et al., *Effect of alkali and alkaline earth metals addition on Ni/ZrO₂ catalyst activity in cellulose conversion. Journal of Thermal Analysis and Calorimetry, 2016. 126(1): p. 103-110.*
61. C. Louis, Z.X.C., M. Che, *Characterization of nickel on silica catalysts during impregnation and further thermal activation treatment leading to metal particles.pdf. The Journal of Physical Chemistry A, 1993. 97: p. 5703-5712.*
62. Peron, D.V., et al., *Nickel-zeolite composite catalysts with metal nanoparticles selectively encapsulated in the zeolite micropores. Journal of Materials Science, 2019. 54(7): p. 5399-5411.*
63. Sousa, F.P., et al., *Simultaneous deoxygenation, cracking and isomerization of palm kernel oil and palm olein over beta zeolite to produce biogasoline, green diesel and biojet-fuel. Fuel, 2018. 223: p. 149-156.*
64. Kim, T.W., et al., *Effects of Zeolite Supports on the Production of Fuel-Range Hydrocarbons in the Hydrotreatment of Various Vegetable Oils with Platinum-Based Catalysts. J Nanosci Nanotechnol, 2019. 19(4): p. 2443-2448.*
65. Han, G.B., et al., *Operation of bio-aviation fuel manufacturing facility via hydroprocessed esters and fatty acids process and optimization of fuel property for turbine engine test. Korean Journal of Chemical Engineering, 2021. 38(6): p. 1205-1223.*
66. Lyu, Y., et al., *One-pot synthesis of the highly efficient bifunctional Ni-SAPO-11 catalyst. Journal of Materials Science & Technology, 2021. 76: p. 86-94.*
67. Xing, S., et al., *One-step hydroprocessing of fatty acids into renewable aromatic hydrocarbons over Ni/HZSM-5: insights into the major reaction pathways. Phys Chem Chem Phys, 2017. 19(4): p. 2961-2973.*

68. S. A. Treese, P.R.P., D. S. J. Jones, *Hydrocracking in Petroleum Processing*. 2 ed. Handbook of Petroleum Processing. 2015: SpringerReference.
69. Fedyna, M., et al., *Effect of zeolite amount on the properties of Pt/(ALSBA-15 + Beta zeolite) micro-mesoporous catalysts for the hydroisomerization of n-heptane*. Fuel, 2020. **280**.
70. Liu, Y., et al., *Hydrotreatment of Vegetable Oils to Produce Bio-Hydrogenated Diesel and Liquefied Petroleum Gas Fuel over Catalysts Containing Sulfided Ni-Mo and Solid Acids*. Energy & Fuels, 2011. **25**(10): p. 4675-4685.
71. Sholeha, N.A., et al., *Enhanced CO₂ methanation at mild temperature on Ni/zeolite from kaolin: effect of metal-support interface*. RSC Advances, 2021. **11**(27): p. 16376-16387.
72. Martens, J.A., et al., *Hydroisomerization and hydrocracking of linear and multibranched long model alkanes on hierarchical Pt/ZSM-22 zeolite*. Catalysis Today, 2013. **218-219**: p. 135-142.
73. El-Sawy, M.S., et al., *Co-hydroprocessing and hydrocracking of alternative feed mixture (vacuum gas oil/waste lubricating oil/waste cooking oil) with the aim of producing high quality fuels*. Fuel, 2020. **269**.
74. Zhang, Z., et al., *Hydroconversion of Waste Cooking Oil into Green Biofuel over Hierarchical USY-Supported NiMo Catalyst: A Comparative Study of Desilication and Dealumination*. Catalysts, 2017. **7**(10).
75. Hossain, M.A., et al., *Catalytic isomerization of dihydroxyacetone to lactic acid by heat treated zeolites*. Applied Catalysis A: General, 2021. **611**.
76. Silva, L.S.d., et al., *Desilication of ZSM-5 and ZSM-12 Zeolites with Different Crystal Sizes: Effect on Acidity and Mesoporous Initiation*. Materials Research, 2019. **22**(2).
77. Yan, L., et al., *Evolution of the pore and framework structure of NaY zeolite during alkali treatment and its effect on methanol oxidative carbonylation over a CuY catalyst*. Journal of Chemical Research, 2020. **44**(11-12): p. 710-720.
78. Sammoury, H., et al., *Desilication of *BEA zeolites using different alkaline media: Impact on catalytic cracking of n-hexane*. Microporous and Mesoporous Materials, 2018. **267**: p. 150-163.

79. Tama's I. Korá'nyi, a.J.n.B.N., *Distribution of Aluminum in Different Periodical Building Units of MOR and BEA Zeolites*. J. Phys. Chem. B, 2005. **109**: p. 15791-15797.
80. Rankin, A.G.M., et al., *Determining the Surface Structure of Silicated Alumina Catalysts via Isotopic Enrichment and Dynamic Nuclear Polarization Surface-Enhanced NMR Spectroscopy*. J Phys Chem C Nanomater Interfaces, 2017. **121**(41): p. 22977-22984.
81. dos Santos, L.R.M., et al., *Creation of mesopores and structural re-organization in Beta zeolite during alkaline treatment*. Microporous and Mesoporous Materials, 2016. **226**: p. 260-266.
82. Trejda, M., et al., *Methanol oxidation on VSiBEA zeolites: Influence of V content on the catalytic properties*. Journal of Catalysis, 2011. **281**(1): p. 169-176.
83. Kasyanov, I.A., et al., *Towards understanding of the mechanism of stepwise zeolite recrystallization into micro/mesoporous materials*. J. Mater. Chem. A, 2014. **2**(40): p. 16978-16988.
84. Busca, G., *Acidity and basicity of zeolites: A fundamental approach*. Microporous and Mesoporous Materials, 2017. **254**: p. 3-16.
85. Gamliel, D.P., et al., *Nickel impregnated mesoporous USY zeolites for hydrodeoxygenation of anisole*. Microporous and Mesoporous Materials, 2018. **261**: p. 18-28.
86. Mihályi, R.M., et al., *n-Heptane hydroconversion over nickel-loaded aluminum- and/or boron-containing BEA zeolites prepared by recrystallization of magadiite varieties*. Journal of Molecular Catalysis A: Chemical, 2013. **367**: p. 77-88.
87. Hu, D., et al., *S-Doped Ni(OH)₂ nano-electrocatalyst confined in semiconductor zeolite with enhanced oxygen evolution activity*. Journal of Materials Chemistry A, 2020. **8**(22): p. 11255-11260.
88. Schreiber, M.W., et al., *Hydrodeoxygenation of fatty acid esters catalyzed by Ni on nano-sized MFI type zeolites*. Catalysis Science & Technology, 2016. **6**(22): p. 7976-7984.
89. Ananmaria P. P. Pires, Y.H., John Kramlich, and Manuel Garcia-Perez, *Chemical composition and fuel properties of alternative jet fuels*. Bioresources, 2018.

13(2): p. 2632-2657.





จุฬาลงกรณ์มหาวิทยาลัย
CHULALONGKORN UNIVERSITY

VITA

NAME Warodom Hunsiri

DATE OF BIRTH 9 september 1995

PLACE OF BIRTH Samutprakan

INSTITUTIONS ATTENDED B.Sc. in Chemistry, Faculty of Science,
Mahidol University, Bangkok, Thailand

HOME ADDRESS 1614/841 khehasamutprakan, Sukhumvit road, Taibanmai,
muang, Samutprakan

PUBLICATION Warodom Hunsiri, Napida Hinchiranan "Effect of
dealumination of beta zeolite on performance of nickel
catalysts in hydroisomerization of palm oil for bio-jet fuel
production" Proceeding of PPC & PETROMAT SYMPOSIUM
2020, Bangkok, Thailand, JULY 23, 2020, pp 25-30.